Photon Pair Sources in Periodically Poled Ti:LiNbO$_3$ Waveguides

A THESIS

submitted by

Abu Thomas

for the award of the degree

of

Doktor der Naturwissenschaften (Dr. rer. nat.)

Department of Physics
University of Paderborn, Germany

December 2010

TABLE OF CONTENTS

Chapter 1

Introduction

In 1900, Max Planck postulated that the energy of electro-magnetic fields is quantized [1]. The motivation was to overcome the ultra-violet catastrophe in the existing models for black body spectrum. Albert Einstein used this idea to explain the photo-electric effect in 1905 [2]. He also mentioned the possibility of population inversion in a medium to achieve gain. It took another 50 years before the first laser was invented in 1960, by Theodore H. Maiman at Hughes Research Laboratories [3]. The discovery of the laser led to a flurry of research activities in the emerging field of non-linear optics. The high power of a laser helps to achieve more pronounced non-linear effects in bulk crystals. S. E. Miller, working in Bell Labs, proposed the idea of integrated optics [4]. The motivation was to achieve highly functional integrated circuits at optical wavelengths, like the electronic integrated circuits. Soon it was realized that the non-linear effects could be further enhanced by using integrated optical circuits. The key element of an integrated optical circuit is a waveguide, which confines light along transverse directions while energy is transported in a perpendicular direction. Non-linear effects like *spontaneous parametric down conversion* with enhanced efficiency was demonstrated in waveguides by means of quasi phase matching .

A similar revolution was underway in the conceptual understanding of quantum mechanics. The famous Bell test experiments, which proved the non-local nature of quantum mechanics, used photon pairs from a radiative cascade of Calcium atoms [5; 6; 7]. Similar experiments were repeated using photon pairs generated from bulk crystals by the non-linear process of spontaneous parametric down conversion. Today, the use of photon pair sources extends beyond the realm of improving the knowledge of quantum mechanics, into quantum key distribution [8], quantum teleportation [9], entanglement swapping [10] etc. In this context, photon pair sources realized using down conversion, especially in waveguides fabricated in crystals, have an increasingly important role.

An essential aspect of the applications mentioned above is the post-processing of the quantum state of the generated photon. The post-processing, for example, includes modifying the phase of the single photon state or spatially re-directing them by means of a beam splitter. Some times, it may be required to change the polarization state of the generated photon. These requirements are traditionally realized using linear optical components behind the photon source. The use of separate bulk optical components leads to problems concerning optical alignment, mode shaping etc. The use of integrated optical circuits, with the source and components integrated into the same substrate, potentially eliminate these problems associated with post-processing, without compromising on efficient generation of the photons. An additional advantage is the possibility to glue an optical fiber with the waveguide, potentially increasing the variety of post-processing using standard fiber optic components, besides the easier handling of the source.

The waveguides fabricated by Ti in-diffusion in $LiNbO_3$ crystal is the non-linear medium of choice in our experiments. $LiNbO_3$ has excellent electro-optic, acousto-optic and optical properties [11]. The optical second order non-linearity of $LiNbO_3$ is the driving force behind spontaneous parametric down conversion. The fabrication of a waveguide in $LiNbO_3$ helps to confine the excitation (a coherent laser source) into very small area ($\approx 100\ \mu m^2$) over a few cms, leading to enhanced non-linear efficiency. The propagation loss in such waveguides can be kept as small as $0.01\ \frac{dB}{cm}$. Moreover, the waveguides fabricated by Ti in-diffusion can guide orthogonally polarized fields. This is a clear advantage over competing technologies like waveguides fabricated by proton exchange in $LiNbO_3$, which only guides one polarization [12; 13]. The small propagation losses, strong non-linearity and guidance of orthogonally polarized fields allows type II spontaneous parametric down conversion, which is the focus of this thesis.

Type II down conversion in $Ti:LiNbO_3$ has been demonstrated by Tanzilli [14] and Suhara [15]. In both schemes, quantum nature of photon pairs was demonstrated by a coincidence experiment. However, the post processing of photon pairs is implemented using bulk optical components. In accordance with the philosophy of integrated optics, we explore the possibility to integrate the linear optical components directly behind the source, on the same substrate. Towards the goal of achieving a fiber pigtailed integrated source, we investigate in detail the coupling efficiency from an optical fiber to a waveguide. The goal is to demonstrate an integrated structure with the source and linear optical components, along with pigtailed optical fibers at both ends.

Another goal of the thesis is the demonstration of an entangled photon pair source. Entangled photon pair sources based on down conversion in $Ti:LiNbO_3$ have been demonstrated by Tanzilli [16] and Suhara [17]. The former is based on type II down conversion at $\lambda = 1310$ nm. The source operates at degeneracy point, i.e., both photons of a pair are at the same wavelength. However, only half of the generated pairs contribute to entanglement. The scheme of Suhara overcomes this draw-back by realizing entanglement with the two photons of a pair at different wavelengths. Even though all pairs contribute to entanglement, the photons pairs generated are distinguishable. We investigate a scheme to overcome the draw back, by designing an entangled photon pair source at non-degeneracy, using a special interlaced domain structure.

Organization of the Thesis

Chapter 2 reviews the basic theoretical framework required to understand the process of spontaneous parametric down conversion. A model for Ti in-diffused waveguides in $LiNbO_3$ is presented. Once the normal modes of the waveguide are identified, a model for non-linearity is introduced by considering the non-linear polarization. The coupled mode equations, which govern the evolution of the interacting fields, are derived based on slowly varying envelope approximation. Simulation results concerning second harmonic generation based on quasi phase matching is presented. The final section explores the theory of spontaneous para-

metric down conversion in the context of Ti:LiNbO$_3$ waveguides in detail and compares the efficiency of the process in other interaction media.

Chapter 3 focuses on basic characterization of waveguides. The basic steps in the fabrication of Ti:LiNbO$_3$ waveguides are explained. The technique to achieve periodic domain inversion of the sample after the waveguide fabrication is explained. The characterization of the propagation loss of orthogonally polarized fields in the waveguide is discussed. Mode size measurement results of single mode waveguides at 1550 nm is presented and compared with that of standard single mode optical fiber. The polarization dependent coupling efficiency of power from a waveguide to optical fiber is estimated based on the overlap integral between the respective modes.

Chapter 4 explains in detail a packaged integrated photon pair source. The results concerning a detailed characterization of the second harmonic generation and spontaneous parametric down conversion experiments are presented. Theoretical and experimental aspects of a polarization beam splitter integrated on the same substrate is explained. Design issues as well as measurement results of a dielectric mirror deposited on the end-face of the sample is discussed. A detailed explanation about the steps involved in pigtailing and packaging of the sample is presented. Finally, the characterization of the photon pair source by coincidence measurement results is also discussed.

Chapter 5 discusses in detail an entangled photon pair source realized with interlaced domain structure. The design issues of the interlaced domain structure is presented. Simulation and experimental results concerning second harmonic generation and spontaneous parametric down conversion are explained. The chapter concludes by showing in detail the characterization of entanglement by an interference experiment.

Chapter 6 summarizes the main results of the thesis. A list of possible future activities related to the work presented in the thesis is discussed.

Additional information is provided in the appendix A, B and C. Appendix A explains the Sellmeier's equations for bulk LiNbO$_3$, Appendix B presents some derivations related to quantum model of spontaneous parametric down conversion. Finally, Appendix C explains the essential aspects of quantum model of coincident counts using two single photon detectors.

Spontaneous Parametric Down Conversion in Periodically Poled Ti:LiNbO$_3$ waveguides: Theoretical Analysis

The most widely used approach to generate single photons is by means of spontaneous parametric down conversion. In this scheme, a photon traveling through a non-linear optical crystal spontaneously decays into two longer wavelength photons. The first section introduces the basic theoretical framework needed to understand the spontaneous parametric down converion (SPDC). In the second section, the concept of quasi phase matching is introduced. This is a pre-requisite for non-linear optical interaction over regions longer than a few optical wavelengths. By tailoring the QPM, a variety of non-linear processes can be accomplished which broadly falls into two categories; Type I and Type II. These processes are explained in third section. In the final section, some calculations concerning SPDC is presented.

2.1 Waveguide Model

The basic scheme of SPDC is shown in Fig 2.1.
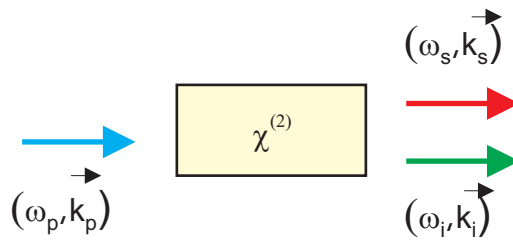
Figure 2.1: Scheme of SPDC. A pump photon (ω_p) in a waveguide fabricated in a non-linear crystal spontaneously decays into longer wavelength signal (ω_s) and idler (ω_i) photons. $\vec{\mathrm{k}}_\mathrm{s,i,p}$ are vectors associated with the momentum of the photons.

The pump photon with frequency ω_p and momentum $\hbar\vec{\mathrm{k}}_\mathrm{p}$, traveling through a waveguide fabricated in a non-linear crystal, spontaneously down-converts into photons with frequencies $\omega_\mathrm{s,i}$ and momentum vectors $\hbar\vec{\mathrm{k}}_\mathrm{s,i}$ [18]. The down-converted photons are called signal and idler photons (indicated by the subscripts 's' and 'i'. Both, the signal and idler photons, have longer wavelengths compared to the

pump photon. They satisfy the energy and the momentum conservation condtions (Eq. 2.1).

$$\hbar\omega_{\mathrm{p}} \ = \ \hbar\omega_{\mathrm{s}} \ + \ \hbar\omega_{\mathrm{i}}$$
$$\hbar\vec{\mathrm{k}}_{\mathrm{p}} \ = \ \hbar\vec{\mathrm{k}}_{\mathrm{s}} \ + \ \hbar\vec{\mathrm{k}}_{\mathrm{i}}$$
$$(2.1)$$

In this thesis, we are interested in the down conversion process in channel waveguides fabricated by in-diffusion of Ti in LiNbO$_3$, as the interaction medium. Such waveguides have been extensively investigated in integrated optics after they were fabricated for the first time by Kaminow [19]. Waveguides of very low losses have been realized without compromising the non-linear properties of the substrate. Ti in-diffusion has the advantage that orthogonally polarized fields can be transmitted.

The schematic of the waveguide is shown in Fig. 2.2.
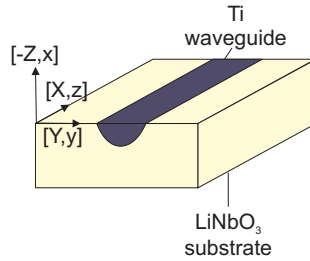
Figure 2.2: Schematic of a Ti in-diffused waveguide on a LiNbO$_3$ substrate. The crystallographic axes are indicated by capital letters. Co-ordinate axes are indicated by small letters.

We consider waveguides fabricated on a Z-cut LiNbO$_3$ substrate. The propagation is in the crystallographic X direction. So the fields polarized along the x-axis see the extra-ordinary index (n_{e}) and fields polarized along the y-axis see the ordinary index (n_{o}). LiNbO$_3$ is a birefringent crystal with $n_{\mathrm{o}} > n_{\mathrm{e}}$. The dispersion of the refractive indices are modeled using Sellmeier equations as shown in [20]. Details concerning waveguide fabrication are summarized in Chapter 3.

The in-diffusion process of Ti in LiNbO$_3$ is modeled by using Fick's law [21]. The concentration profile, c(x,y), of Ti after in-diffusion is

$$c(x,y) \ = \ c(0,0) \ f(x) \ g(y), \qquad \text{where}$$

$$g(y) \ = \ \frac{1}{2} \left[\mathrm{erf}\left(\frac{y + \frac{W}{2}}{W_{y}} \right) + \mathrm{erf}\left(\frac{y - \frac{W}{2}}{W_{y}} \right) \right] \qquad \text{and}$$

$$f(x) \ = \ \mathrm{e}^{-\left(\frac{x^2}{W_{x}^2} \right)}.$$

The functions, f(x) and g(y), represent the distributions along the depth and the width of the waveguide respectively. W is the width of the Ti stripe before in-diffusion. c(0,0) is the Ti concentration in the stripe. W_{x} and W_{y} are diffusion lengths along the x and y directions. The dependence of the diffusion lengths on

temperature T and diffusion time τ are shown below.

$$W_{x,y} = \sqrt{D_{x,y}(T)\,\tau} \qquad D_x(\infty) = 2710\,\frac{\mu m^2}{s} \qquad D_y(\infty) = 2890\,\frac{\mu m^2}{s}$$

$$D_{x,y} = D_{x,y}(\infty)\,e^{-\left(\frac{Q_{x,y}}{k_B T}\right)} \qquad Q_x = 1.936\,\text{eV} \qquad Q_y = 1.905\,\text{eV}$$

In the above equations, $D_{x,y}$ is the diffusion constant, $Q_{x,y}$ is the activation energy and k_B is the Boltzmann constant. The change of the refractive index $\delta n_{o,e}$ due to the diffusion is modelled as a function of wavelength and concentration as follows:

$$\delta n_e = \frac{0.839\,\lambda^2}{\lambda^2 - 0.0645}\,V_e\,c(x,y) \qquad V_e = 1.2 \times 10^{-23}\,\text{cm}^3$$

$$\delta n_o = \frac{0.8\,\lambda^2}{\lambda^2 - 0.08066}\,[V_o\,c(x,y)]^{0.5} \qquad V_o = 1.3 \times 10^{-25}\,\text{cm}^3$$

The change in refractive index along the ordinary axis is smaller compared to the change along the extra-ordinary axis.

Once the refractive index profiles are known, the normal modes of the waveguides are calculated. For this we consider the most general form of Maxwell's equations in an inhomogeneous and anisotropic medium. The evolution of electric field is described by the well-known second order Helmholtz equation [22]. In time domain the equation has the form,

$$\nabla\left[\nabla \cdot \vec{E}\right] - \nabla^2 \vec{E} + \mu_0 n^2 \partial_t^2 \vec{E} = -\partial_t^2 \vec{P}^{(2)} \tag{2.5}$$

The non-linear effects enter the model through the driving term on the right hand side $-\partial_t^2 \vec{P}^{(2)}$. This is a small effect on the wave equation in the linear approximation. To proceed further, we neglect the contribution of the non-linear polarization. The effect of the non-linear polarization is re-introduced later after finding the normal modes of the waveguide. We simplify the first term in Eq. 2.5 by finding the divergence of $\vec{E} = E_x\,\hat{x} + E_y\,\hat{y}$ using Gauss' law as follows:

$$\nabla \cdot n^2 \vec{E} = 0$$

$$\Rightarrow \nabla \cdot \vec{E} = -\frac{1}{n^2}\nabla n^2 . \vec{E}$$

$$\Rightarrow \nabla \cdot \vec{E} = -\frac{1}{n^2}\partial_x n^2\,E_x - \frac{1}{n^2}\partial_y n^2\,E_y - \underbrace{\left[\frac{1}{n^2}\partial_z n^2\,E_z\right]}_{=0}$$

In the case of a waveguide, where the confinement is only along the transverse directions (x,y), there is no variation of the refractive index along the propagation direction (z). Hence, in the last step the term proportional to $\partial_z n^2$ is neglected. Using this expression for the divergence of the electric field in the Helmholtz

equation we arrive at two coupled equations,

$$\partial_x \left[\frac{1}{n^2} \partial_x n^2 \, E_x \right] + \partial_y^2 \, E_y + \partial_z^2 \, E_z - \mu_0 n^2 \partial_t^2 \, E_x = -\partial_t^2 \vec{P}^{(2)} - \underbrace{\partial_x \left[\frac{1}{n^2} \partial_y n^2 \, E_y \right]}_{\approx 0}$$

$$\partial_x^2 \, E_x + \partial_y \left[\frac{1}{n^2} \partial_y n^2 \, E_y \right] + \partial_z^2 \, E_z - \mu_0 n^2 \partial_t^2 \, E_x = -\partial_t^2 \vec{P}^{(2)} - \underbrace{\partial_y \left[\frac{1}{n^2} \partial_x n^2 \, E_x \right]}_{\approx 0}$$

The coupling terms are shown on the right hand side. They are small and are neglected. Also neglecting the driving term representing the non-linear polarization, we arrive at two independent equations whose solutions are known as transverse electric (TE) and transverse magnetic (TM) modes. With the waveguide geometry shown in Fig. 2.2, the TE polarized field sees the ordinary index ($n_o(\omega)$) and the TM polarized field sees the extra-ordinary index ($n_e(\omega)$). The numerical techniques based on the effective index method or the finite element method to solve the transverse distribution of TE and TM modes have been extensively studied [23; 22]. Both techniques take into consideration the anisotropy of the waveguide and the refractive index distribution. Solvers based on such techniques give the mode field distribution and the effective index as a function of wavelength. The effective index determines the propagation constant of a mode along the waveguide. The propagation constant β is a function of frequency and is polarization dependent. The propagation constant is related to an effective index n_{eff} defineda as follows:

$$\beta_{\text{TE,TM}} \left(\omega \right) \equiv \frac{\omega}{c} \, n_{\text{eff,TE,TM}} \left(\omega \right). \tag{2.8}$$

Note that effective index is different for TE and TM modes. The mode field distributions at different wavelengths determine an overlap integral which is a crucial factor determining the efficiency of non-linear processes in the waveguide. Also, the dispersion of the effective indices determine the wavelengths of the pump, signal and idler which interact via the non-linear process. To understand quantitatively the non-linear effects, we re-introduce the non-linear polarization, $P^{(2)}$ into the Maxwell's equations. The results are explained in the next section.

2.2   Non-linear Polarization

The coupling of energy from the pump photon to the signal and idler photons is facilitated by the polarization induced in the crystal. The pump and the idler fields, in addition to the polarization at ω_p and ω_i, also induce a weak polarization at ω_s, which contributes to the signal field. Similarly the pump and the signal fields induce a polarization at ω_i which contributes to the idler field. The weak polarization responsible for the coupling is due to the well known second order non-linearity [24]. In general, the complex amplitude of the electric displacement
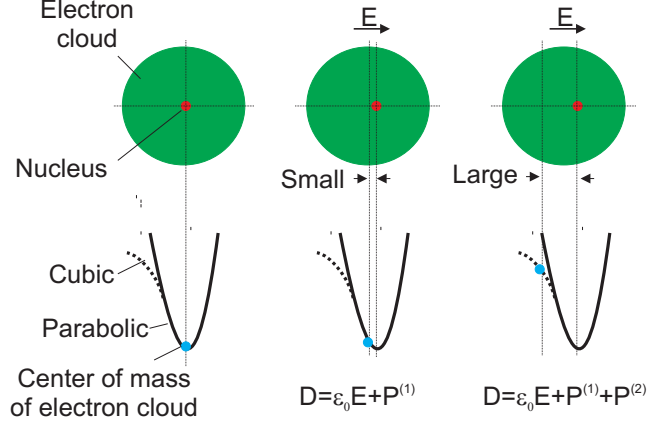
Figure 2.3: Physical origin of linear and non-linear polarization. When there is no external field, the center of mass of the electron cloud and the nucleus coincide. In the presence of an external field, the center of mass of the electron cloud is displaced from the nucleus with a linear restoring force (parabolic potential well). When the field is strong enough, the restoring force is weakly non-linear (cubic potential well).

$(\vec{D})$ at a point $(\vec{r})$ in the interaction medium has the form

$$\vec{D}(\omega, \vec{r}) = \epsilon_0 \vec{E}(\omega, \vec{r}) + \vec{P}(\omega, \vec{r}) \qquad \text{where} \qquad (2.9a)$$

$$\vec{P}(\omega, \vec{r}) = \vec{P}^{(1)}(\omega, \vec{r}) + \vec{P}^{(2)}(\omega, \vec{r}) \qquad (2.9b)$$

where $\vec{E}$ and $\vec{P}$ are the complex amplitudes of electric field and the polarization respectively. The polarization is the sum of a strong polarization $P^{(1)}$ and a weak polarization $P^{(2)}$. The physical origin of linear and non-linear electric susceptibilities is shown schematically in Fig. 2.3. The strong polarization results from the linear electric susceptibility ($\chi^{(1)}$). At the atomic level, $\chi^{(1)}$ is related to the displacement of the center of mass of the electron cloud from the equilibrium position. The dipole moment resulting from this displacement and hence $P^{(1)}$ is proportional to the electric field. The displacement is assumed to be small enough that the restoring force on the electron cloud is still linear, and hence the name linear electric susceptibility.

$$P^{(1)}(\omega, z) = \epsilon_0 \chi^{(1)}(\omega) E(\omega, z) \qquad (2.10)$$

The weak polarization $P^{(2)}$ results from the second order electric susceptibility ($\chi^{(2)}$). When the input fields are strong enough, the electron cloud is pulled into a region where the restoring force is non-linear. The resulting dipole moment contains contributions from (in addition to the input frequencies) electron oscillations at other frequencies. If the input frequencies are ω_s and ω_i, then

$$P_i^{(2)}(\omega_p, z) = \epsilon_0 \chi_{ijk}^{(2)}(\omega_p, \omega_s, \omega_i) E_i(\omega_s, z) E_k(\omega_i, z) \qquad (2.11)$$

The indices i, j and k indicate the orientation of the fields. The non-linear tensor $\chi_{ijk}^{(2)}$ couples the fields oriented in the j and k direction through the induced non-linear polarization $P_i^{(2)}[\omega_p, z]$. In principle, $3^3 = 81$ different elements in

8

the matrix representation of $\chi^{(2)}_{ijk}$ allow an equal number of different non-linear interactions. However, the symmetry considerations of the non-linear medium restrict the range and variety of possible non-linear interactions. Also, when the frequencies involved are far off from the resonant frequencies of the medium, an additional constraint, called Kleinman symmetry, further restricts the possible interactions [25]. In the case of LiNbO$_3$, only 8 elements are non-zero [11]. The non-linear coefficients d$_{33}$ = 30 $\frac{\text{pm}}{V}$ and d$_{31}$ = 5 $\frac{\text{pm}}{V}$ are are most commonly used. The non-linear coefficient d$_{33}$ couples fields polarized along the extra-ordinary axis. Using d$_{33}$ in LiNbO$_3$ waveguide, a variety of non-linear processes like second harmonic generation, difference frequency generation, optical parametric amplification and optical parametric oscillation has been reported [26; 27]. However, the focus of this thesis is on spontaneous parametric down conversion mediated by d$_{31}$. The coefficient d$_{31}$ couples orthogonally polarized input fields. Before considering the down conversion process in detail, we focus first on the non-linear process of second harmonic generation. The second harmonic generation is conceptually much simpler to understand and the mathematical techniques used to model down conversion and second harmonic generation are almost the same.

In waveguides made on Z-cut, X-propagating LiNbO$_3$ the non-linear polarizations involved in three wave mixing are written as

$$P^{(2)}_{\text{SH}}\left(\omega_{\text{SH}}, z\right) = 2\epsilon_0 \, d_{31} \, E_{\text{TE}}\left(\omega_{\text{TE}}, z\right) E_{\text{TM}}\left(\omega_{\text{TM}}, z\right)$$
$$P^{(2)}_{\text{TE}}\left(\omega_{\text{TE}}, z\right) = 2\epsilon_0 \, d_{31} \, E_{\text{SH}}\left(\omega_{\text{SH}}, z\right) E^*_{\text{TM}}\left(\omega_{\text{TM}}, z\right)$$
$$P^{(2)}_{\text{TM}}\left(\omega_{\text{TM}}, z\right) = 2\epsilon_0 \, d_{33} \, E_{\text{SH}}\left(\omega_{\text{SH}}, z\right) E^*_{\text{TE}}\left(\omega_{\text{TE}}, z\right)$$

Note that $\omega_{\text{SH}} = \omega_{\text{TE}} + \omega_{\text{TM}}$ in the above equations. This is necessary to satisfy energy conservation requirement. The subscript SH indicates second harmonic and in this case $\omega_{\text{TE}} = \omega_{\text{TM}} = \omega_{\text{f}}$. The input field with the frequency ω_{f} is called the fundamental.

To study the evolution of fields in the interaction region, we look at the second harmonic generation process in more detail. In order to ensure the build up of SH in the interaction region (by transfer of energy from the fundamental to the SH), a proper phase relationship has to be maintained between $P^{(2)}_{\text{SH}}\left(\omega_{\text{SH}}, z\right)$ and $E_{\text{SH}}\left[\omega_{\text{SH}}, z\right]$. The non-linear polarization, varies along the interaction region with a spatial dependence of $e^{i[\beta_{\text{TE}}+\beta_{\text{TM}}]z}$, where $\beta_{\text{TE,TM}} = \frac{\omega_{\text{f}} n_{\text{TE,TM}}}{c}$ are the propagation constants of the fundamental field. The SH, on the other hand, varies along the interaction region with a spatial dependence of $e^{i\beta_{\text{SH}}z}$, where $\beta_{\text{SH}} = \frac{2\omega_{\text{f}} n_{\text{SH}}}{c}$ is the propagation constant of the SH field. The refractive indices, n$_{\text{TE,TM}}$ of the fundamental and n$_{\text{SH}}$ of the SH field, are different because of dispersion. Hence the spatial variations of the non-linear polarization and the traveling wave SH are not synchronous.

The complex amplitudes of $P^{(2)}$, SH and the fundamental fields are shown in

Eq. 2.13.

$$P^{(2)}(t,z) = \frac{1}{2}\,\epsilon_0\,d_{31}\,A_{\text{TE}}\,(\omega_{\text{f}},z)A_{\text{TM}}\,(\omega_{\text{f}},z)\,\psi_{\text{f}}^2(x,y)\,e^{-i(2\omega_{\text{f}}t\,-\,2\beta_{\text{f}}z)}\,+\,\text{c.c.}$$

$$E_{\text{SH}}(t,z) = \frac{1}{2}\,A_{\text{SH}}\,(2\omega_{\text{f}},z)\,\psi_{\text{SH}}(x,y)\,e^{-i(2\omega_{\text{f}}t\,-\,\beta_{\text{SH}}z)}\,+\,\text{c.c.}$$

$$E_{\text{TE}}(t,z) = \frac{1}{2}\,A_{\text{TE}}\,(\omega_{\text{f}},z)\,\psi_{\text{TE}}(x,y)\,e^{-i(\omega_{\text{f}}t\,-\,\beta_{\text{TE}}z)}\,+\,\text{c.c.}$$

$$E_{\text{TM}}(t,z) = \frac{1}{2}\,A_{\text{TM}}\,(\omega_{\text{f}},z)\,\psi_{\text{TM}}(x,y)\,e^{-i(\omega_{\text{f}}t\,-\,\beta_{\text{TM}}z)}\,+\,\text{c.c.}$$

(2.13)

The amplitudes A_{SH} and $A_{\text{TE,TM}}$ are the slowly varying envelopes of the SH, and the fundamental, respectively. These are complex amplitudes, and different from the Fourier amplitudes of the corresponding fields, by construction. ψ_{SH} and $\psi_{\text{TE,TM}}$ are the transverse field distributions of the SH and the fundamental, respectively. In the case of waveguides (which is the focus of this thesis), the transverse field distributions remain unchanged along the interaction region. The spatial variations of the envelopes are much slower compared to the spatial variations of the phase. In other words,

$$|\partial_z A|\ <<\ |\beta A|$$
$$|\partial_z^2 A|\ <<\ |\beta^2 A|$$

The use of slowly varying envelope approximation is justified whenever the shortest length scale of the interaction is longer (at least by an order of magnitude) than the wavelength of the field. By using the slowly varying envelope approximations for the fields and non-linear polarizations in the TE or TM equations, we finally arrive at the evolution equation for the SH and the fundamental along the interaction region as shown below.

$$\partial_z A_{\text{SH}} = \frac{i\omega_{\text{SH}}\,d_{31}\,\eta}{n_{\text{SH}}c}\,A_{\text{TE}}\,A_{\text{TM}}\,e^{i\Delta\beta z}$$

$$\partial_z A_{\text{TE}} = \frac{i\omega_{\text{f}}\,d_{31}\,\eta}{n_{\text{TE}}c}\,A_{\text{SH}}\,A_{\text{TM}}^*\,e^{-i\Delta\beta z}$$

$$\partial_z A_{\text{TM}} = \frac{i\omega_{\text{f}}\,d_{31}\,\eta}{n_{\text{TM}}c}\,A_{\text{SH}}\,A_{\text{TE}}^*\,e^{-i\Delta\beta z}$$

In the above equations the term $\Delta\beta = (\beta_{\text{TE}} + \beta_{\text{TM}} - \beta_{\text{SH}})$. η represents the overlap integral between the transverse distributions of the SH and the fundamental fields. Some remarks concerning the normalization of $A_{\text{SH,TE,TM}}$ and $\psi_{\text{SH,TE,TM}}$ follow:

$$\int \text{dxdy}\,\psi_{\text{SH,TE,TM}}^2 = 1 \qquad\qquad \Rightarrow [\psi_{\text{SH,TE,TM}}] = \frac{1}{\text{m}}$$

$$\int \text{dxdy}\,\psi_{\text{SH}}\,\psi_{\text{TE}}\psi_{\text{TM}} = \eta \qquad\qquad \Rightarrow [\eta] = \frac{1}{\text{m}}$$

$$\frac{|A_{\text{SH,TE,TM}}|^2}{2Z_{\text{SH,TE,TM}}} = P_{\text{SH,TE,TM}} \qquad\qquad \Rightarrow [A_{\text{SH,TE,TM}}] = \text{V}$$

The factor $Z_{SH,TE,TM}$ represent the wave impedances of the corresponding fields with $Z_{SH,TE,TM} = n_{SH,TE,TM}\sqrt{\frac{\mu_0}{\epsilon_0}}$. The power in the SH grows in the interaction region only if $|\partial_z A_{SH}|^2 > 0$. But due to dispersion, as explained earlier, this is not achieved. The energy is coupled back and forth between the fundamental and SH with a periodicity of $L_c = \frac{\pi}{|\Delta\beta|}$. The periodicity L_c is called the coherence length of interaction, and is the most important length scale involved. The reason for a finite L_c is chromatic dispersion. Beyond L_c, the weak non-linear polarization induced by the fundamental field grows out of phase with the SH field and hence, destructively interferes with it. In order to enable the unidirectional transfer of energy from the fundamental to the SH, L_c has to be increased. One way to achieve this is by means of quasi phase matching. In this method, the sign of the non-linear coefficient $\chi^{(2)}$ is reversed periodically along the interaction region. The periodicity of inversion is $\Lambda = 2L_c$. The propagation constant $\beta_\Lambda = \frac{2\pi}{\Lambda}$ associated with the periodicity of inversion, exactly cancels the phase mismatch $\Delta\beta$. The technique by which a periodic sign reversal is achieved is called periodic poling [12].

2.3   Quasi Phase Matching

Quasi phase matching (QPM) can be achieved in ferroelectric non-linear materials. Ferroelectric materials have a characteristic spontaneous polarization, i.e., a polarization even in the absence of external electric field [28]. The rhombohedral unit cell of $LiNbO_3$ is shown in Fig. 2.4(a) [29]. The spontaneous polarization results from the displacement of Li^+ and Nb^{5+} above or below the oxygen planes [30]. Commercially available $LiNbO_3$ is poled in such a way that these ions sit on the same side of the Oxygen plane. Periodic poling reverses the spontaneous polarization by pushing the Li ion below the nearest oxygen plane. The Nb ion is moved from a position above the center of mass of two oxygen planes to slightly below (Fig. 2.4(b)). The more detailed aspects of domain inversion and dynamics of periodic poling are active areas of research [31].

The technique of periodic poling is illustrated schematically in Fig. 2.5(a). The evolution of SH power in the QPM structure is shown in Fig. 2.5(b). In the uniformly poled structure, the growth of SH power in the first L_c is not sustained during the second L_c. However, in the periodically poled structure, the growth of SH power in the first L_c (or domain) continues further down the interaction region. The poled structure (with a few domains) shows a growth of SH power, orders of magnitude stronger than in the uniformly poled structure. This dramatically illustrates the advantage of QPM.

With periodic poling, the non-linear coefficient, $\chi^{(2)}$, varies along the interaction region as shown in Fig. 2.6(a). There is a sudden change in sign of the non-linear coefficient between the adjacent domains. The change in the sign ensures that the energy is only transferred from fundamental to SH. The Fourier decomposition of the amplitude of $\chi^{(2)}(z)$ as a function of the spatial frequency is shown in Fig. 2.6(b). The spatial variations and the spatial frequency components

(a)   (b)
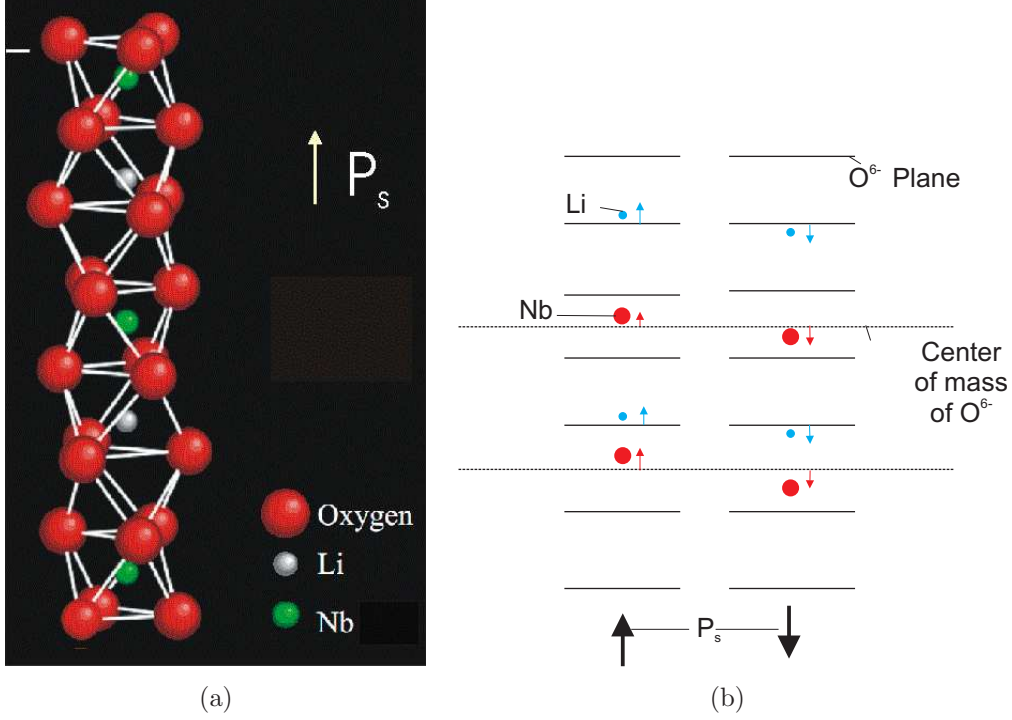
Figure 2.4: LN Structure. The spontaneous polarization arises from the displacement
of Li and Nb ions out of the oxygen plane.

(a)   (b)
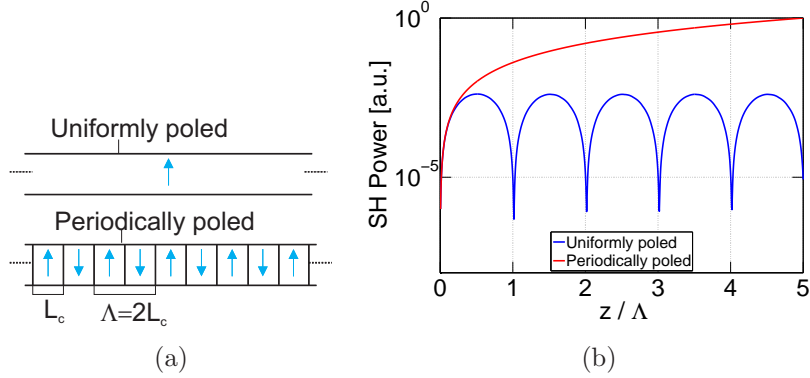
Figure 2.5: (a) The poled region with a uniform spontaneous polarization. With periodic poling, the direction of spontaneous polarization is reversed in a periodic manner. (b) The evolution of SH power in uniformly and periodically poled structure. In the uniformly poled structure, the SH power does not increase continuously. In the periodically poled structure, the SH power increases continuously.

are as follows:

$$\chi^{(2)}[z] = d_{31} \, \Box \left(\frac{z}{\Lambda} \right)$$

$$\tilde{\chi}^{(2)}[m] = 0; \qquad\qquad \text{for even m}$$

$$= \frac{2}{m\pi} d_{31}; \qquad\qquad \text{for odd m}$$

In the above equation, $\Box \left(\frac{z}{\Lambda} \right)$ is a square wave with periodicity Λ and m represents

12
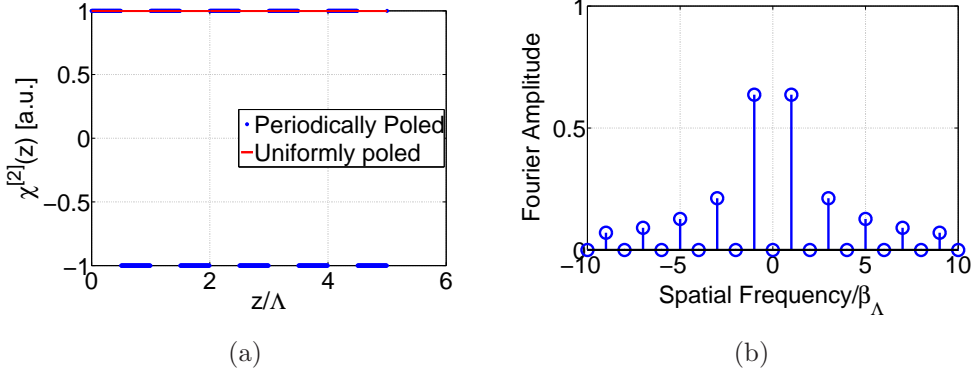
Figure 2.6: The variation of the non-linear coefficient along the interaction length is shown in Fig. (a). The Fourier amplitude distribution corresponding to a spatial frequency decomposition of the non-linear coefficient is shown in Fig. (b).

the discrete spatial frequency component. This is illustrated in Fig. 2.6.

Each of the non-zero Fourier component of the non-linear coefficient contributes to independent SH processes. The strength of the different SH processes is dependent on the Fourier component which mediates the corresponding interaction. The strongest interaction is contributed by $\tilde{\chi}^{(2)}[1] = \frac{2}{\pi}\chi^{(2)}$. This is called first order phase matching. The SH power corresponding to higher order phase matching falls off as $\frac{1}{m^2}$. We consider only the first order phase matching in this thesis. With first order phase matching, the coupled mode equations are

$$\partial_z A_{SH} = \frac{i2\omega_{SH}d_{31}\eta}{\pi n_{SH}c} A_{TE} A_{TM} e^{i(\beta_{TE}+\beta_{TM}+\beta_\Lambda-\beta_{SH})z} \tag{2.18a}$$

$$\partial_z A_{TE} = \frac{i2\omega_f d_{31}\eta}{\pi n_{TE}c} A_{SH} A_{TM}^* e^{-i(\beta_{TE}+\beta_{TM}+\beta_\Lambda-\beta_{SH})z} \tag{2.18b}$$

$$\partial_z A_{TM} = \frac{i2\omega_f d_{31}\eta}{\pi n_{TM}c} A_{SH} A_{TE}^* e^{-i(\beta_{TE}+\beta_{TM}+\beta_\Lambda-\beta_{SH})z} \tag{2.18c}$$

With an input power of P_{TE} in the TE mode and P_{TM} in the TM mode, the initial conditions for the above equations become

$$A_{SH}(0) = 0$$
$$A_{TE}(0) = \sqrt{P_{TE}(0)\, 2Z_{TE}}$$
$$A_{TM}(0) = \sqrt{P_{TM}(0)\, 2Z_{TM}}$$

The coupled mode equations (2.18) can be solved to obtain a closed form solution for the SH power. The regime where the depletion of the fundamental, due to the transfer of energy to the SH, is negligible is called Non-Depleted Pump Approximation (NDPA). With this approximation, the change in the complex amplitudes of the fundamental fields are neglected, i.e., $\partial_z A_{TE,TM} \approx 0$. For an interaction region of length L, we obtain from the coupled mode equation for

13

SH (2.18):

$$A_{\text{SH}}(\text{L}) \;=\; \kappa_{\text{SH}}\, A_{\text{TE}}\, A_{\text{TM}}\, \frac{e^{i\Delta\beta\text{L}} - 1}{j\Delta\beta} \tag{2.20a}$$

$$\Rightarrow \text{P}_{\text{SH}}(\text{L}) \;\equiv\; \frac{|A_{\text{SH}}|^2}{2Z_{\text{SH}}} \;=\; \frac{2|\kappa_{\text{SH}}|^2 Z_{\text{TE}} Z_{\text{TM}}}{Z_{\text{SH}}}\, \text{P}_{\text{TE}}\, \text{P}_{\text{TM}}\, \text{L}^2\, \text{sinc}^2\left(\frac{\Delta\beta\text{L}}{2}\right). \tag{2.20b}$$

In the above equations, $\kappa_{\text{SH}} \equiv \frac{i2\omega_{\text{SH}}\chi^{(2)}\eta}{n_{\text{SH}}c}$ and $\Delta\beta \equiv (\beta_{\text{TE}} + \beta_{\text{TM}} + \beta_\Lambda - \beta_{\text{SH}})$. It is seen that the SH power in the regime of NDPA is quadratic both in the power of the fundamental field $(\text{P}_{\text{TE}}\text{P}_{\text{TM}})$ and the interaction length (L). The wavelength dependence of the SH power is mainly described by the $\text{sinc}^2\left(\frac{\Delta\beta\text{L}}{2}\right)$ term. The spectral dependence is known as phase matching characteristic and is shown in Fig. 2.7(a).
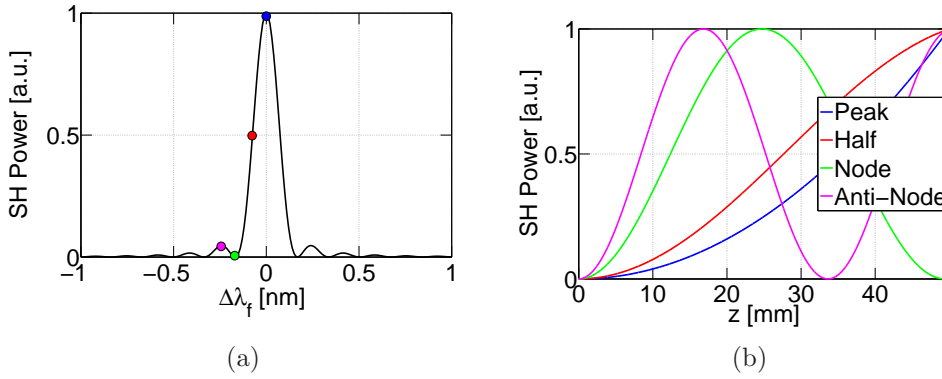
Figure 2.7: (a) Phase Matching Characteristic of SH in a 50 mm long interaction region.Dots indicate peak (blue), half power point (red), node (green) and anti-node (magenta) (b) Corresponding SH evolution in the interaction region. With exact phase matching, the SH has a parabolic profile along the interaction region ($\text{L}_c = \infty$). At the half power point, the coherence length almost equals the length of the interaction region ($\text{L}_c \approx 1.1\,\text{L}$). At the node, the energy gained by the SH along the first half is transferred back to the fundamental ($\text{L}_c = \frac{\text{L}}{2}$). The first anti-node is where the coherence length is equal to a third of the length of the interaction region ($\text{L}_c = \frac{\text{L}}{3}$). The SH power in these four cases are separately normalized to one.

It should be stressed that for a medium with infinite length of interaction, the phase matching spectrum would be a delta function peaked at the exact (quasi-) phase matched wavelength. But with finite interaction length, there is a distribution of power in the spectral range around this wavelength. The peak of the phase matching curve corresponds to the wavelength resulting in a coherence length $\text{L}_c \equiv \frac{\pi}{|\Delta\beta|} = \infty$. In this case, there is a unidirectional transfer of energy from the fundamental field to the SH. Also the rate of the transfer increases along the interaction length. This leads to a parabolic profile in the evolution of power along the interaction region. When we move away from the peak wavelength, the coherence length of interaction decreases. The half power point corresponds to the wavelength for which the coherence length is $\text{L}_c \approx 1.1\text{L}$. At this wavelength there is a uni-directional transfer of energy from the fundamental field to the SH, but the rate of transfer decreases towards the end of the interaction region.

Still further away from the main peak, the coherence length continues to decrease. The first node in the phase matching curve corresponds to a coherence length that exactly equals half the interaction length, i.e., $L_c = \frac{L}{2}$. At this wavelength, only along the first half of the interaction region, does the fundamental field transfer energy to the SH. Along the second half, the energy flows back from the SH to the fundamental field. Beyond the first node, lies the first anti-node. The coherence length in this case is $L_c = \frac{L}{3}$. A complete cycle of energy transfer is over in the initial $\frac{2}{3}$ region. The final section contributes to the SH which results in the first anti-node. In general, the nodes correspond to coherence lengths that are even divisibles of the interaction length. Similarly, the anti-nodes correspond to coherence lengths that are odd divisibles of the interaction length. These concepts are illustrated in Fig. 2.7(b). With the model presented for SH, we can look in detail at the spontaneous parametric down conversion process in detail. The next section explains the modifications required in the model to quantitatively analyze the down conversion.

2.4 Spontaneous Parametric Down Conversion

Spontaneous Parametric Down Conversion (SPDC) is the process by which a photon traveling through a non-linear medium converts spontaneously decays into two longer wavelength photons. SPDC has been reported in both second order and third order non-linear media. Unlike SH, the SPDC can be understood only from the quantum nature of electromagnetic fields. In the case of difference frequency generation for example, the generation of an idler field can be understood qualitatively as the radiation from an electron oscillating in the presence a non-linear restoring force. The electron in such a potential, when driven at both the pump and the signal frequencies, also oscillates at the beat frequency because of the non-linear restoring force. In the case of SPDC, the role of the signal and idler fields are played by the ubiquitous vacuum fluctuations of the quantized electromagnetic field [32].

In this thesis, we are focused on type II SPDC where the down-converted fields are orthogonally polarized. In order to understand the SPDC quantitatively, we still use the coupled mode equations, Eq. 2.18. The differences are only in the initial conditions of the three equations. The initial conditions are

$$
\begin{aligned}
A_{\text{TE}}(0) &= \sqrt{2Z_{\text{TE}}P_{\text{TE}}(0)} \\
A_{\text{TM}}(0) &= \sqrt{2Z_{\text{TM}}P_{\text{TM}}(0)} \\
A_{\text{P}}(0) &= \sqrt{2Z_{\text{p}}P_{\text{p}}(0)}
\end{aligned}
\tag{2.21}
$$

$Z_{\text{TE,TM,P}}$ represent the wave impedances of the corresponding fields. In the case of SPDC, the depletion of the pump can be neglected($\partial_z A_{\text{p}} \approx 0$). A closed form solution of the coupled mode equations is obtained under this condition. This is shown below.

$$
\begin{bmatrix} A_{\text{TE}}(\text{L}) \\ A^*_{\text{TM}}(\text{L}) \end{bmatrix} = \text{M} \begin{bmatrix} A_{\text{TE}}(0) \\ A^*_{\text{TM}}(0) \end{bmatrix}
\tag{2.22}
$$

where the non-unitary matrix M is given by [33]

$$
M = \begin{bmatrix} e^{\frac{i\Delta\beta z}{2}} \left(\cosh(\Gamma z) - \frac{i\Delta\beta}{2\Gamma}\sinh(\Gamma z) \right) & e^{\frac{i\Delta\beta z}{2}} \left(-\frac{i\kappa_{TE} A_p}{\Gamma}\sinh(\Gamma z) \right) \\ e^{-\frac{i\Delta\beta z}{2}} \left(\frac{i\kappa_{TM}^* A_p^*}{\Gamma}\sinh(\Gamma z) \right) & e^{-\frac{i\Delta\beta z}{2}} \left(\cosh(\Gamma z) - \frac{i\Delta\beta}{2\Gamma}\sinh(\Gamma z) \right) \end{bmatrix} \quad (2.23)
$$

The matrix M is non-unitary , because the total number of photons at the input and output is different. The constant $\Gamma = \sqrt{\kappa_{TE}\kappa_{TM}^*| A_p |^2 - \left[\frac{\Delta\beta}{2} \right]^2}$ is a gain co-efficient and peaks at the exact (quasi-) phase matched wavelength. The non-unitary matrix M is a characteristic of transformations in which the metric $|A_1|^2 - |A_2|^2$ is preserved (for example Lorentz transformation). In the context of SPDC, this means that the increase in photon number in the TE mode must exactly equal the input in the photon number in the TM mode [34]. In a fully quantized picture, the slowly varying amplitudes $A_{TE,TM}$ and $A_{TE,TM}^*$ are replaced by the operators $\hat{a}_{TE,TM}$ and $\hat{a}_{TE,TM}^\dagger$, respectively. The operators $\hat{a}$ is the annihilation operator and the operator $\hat{a}^\dagger$ is the creation operator. A detailed description of the quantum nature of down conversion is given in Appendix 1. In the quantum picture, the transformation of the operators is given by

$$
\begin{bmatrix} \hat{b}_{TE} \\ \hat{b}_{TM}^\dagger \end{bmatrix} = M' \begin{bmatrix} \hat{a}_{TE} \\ \hat{a}_{TM}^\dagger \end{bmatrix} \quad (2.24)
$$

where $\hat{b}_{TE,TM}$ are the annihilation operators of the normal modes after transformation. The matrix M' is similar to M. But the coefficients $\kappa_{TE,TM}$ are renormalized to $\kappa \equiv \frac{i2\sqrt{\omega_{TE}\omega_{TM}}\chi^{(2)}\eta}{\sqrt{n_{TE}n_{TM}}c}$ [35]. This is necessary to preserve the commutation relations between the operators. The generated photon number per normal mode is

$$
\begin{aligned} \langle \hat{b}_{TE}^\dagger \hat{b}_{TM} \rangle &= |M_{12}|^2 \\ &= \left| \frac{\kappa A_p}{\Gamma}\sinh(\Gamma L) \right|^2 \end{aligned} \quad (2.25)
$$

Here normal mode implies a mode with well-defined frequency and propagation constant. It should be emphasized that even in a single mode waveguide, there exists many normal modes. The term single mode only implies that the transverse distribution of fields at different frequencies are the same. The result shows that only the off-diagonal elements of the matrix M' contribute to the generation of photons after interaction. This is clear because the non-linear interaction does not amplify the vacuum fluctuations in a mode, but only couples it with another, that satisfy energy and momentum conservation. A formal proof is shown by Suhara [35].

The classical equations are still used to obtain a quantitative estimate of the SPDC. For this, the vacuum fluctuations have to be introduced into the initial conditions $A_{TE}(0)$ and $A_{TM}(0)$. The vacuum fluctuations contribute an energy equal to that of a photon in any normal mode. Consider the case when the interaction region is pumped by a continuous wave laser. The down-converted fields have a finite spectrum because the single frequency pump is interacting with

broad band vacuum fluctuations. The width of the down-converted spectrum is limited only by the phase matching condition. More specifically, the group index difference between the TE and TM modes limits the emission spectrum. The spectral profile in the limit $\Gamma L \approx \frac{\Delta\beta L}{2}$ (small pump approximation) is a sinc^2 function. The FWHM of emission $\Delta\omega$ is equal to $\Delta\omega = \frac{2.8c}{[n_{\text{TE,G}} - n_{\text{TM,G}}]L}$, where $n_{\text{TE,TM,G}}$ represent the group indices of TE and TM modes.

The spectrum is simulated with finite resolution($\Delta\omega$). A normal mode is associated with each slice of the spectrum. The spectral power density of the vacuum fluctuation is $\partial_\omega P(\omega) = \hbar\omega$. The initial conditions are then given by two sets of equations, one for TE spectrum and the other for TM spectrum:

$$A_{\text{TE}}(0) = \sqrt{2Z_{\text{TE}}\,\hbar\omega_{\text{TE}}\,\Delta\omega} \qquad A_{\text{TE}}(0) = 0 \qquad\qquad (2.26a)$$

$$A_{\text{TM}}(0) = 0 \qquad\qquad A_{\text{TM}}(0) = \sqrt{2Z_{\text{TM}}\,\hbar\omega_{\text{TM}}\,\Delta\omega} \qquad (2.26b)$$

$$A_{\text{P}}(0) = \sqrt{2Z_{\text{p}}P_{\text{p}}} \qquad\qquad A_{\text{P}}(0) = \sqrt{2Z_{\text{p}}P_{\text{p}}} \qquad\qquad (2.26c)$$

In order to evaluate the TE spectrum, $A_{\text{TE}} = 0$, and in order to evaluate TM spectrum, $A_{\text{TM}} = 0$. This is necessary because the quantum model shows that only the cross-terms contribute to the increase in photon number. Calculated spectrum of type II down conversion is shown in Fig. 2.8(a). A continuous wave pump with $\lambda_{\text{p}} = 776.5\,\text{nm}$ and $P_{\text{p}} = 10\,\text{mW}$ is used. A waveguide segment of length $L = 50\,\text{mm}$ with a domain periodicity $\Lambda = 9.35\,\mu\text{m}$ and temperature $= 174\,^\circ\text{C}$ is modeled. The coupling coefficient, $\kappa_{\text{TE}} \approx \kappa_{\text{TM}} = 0.6\,\frac{1}{\text{V·m}}$ The FWHM of the spectrum $\Delta\lambda \approx 0.6\,\text{nm}$. The conversion efficiency is given by the ratio $\eta = \frac{P}{P_{\text{p}}} \approx \frac{122\,\text{pW}}{10\,\text{mW}} \approx 10^{-9}$. The spectral power density $\partial_\omega P(\omega) = 200\,\frac{\text{pW}}{\text{nm}}$.
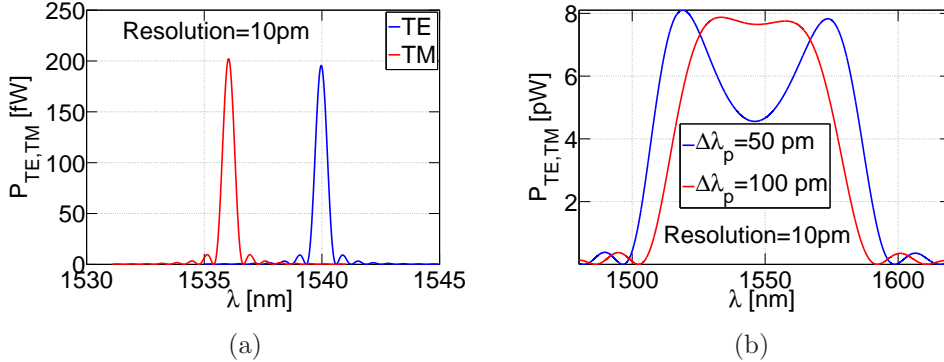
Figure 2.8: (a) Calculated spectra of Type II SPDC. (b) Calculated spectra of Type I SPDC ($\Delta\lambda_{\text{p}}$ is the de-tuning of pump wavelength from degeneracy point). Both calculations are done with $P_{\text{p}}(0) = 10\,\text{mW}$ and $L = 50\,\text{mm}$ (see text for more details).

The spectrum of type I down conversion is shown in Fig. 2.8(b). The simulation parameters are the same as for type II down conversion. The type I down conversion has infinite bandwidth at degeneracy point because of equal group velocities of both photons (both photons are emitted into the same normal mode). The simulations correspond to a pump wavelength offset from the degeneracy point by $\Delta\lambda_{\text{p}} = 10\,\text{pm}$ and $\Delta\lambda_{\text{p}} = 50\,\text{pm}$. The poling periodicity is $\Lambda = 18.2\,\mu\text{m}$. Compared to type II process, type I has higher conversion efficiency and broader

emission. The conversion efficiency is estimated to be $\eta = 5 \times 10^{-6}$. The emission bandwidth is $\Delta\lambda \approx 62\,\mathrm{nm}$. The spectral power density $\partial_\omega \mathrm{P}(\omega) = 780\,\frac{\mathrm{pW}}{\mathrm{nm}}$. It is seen that the spectral power densities of type I and type II processes agree with in one order of magnitude. In quantum optics experiments, the spectral power density of down conversion is more important than the absolute value of conversion efficiency. Even though the conversion efficiency of type I process is higher, spectral filtering has to be done behind the source to improve the coherence time/length of the photons generated. The spectral filtering may introduce insertion loss as well. With type II process of smaller emission bandwidth the need for spectral filtering can be avoided. Also the orthogonality of the polarizations help in easier spatial separation of the down-converted photons. In this thesis, we concentrate on type II down conversion.

The Table 2.1 compares the efficiency of down conversion realized in bulk non-crystals. It is seen that the waveguides provide efficiency at least three orders higher than the bulk crystals. The main reasons for the better efficiency with waveguide is two-fold. The interacting fields are confined in a very small volume. The efficiency goes as the square of effective interaction cross-section. Also, the effective cross-section is maintained over a long propagation length without divergence by diffraction. The efficiency goes as the square of the interaction length. Thus waveguide devices work with high efficiency at low power.

Reference	Medium	Mechanism	Efficiency
Tittel [36]	KNbO$_3$	Type I 1310 nm	1.9×10^{-10}
Kwiat [37]	BBO	Type I, 702 nm	3.4×10^{-11}
Zeilinger [38]	BBO	Type II, 702 nm	8.1×10^{-13}
Kumar [39]	DSF	FWM, 1550 nm	10^{-10}

Table 2.1: Comparison of spontaneous parametric down conversion efficiencies realized in bulk crystal and optical fiber. Both type I and type II results are listed. The results of bulk crystals are at least three orders smaller compared to the waveguides. In optical fiber, similar efficiency is achieved. (DSF: Dispersion Shifted Fiber, FWM: Four Wave Mixing)

Down conversion by spontaneous four wave mixing enabled by Kerr non-linearity in optical fibers has been reported by Kumar [39]. The fiber based source can be spliced to a standard telecom fiber component with negligible loss. A fiber based, polarization entangled photon pair source has also been reported [40]. However, spontaneous Raman scattering co-exists with the four wave mixing resulting in spurious photons. This limits the quality of entanglement.

In this thesis, Chapters 3 discusses an integrated photon pair source and Chapter 4 discusses an entangled photon pair source. Both sources generate single photon states that are realized by using down conversion. However, the joint state, $|\psi\rangle_{12}$, of the photon pairs realized by down conversion is not a single photon state, but has a Bose-Einstein distribution over the number states [35].

$$|\psi\rangle_{12} = \mathrm{sech}\,(\Gamma L) \sum_{n=0}^{n=\infty} \tanh^n (\Gamma L)\, |n\rangle_1 |n\rangle_2 \qquad (2.27)$$

The probability of seeing n photon pairs, P_n, during a measurement window is proportional to the coefficient of the state $|n\rangle_1 |n\rangle_2$

$$P_n = |_1\langle n|_2 \langle n| |\psi\rangle_{12}|^2$$
$$= |\text{sech}\,(\Gamma L) \tanh^n (\Gamma L)|^2$$

With high pump power there is a probability that more than one photon pair is generated. If the pump power is too low, the probability of generating a single pair is reduced. Hence, it is necessary to find a compromise between the pair generation rate and the probability to generate more than one photon pair.

(a)

(b)

(c)
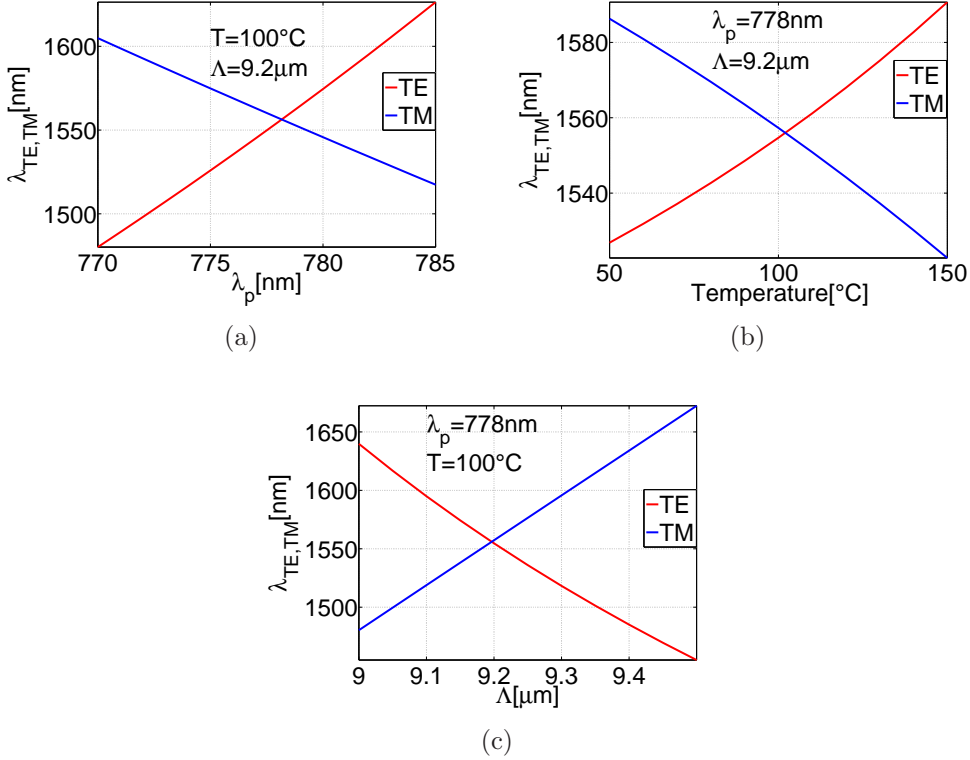
Figure 2.9: (a) Pump wavelength tuning of emission wavelengths. The slope of TE emission is $\partial_{\lambda_P} \lambda_{TE} = 10$ and the slope of TM emission is $\partial_{\lambda_P} \lambda_{TM} = -5$. (b) Temperature tuning characteristics of emission wavelengths. λ_{TE} changes with $\partial_T \lambda_{TE} = 0.6 \frac{nm}{°C}$ and λ_{TM} changes with $\partial_T \lambda_{TM} = -\partial_T \lambda_{TE}$. (c) Change in emission wavelength with change in domain period, Λ. The slope of TE emission is $\partial_\Lambda \lambda_{TE} = -0.4$ and the slope of TM emission is $\partial_\Lambda \lambda_{TM} = -\partial_\Lambda \lambda_{TE}$.

The thesis considers photon pairs generated in the standard telecommunication band ($\lambda \approx 1550$ nm). Down conversion is achieved in this range by using a pump wavelength, $\lambda_p \approx 775$ nm range. The domain periodicity Λ to achieve quasi phase matching is $\Lambda \approx 9\,\mu$m. The photon pairs generated can be tuned over a wide range by changing the pump wavelength, temperature or the domain period. The dependence of the emission wavelengths $\lambda_{TE,TM}$ on λ_p is shown in Fig. 2.9(a). The slope of the TE emission is $\partial_{\lambda_P} \lambda_{TE} = 10$ and the slope of TM emission is $\partial_{\lambda_P} \lambda_{TM} = -5$. Even though the linearity of the tuning characteristics is advantageous in some applications, the steep slope also points to

19

the necessity of stabilizing the pump wavelength in applications where precise emission wavelengths are required. Unlike with change of the pump wavelength, the change of the emission wavelength with temperature is slower, as shown in Fig. 2.9(b). The slope of TE emission is $\partial_T \lambda_{TE} = 0.6 \frac{nm}{°C}$ and that of TM emission is $\partial_T \lambda_{TM} = -\partial_T \lambda_{TE}$. The temperature of the sample should be stabilized to achieve stable emission wavelengths. The relatively slow variation of the tuning characteristic allows to fine-tune the emission wavelength, which is more difficult with pump wavelength tuning. As already mentioned, the required domain period to achieve down-conversion in the 1550 nm range is $\Lambda \approx 9\,\mu m$. It is helpful to fabricate waveguides with different periodicities so that the required emission wavelengths can be achieved with minimal tuning of pump wavelength or temperature. This may be required because commercially available tunable laser sources at λ_p have limited tuning range. Also the pump power is not uniform over the whole range. The slope of TE emission with domain period is $\partial_\Lambda \lambda_{TE} = -0.4$ and that of TM emission is $\partial_\Lambda \lambda_{TM} = -\partial_\Lambda \lambda_{TE}$. Type II down conversion has been reported in 1310 nm range (also interesting because of zero dispersion of optical fibers) using a domain periodicity, $\Lambda \approx 6\,\mu m$ [41].

Conclusion

Detailed theoretical model of the Ti:LiNbO$_3$ waveguide is presented. The origin of second order non-linear polarization in LiNbO$_3$ is briefly discussed with the help of the crystal structure. Concept of quasi phase matching is explained in detail using coupled mode equations, with second harmonic generation as an example of the non-linear process in the waveguide. Finally, calculations concerning efficiency, bandwidth and tuning characteristics of spontaneous parametric down conversion is reported. The calculations are compared with the results in other non-linear media.

Chapter 3

Titanium In-diffused Periodically Poled Lithium Niobate Waveguides

The fabrication of Ti in-diffused periodically poled LiNbO$_3$ waveguides are explained in this chapter. The basic characterization mechanisms are also summarized. The first section briefly presents the waveguide fabrication technique. The second section discusses the periodic poling of the waveguide. Theoretical and experimental aspects of waveguide loss measurement are discussed in section three. Mode size measurement results are reported in section four. A comparison with the measured mode size of an optical fiber is also given.

3.1 Fabrication
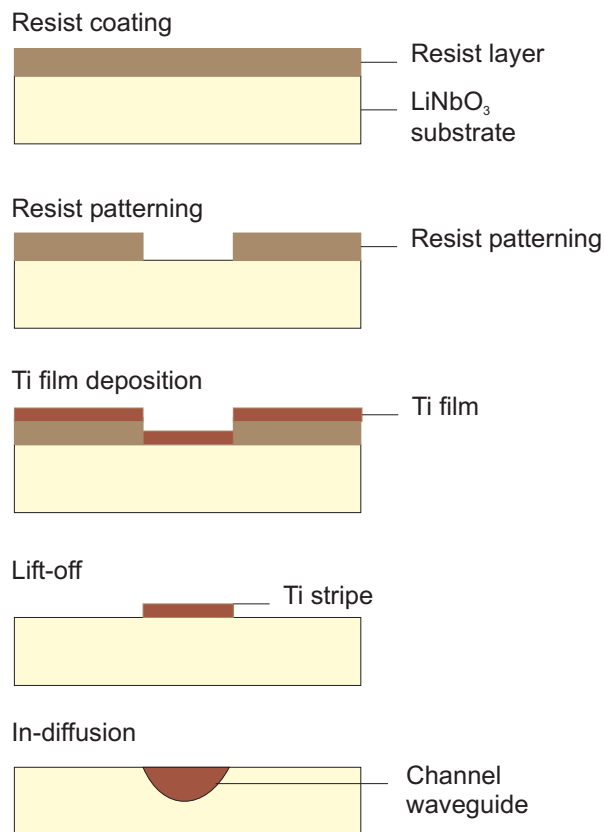
Figure 3.1: Steps involved in waveguide fabrication.

Channel waveguides are fabricated by diffusing Ti into LiNbO$_3$ substrate. Light is confined because of the phenomenon of total internal reflection resulting from an increased refractive index in regions where Ti is in-diffused . The

basic steps of the fabrication of Ti:LiNbO$_3$ waveguides are shown schematically in Fig. 3.1 [42]. We start with a photo-lithographically defined waveguide pattern on the substrate. Later, Ti film is deposited by an evaporation technique. By lift-off Ti is removed leaving a metalized pattern corresponding to the waveguide. The diffusion is done at 1060 °C for about 9 hours. The diffusion is done on the -Z face of the sample. The width of the Ti stripe is chosen to be 5, 6 or 7 μm. The thickness of the stripe is about 90 nm. These fabrication parameters are chosen such that we obtain single mode operation at 1550 nm.

3.2   Periodic Poling
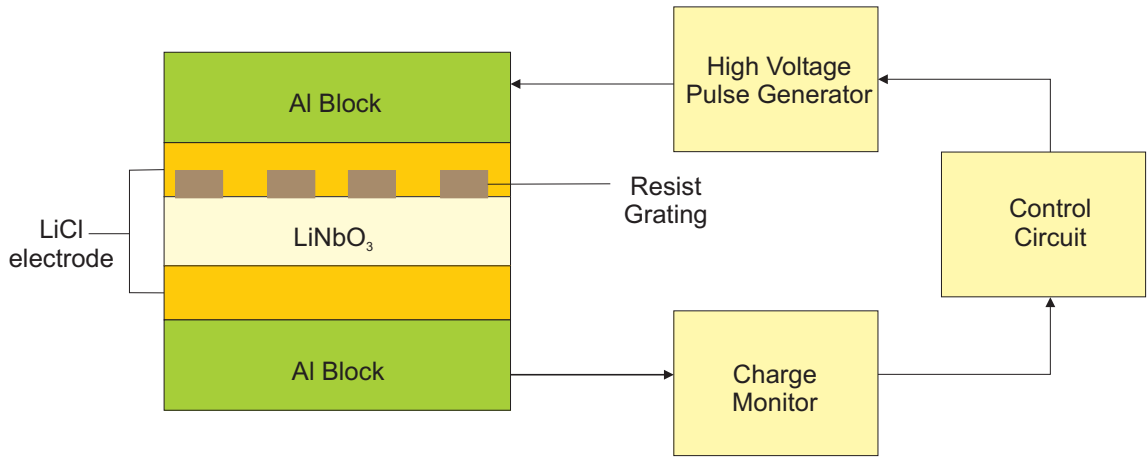
Figure 3.2: Steps involved in waveguide fabrication. See text for details.

After the waveguide fabrication, the sample is periodically poled. The schematic of the set-up used for periodic poling is shown in Fig. 3.2. In order to obtain a 50% duty cycle with periodic poling, it is essential that the duty cyle on the photomask is less than 50%. The photoresist is immersed in the electrode used for poling (LiCl dissolved in isopropyl alcohol). A voltage pulse, from the high voltage generator, is applied so that the coercive field of LiNbO$_3$ (21 $\frac{kV}{mm}$) is exceeded [42]. The poling is controlled by monitoring the current flow in the external circuit. The charge associated with spontaneous polarization(P$_s$) is about $\approx 70 \frac{\mu C}{cm^2}$. If A is the total surface area of the electrode, the total charge on the +Z face is reduced by 2P$_s \times$A. The poling is stopped when the charge flowing through the external circuit exactly equals this value, that is, when $\int dt\ i(t) = 2P_s \times A$.

3.3   Loss Measurement

A clever method to measure the scattering losses in the Ti:LiNbO$_3$ waveguides is shown in [43]. The technique is to look for the visibility of the Fabry-Perot resonances seen by temperature tuning the sample. However, the method is limited to only single mode waveguides. This is a draw back of the scheme because non-linear
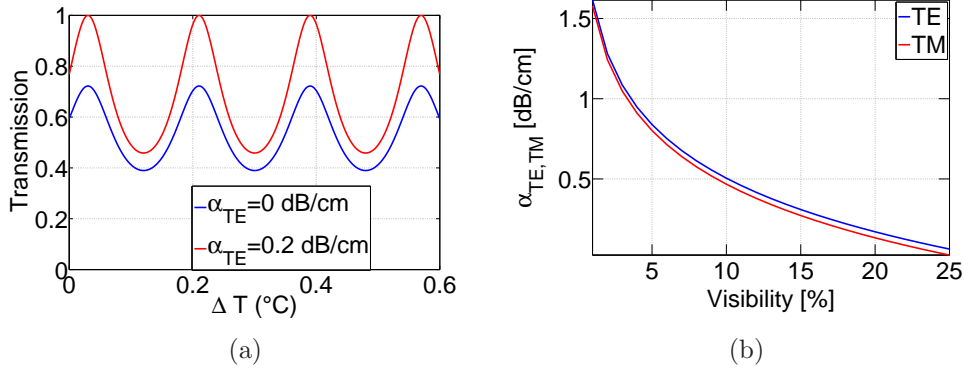
Figure 3.3: (a)Calculated FP resonances obtained by temperature tuning (ΔT). The visibility of the resonance is higher when the scattering loss is smaller. With no scattering loss, the visibility is limited by the finite reflectivity at the end-faces of the waveguide. (b) Calculated scattering loss as a function of the visibility for TE and TM polarizations. The waveguide length is L $= 90\,\mathrm{mm}$ and $\lambda = 1550\,\mathrm{nm}$.

processes usually involve widely separated wavelengths. For example, second harmonic generation experiments considered in this thesis involves $\lambda_\mathrm{f} \approx 1550\,\mathrm{nm}$ and $\lambda_\mathrm{SH} \approx 775\,\mathrm{nm}$ with, with waveguides multi-mode at the second harmonic wavelengths. In this case, only the scattering losses at λ_f are measured.

By tuning the temperature, we observe the Fabry-Perot resonances as shown in Fig. 3.3(a). With scattering loss, the visibility in the resonance comes down to 30 % (blue curve). Without scattering loss, the visibility is about 37 % (red curve). The scattering loss (α), can be derived from the transmission characteristic of a Fabry-Perot cavity and is given by

$$
\begin{aligned}
\alpha \, \left[\frac{\mathrm{dB}}{\mathrm{cm}} \right] &= \frac{4.34}{\mathrm{L}} \, \left[\ln \mathrm{R} \, + \, \ln 2 \, - \, \ln \mathrm{V} \right]. \\
\mathrm{V} &= \frac{\mathrm{T_{max}} - \mathrm{T_{min}}}{\mathrm{T_{max}} + \mathrm{T_{min}}}.
\end{aligned}
\tag{3.1}
$$

R is the wavelength and polarization dependent reflectivity at the end-faces of the waveguide, V is the visibility calculated from maximum ($\mathrm{T_{max}}$) and minimum ($\mathrm{T_{min}}$) of transmission. The dependence of the scattering loss on the visibility is shown in Fig. 3.3(b). The calculation is for a 90 mm long waveguide at $\lambda = 1550\,\mathrm{nm}$.

Scattering loss measurements were done in waveguides which are single mode at 1550 nm. The experimental set up is shown schematically in Fig. 3.4. Light from External Cavity Laser (ECL) at $\lambda = 1550\,\mathrm{nm}$ is coupled into the waveguide by using an in-coupling lens ($\mathrm{L_1}$). ECL is preferred because the coherence length of such a source is much longer than the length of the sample ($< 10\,\mathrm{cm}$). The light from the waveguide is collected using an out-coupling lens ($\mathrm{L_2}$). InGaAs PIN photo-diode is used to measure the light collected by $\mathrm{L_2}$. A He-Ne laser at 632 nm is used for aligning the sample. For reliable measurement of scattering loss, it is essential that the ECL is stabilized to single longitudinal mode of operation. Using
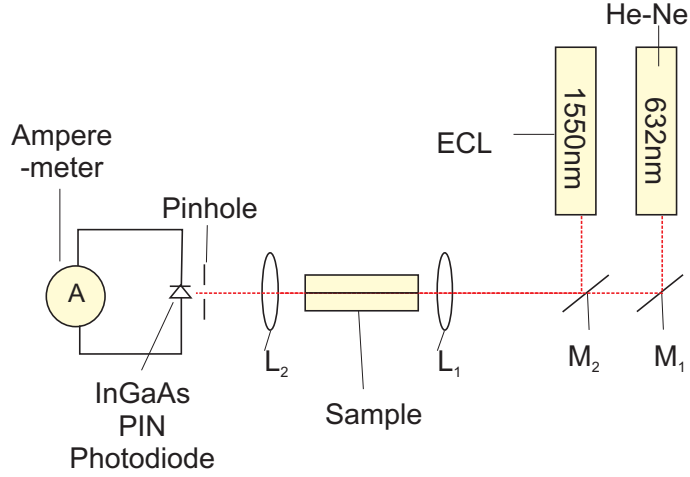
Figure 3.4: Schematic of the loss measurement setup.

(a)

(b)
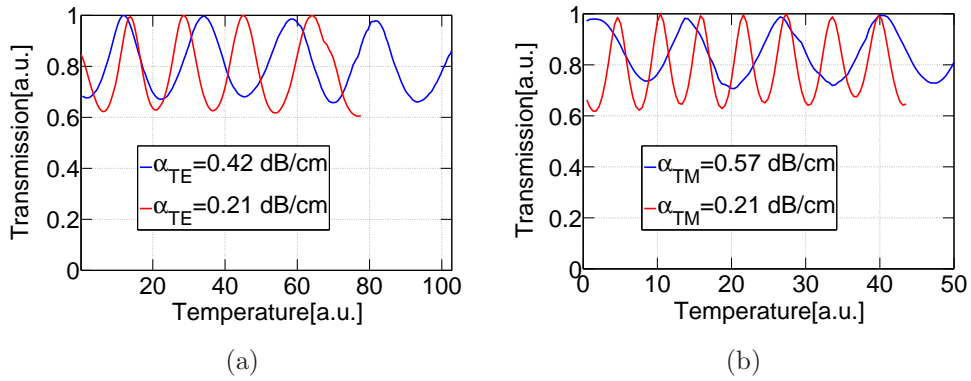
Figure 3.5: (a) Temperature tuning characteristics of the sample with TE polarized light. (b) Temperature tuning characteristics of the sample with TM polarized light.

a pinhole in-front of the detector helps to block the guided substrate modes which are collected by L_2. The temperature tuning characteristic is measured while heating the sample by passing current through the Peltier elements attached to the sample holder. The result is shown in Fig. 3.5(a). The measurement was done on two different waveguides on the sample Pb 906z.

3.4 Mode Size Measurement

A second important characterization step is to measure the near field intensity profile of the guided mode in the waveguide. The measurements of the intensity profiles of two different polarizations let us calculate their overlap integral, an important parameter which determines the efficiency of the non-linear process. The measurement also help us to obtain an upper limit for coupling the light from the waveguide into standard single mode fibers.

The setup used to measure the near field intensity profile is shown in Fig. 3.6.
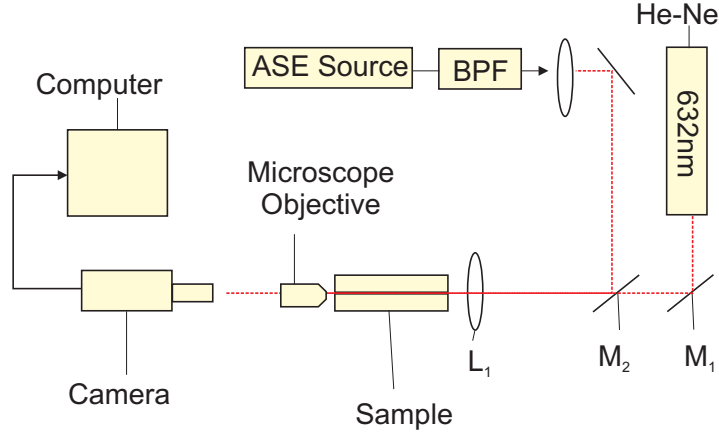
Figure 3.6: Schematic of the mode measurement setup.

Instead of a single mode ECL, a broad band amplified spontaneous emission (ASE) source is used to measure the mode profile. The broadband source is used so that unwanted interference effects in the optical path can be eliminated, which would otherwise affect the mode size measurement. The ASE source has a band width of ≈ 30 nm. Such a broad emission is undesirable because the mode size change with wavelength. A Band Pass Filter (BPF) with a band width of ≈ 1 nm is used. With 1 nm the coherence length is short enough (≈ 2.4 mm) to eliminate any interference effects in the optical path without introducing any errors in the measurement due to dispersion. A microscope objective collects the light from the waveguide. The use of a microscope objective provides better resolution. The numerical aperture of the objective is 0.9. The light collected using the objective is later imaged on a camera.

(a)

(b)
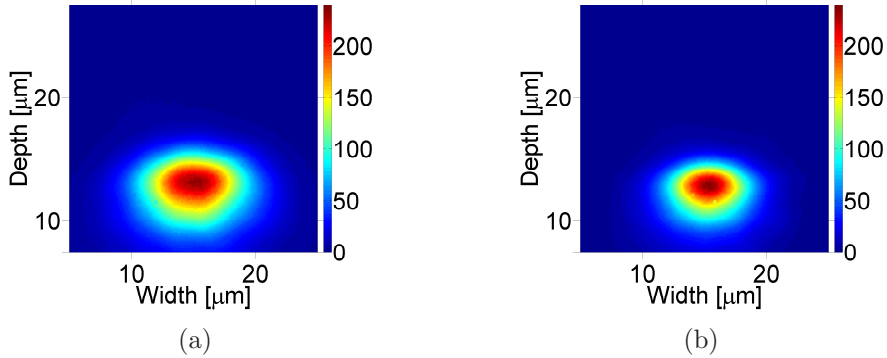
Figure 3.7: (a) Measured mode profile of a TE polarized field. (b)Measured mode profile of a TM polarized field. Both measurements correspond to a $5\mu m$ wide waveguide at wavelength $\lambda = 1550$ nm. The waveguide is single mode for both fields.

The measured mode profiles of a $5\ \mu m$ waveguide is shown in Fig. 3.7(a) and Fig. 3.7(b). Mode size of the TE polarized field is larger than that of TM polarized field. This is because, the increase in the refractive index by Ti in-diffusion is larger for extra-ordinary index compared to the ordinary index (refer Chapter 1 for details). The mode sizes of the TE and TM modes obtained from these
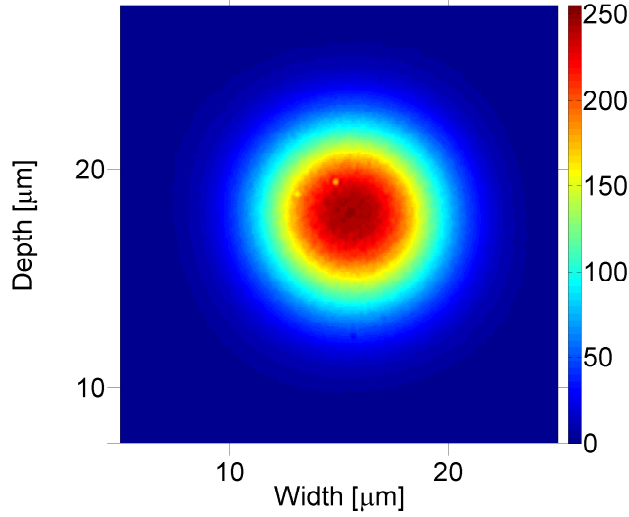
Figure 3.8: Measured mode profile of Leoni-E9/125 optical fiber at $\lambda = 1550$ nm. The fiber is single mode at 1550 nm. For details see Table 3.1.

measurements is summarized in the table 3.1.

parameter	TE [μm]	TM [μm]	Fiber [μm]
FWHM [H]	6.9	5.1	6.6
FWHM [V]	5.0	3.8	6.8
$\frac{1}{e^2}$ Width	13.4	10.3	10.6
$\frac{1}{e^2}$ Width	10.3	8.0	11.0

Table 3.1: Measured mode size of TE and TM polarized modes at $\lambda = 1550$ nm. Also the measured mode size of a standard single mode fiber is shown. FWHM: Full Width at Half Maximum.

Waveguide modes in either polarization is asymmetric because the Ti indiffusion profile lacks symmetry. When the light from the waveguide is coupled into a standard single mode fiber (fiber modes have circular symmetry around the core), coupling loss results from the mode mismatch. In order to look at the overlap integral of the fiber mode and the waveguide modes, and hence obtain a quantitative estimate of the coupling efficiency, the mode distribution of an optical fiber (Leoni-E9/125) is studied. The measured mode profile of the fiber is shown in Fig. 3.8 and the half-widths are summarized in Table 3.1. We define the polarization dependent overlap integral $\eta_{\text{TE,TM}}$ between the fiber mode and the waveguide mode as follows:

$$\eta_{\text{TE,TM}} = \left| \int \mathrm{dxdy}\, \psi_{\text{TE,TM}}\, \psi_{\text{Fiber}} \right|^2 \qquad \text{with the normalizations,}$$

$$\int \mathrm{dxdy}\, |\psi_{\text{TE,TM,FIBER}}|^2 = 1$$

(3.2)

In the above equations, $\psi_{\mathrm{TE,TM}}$ represents the TE and TM mode fields and ψ_{Fiber} represents the mode field of the fiber. A direct determination of the coupling efficiencies using the measured intensity distributions over-estimates η due to the limited resolution of the imaging system. A more reliable approach is to use approximate solutions for field distributions of Ti-diffused waveguides (with FWHM fitted to the measured results) and then calculate the efficiencies. The results are shown in Table 3.2. Please note that losses due to Fresnel reflections are not included in the calculations.

Polarization	$\eta\,[\%]$
TE	92
TM	78

Table 3.2: Coupling efficiency of the waveguide modes and the fiber mode estimated from the measured data. The coupling efficiency is higher for the TE mode compared to TM mode. Losses due to Fresnel reflection are not included in the calculation.

Conclusion

The chapter presented basic steps in waveguide fabrication and periodic poling. Characterization of the waveguide losses of TE and TM polarized modes were also discussed. Mode size measurement results of TE and TM polarized fields were explained. The mode size of a standard single mode fiber was measured and the overlap with the waveguide modes were calculated.

Chapter 4

Photon Pair Source with Integrated Polarization Splitter

In this chapter, the development of a packaged integrated photon pair source based on spontaneous parametric down conversion is reported. The source consists of a periodically poled Ti:LiNbO$_3$ waveguide combined with a polarization splitter on the same substrate. A dielectric end-face mirror suppresses the residual pump. Single mode fiber pigtails at the input and output of the waveguide results in stable operation.

In the first section, the design and fabrication of the source is explained. The second section presents the characterization of the waveguide by second harmonic generation and spontaneous parametric down conversion experiments. Theoretical and experimental investigations of the polarization splitter is discussed in the third section. The details of pigtailing and packaging of the source is reported in the fourth section. The fifth and final section summarizes the results of photon pair generation experiments. The results are compared with those of other sources.

4.1   Design and Fabrication

The schematic of a conventional photon pair source is shown in Fig. 4.1. The source consists of a non-linear crystal in which the photon pairs are generated. The generated photon pairs are orthogonally polarized. A polarization beam splitter is kept behind the source to spatially separate the orthogonally polarized photons. The arrival time of the photons in a pair, behind the splitter are the same. In other words, detection of one photon heralds the arrival of the other. A pump suppression scheme is also required. Otherwise, the residual pump photons reaching the detector degrades the arrival time correlation between the photons in a pair. The use of a waveguide structure in the bulk non-linear crystal helps to increase the efficiency of the non-linear process [14; 44]. However, in the conventional schemes, the photon pair generation, polarization splitting and the residual pump suppression are realized using different components. This leads to problems concerning the stability of such a source for long term operation. In our approach, we combine the photon pair generation, polarization splitting and pump suppression on the same substrate [45]. Moreover, the source is fiber pigtailed at the input and output ports. This facilitates easier integration with standard telecom components used in quantum key distribution systems.

As shown in the schematic, the pump light($\lambda_{\rm p} = 780$ nm) is coupled into the waveguide using a polarization maintaining single mode fiber(PMF). Both fiber and waveguide end-faces are angle polished to avoid back-reflections into the fiber.
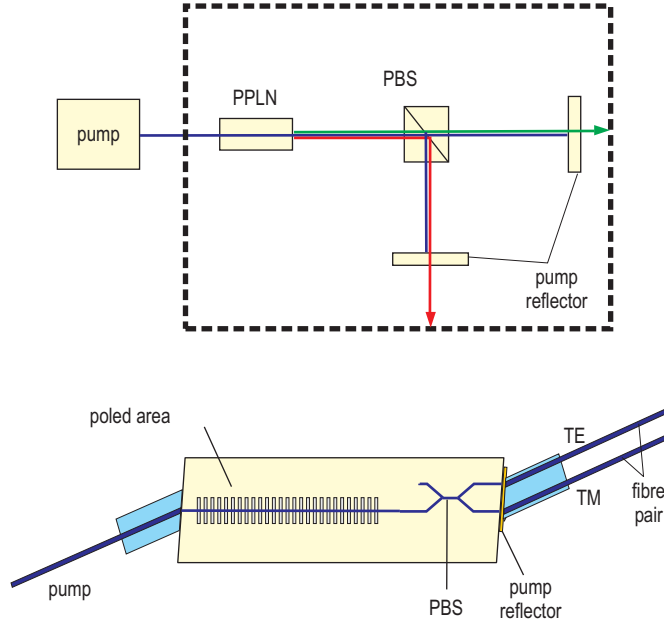
Figure 4.1: (a) Conventional scheme to realize a photon pair source. A non-linear crystal generates the photon pairs. The photon pairs are spatially separated externally using a polarization beam splitter. Pump suppression is also achieved externally. (b) Integrated fiber pigtailed photon pair source. The photon pair generation, spatial separation and pump suppression are realized on the same substrate. More over, the source is fiber pigtailed at the input and output.

The waveguide is fabricated by the in-diffusion of a photo-lithographically defined $7\,\mu$m wide, 90 nm thick Ti stripes for 9 hours at 1060 °C. Afterwards, a waveguide section of 66 mm length is periodically poled with a periodicity of 9.1 μm to obtain type II quasi phase matched SPDC with signal and idler wavelengths around 1560 nm(waveguide temperature $\approx 50°$C). The orthogonally polarized signal and idler photons generated in the Ti:PPLN waveguide are separated by a specially designed directional coupler operating as polarization splitter. In order to obtain the best performance, splitter with different design parameters are fabricated on the same sample and tested. The layout of the sample is shown in Fig. 4.2. On the waveguide end face, a dielectric mirror is deposited to reflect the residual pump. The spatially separated photons are butt-coupled to two standard single mode fibers embedded in a glass ferrule. The integrated photon pair source is packaged in an Al-housing, with provision for stabilizing the substrate temperature.

4.2 Waveguide Characterization

Scattering losses of the different waveguides in the sample are estimated from the visibility seen in the temperature tuning characteristic of the sample. This was necessary to identify the best structure for fiber pigtailing. However, it is not possible to measure the scattering loss of the composite structure by this method. Hence, a waveguide without subsequent polarization splitter, fabricated as a control guide and adjacent to the relevant composite structure, is chosen to
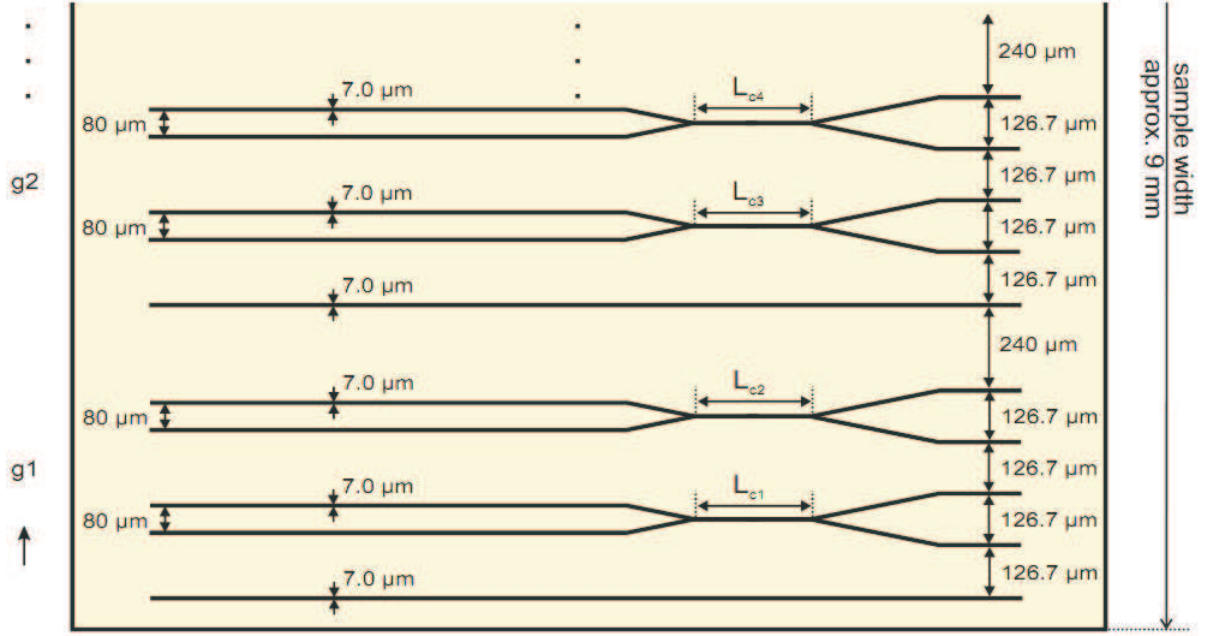
Figure 4.2: Layout of the sample used for pigtailing. There are 12 groups on the sample with each group containing 2 integrated structures and 1 test waveguide. The polarization splitters in the integrated structures have different coupling lengths. The length of the poled region is $L = 66$ mm. Preliminary investigations are done on a test waveguide instead of an integrated structure.

measure the scattering loss. The best waveguide in the sample showed a scattering loss of $\alpha_{\text{TE}} = 0.2\,\frac{\text{dB}}{\text{cm}}$ in the TE polarization and $\alpha_{\text{TM}} = 0.25\frac{\text{dB}}{\text{cm}}$ in the TM polarization. Further, the efficiency of the SH and SPDC is measured.

Second Harmonic Generation

The second harmonic(SH) measurement of the waveguide is important because it gives an estimate of the efficiency of non-linear processes in the waveguide. Also, the measurement helps to identify the degeneracy point in the reverse process of spontaneous parametric down conversion. The set-up used to measure the SH is shown below.

Light from the ECL ($\lambda = 1550$ nm) is used as the fundamental power. Light from a He-Ne laser is used for alignment purposes. A fiber polarization controller is used to control the polarization of light from the ECL. Mirrors M_1 and M_2 are used to redirect the light collimated by the lens L_1. The light is coupled into the sample by using a lens which is anti-reflection coated for 1550 nm (L_2). The SH generated is collected using a lens which is anti-reflection coated for $\lambda = 775$ nm (L_3). Finally, the SH is measured using a Si photo-diode as detector. The measured SH phase matching spectrum of the waveguide with poling period $\Lambda = 9.05\,\mu$m is shown in Fig. 4.4. The temperature of the waveguide is maintained at 40°C. The SH efficiency is calculated from the SH power at the peak of the curve (P_{SH}) and the fundamental power estimated to be coupled into the waveguide($P_f = 0.8$ mW).
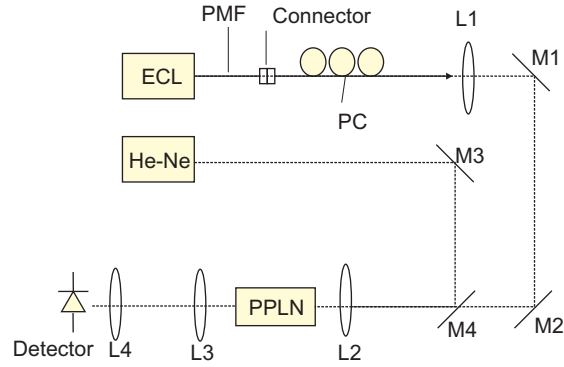
Figure 4.3: Set up for second harmonic generation and measurement. The fundamental field from the ECL is coupled into the waveguide using L_2. The second harmonic is coupled out using L_3. The second harmonic is measured by using a Si photo-diode.
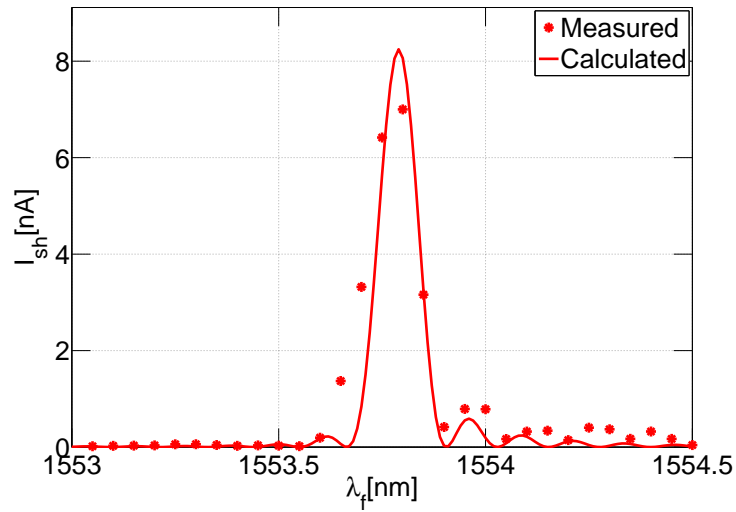
Figure 4.4: The measured and calculated SH phase matching characteristic obtained by tuning λ_f. The FWHM is $\approx 100\,\mathrm{pm}$. The asymmetry in the curve is explained by the inhomogeneity of the waveguide. The length of the sample is $66\,\mathrm{mm}$ and the temperature is kept at $40\,^\circ\mathrm{C}$.

The responsivity of the Si detector used is $R \approx 0.5 \frac{A}{W}$. Hence the peak SH power is $P_{SH} = \frac{I_{SH}}{R}$, where I_{SH} is the photo-diode current. The measured SH efficiency η_{SH} is calculated as follows:

$$\eta_{SH} = \frac{\frac{I_{SH}}{R} \times 100}{P_f^2} \tag{4.1}$$

$$= \frac{\frac{8 \text{ nA}}{0.5 \frac{A}{W}} \times 100}{(\ 0.8 \text{ mW} \ )^2} \tag{4.2}$$

$$\eta_{SH} = 2.5 \ \frac{\%}{W} \tag{4.3}$$

The measured efficiency falls short of the predicted efficiency of $13 \ \frac{\%}{W}$. While plotting the Fig. 4.4, a coupled fundamental power of $P_f = 0.35 \text{ mW}$ is used so that the two peaks coincide. Also the calculated λ_f for exact phase matching is offset from the measured value by 4 nm. The FWHM of the measured phase matching curve ($\approx 100 \text{ pm}$) agrees very well with the calculated value.

There is an asymmetry in the measured phase matching curve. The right side lobe is higher compared to the left side lobe. As explained in Chapter 1, the SH corresponding to the first side lobe gains energy during the initial one third and the final one third section of the waveguide. An inhomogeneity in these sections may result in a faster or slower growth, depending on the coherence length of interaction. A decrease in the width of the waveguide for example, will result in an increase in the coherence length of interaction for the right side lobe while decreasing the coherence length for the left side lobe. The calculated curve in Fig. 4.4 is obtained by assuming an inhomogeneity of the width of the waveguide. This is shown in more detail in Fig. 4.5(a). The width of the waveguide is assumed to be decreasing from $5.0 \ \mu m$ to $4.5 \ \mu m$ over a distance of 20 mm. With this, the propagation constants $\beta_{TE,TM,SH}$ change as shown in the Fig. 4.5(b). At the exact phase matching wavelength, the value of $\Delta\beta$ changes from 0 in the central section to $-160 \ \frac{1}{mm}$ at the end of the waveguide. Neither temperature inhomogeneity nor the variation in the refractive index (which are other possible reasons for asymmetry) along the depth is considered.

The temperature tuning characteristics of SH is studied. With increasing temperature, the phase matching curve shifts to shorter wavelengths(Fig. 4.6). The slope of the tuning curve is $\partial_T \lambda_f = -200 \ \frac{pm}{^\circ C}$. The slope is roughly the same for all domain periods. It is also evident from the figure that the shift of the phase matching curve with domain period has a slope $\partial_\Lambda \lambda_f = 0.1$. There is a certain offset between the calculated and measured values. This is because the model for the effective index calculation for Ti:LN waveguide is not exact.

Spontaneous Parametric Down Conversion

The Spontaneous Parametric Down Conversion process in the waveguide is investigated. The set up used for the mesurement is shown in Fig. 4.7. The ECL

(a)   (b)
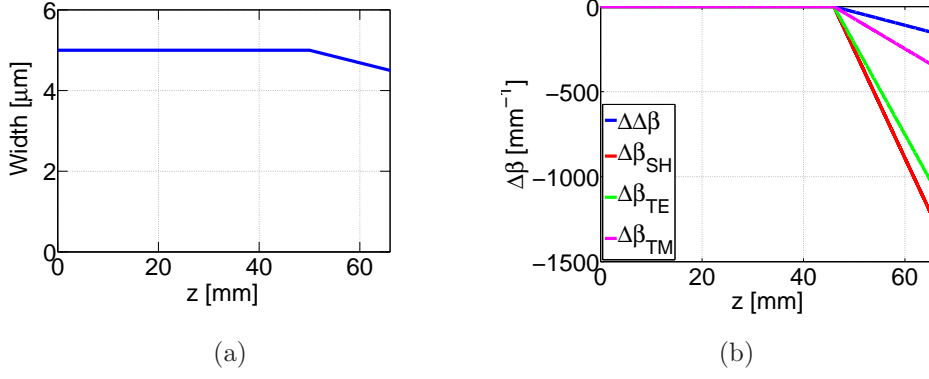
Figure 4.5: (a) Inhomogeneity in the width of the waveguide as used in the calculation. (b) The change of the propagation constants as a function of the interaction length.
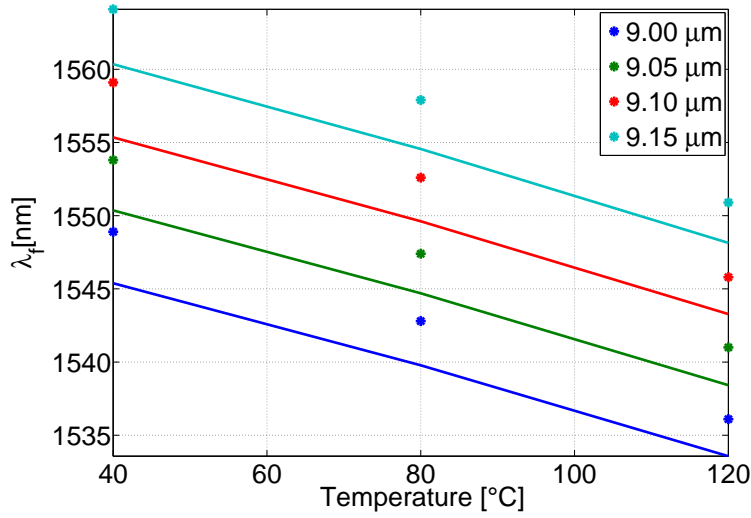
Figure 4.6: The measured and calculated temperature tuning behavior of SH. The slope of the curve is $\partial_T \lambda_f = -200 \, \frac{\text{pm}}{^\circ\text{C}}$. The slope is roughly the same for all the domain periods.

(Toptica DL pro 100, $\lambda_p \approx 775$ nm) is used as the pump source. The light from the laser-head is coupled out using a polarization maintaining fiber. The fiber tip is oriented in such a way that TE polarized light is coupled into the waveguide. The in-coupling lens is L_3 is anti-reflection coated for 775 nm. The down-converted radiation in the 1550 nm range is coupled out using the lens L_4. L_4 is anti-reflection coated for 1550 nm. The radiation is then spectrally resolved by a monochromator (HR320). The power in the down-converted field is at least 10 orders lower than that of the pump field. It is necessary to use a detection system with high sensitivity. The sensitivity is achieved by using a Lock In amplifier (SR850) to measure the current from the InGaAs photo-diode. The reference signal for the amplifier is obtained from a chopper, which modulates the pump. A 3 s time constant is used for the measurement. The input impedance is set to (100 MΩ).
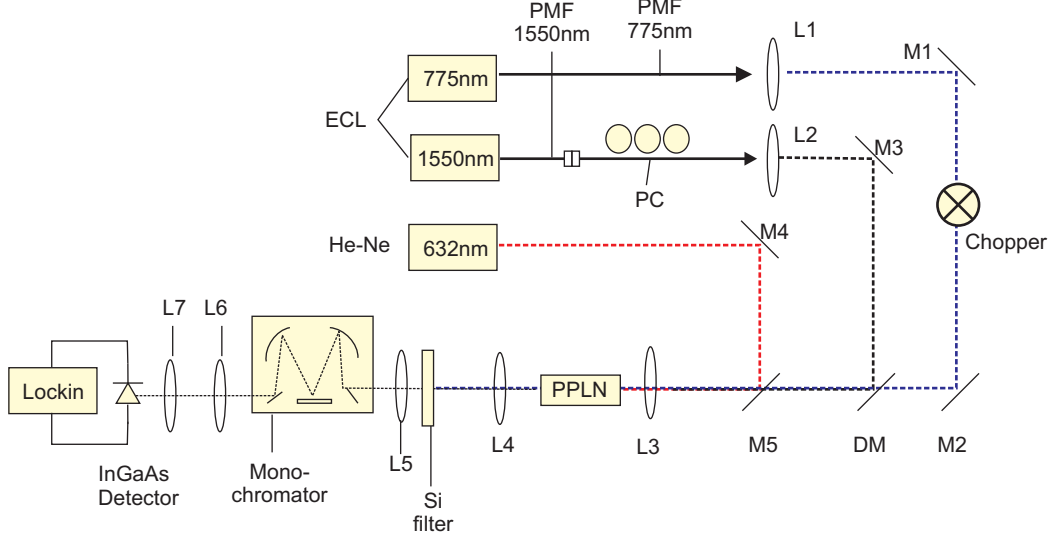
Figure 4.7: The setup used to measure spontaneous parametric down conversion. Light from ECL ($\lambda_p \approx 775$ nm) is used as the pump. The power is measured by using an InGaAs photo-diode. A monochromator is used for spectral resolution. The Lock In technique provides the required detection sensitivity.

With this setting, the spectral current density of thermal noise is given by

$$
\begin{aligned}
\tilde{I}_{rms} &= \sqrt{\frac{4\,k\,T}{Z_{in}}} \\
&= \sqrt{\frac{4 \times 1.38 \times 10^{-23}[\frac{J}{K}] \times 300\,[K]}{100 \times 10^6 [\Omega]}} \\
&= 130\,\frac{fA}{\sqrt{Hz}}
\end{aligned}
$$

The choice of time constant is carefully made to reduce the noise on one hand, without increasing the mesurement duration. With a 3 s time constant, the lockin acts as a bandpass filter with a bandwidth of $\Delta f = 26$ mHz centered at the reference frequency. The noise level in this case is $I_{rms} = \tilde{I}_{rms} \times \Delta f = 2$ fA. For a more detailed discussion about the noise contributions from other sources please refer the technical literature of SR850 [46].

The monochromator (HR320), with a Czerny-Turner design, is used for spectrally resolving the intensity of down converted field. The arrangement of the mirrors, grating and the slits is shown in Fig. 4.8. Before measuring the SPDC spectrum, the transmission of the 1550 nm radiation through the monochromator is studied. The monochromator has a blazed diffraction grating which concentrates the diffracted power to the first order. The grating is blazed for operation at a wavelength range $\lambda \approx 1\,\mu m$ [47]. The diffraction efficiency is reduced in the 1550 nm range. The transmission of TE polarized radiation is 25 % while that of TM is 20 % at 1550 nm, because the angle of first order diffraction and the angle of specular reflection are not equal. In order to obtain the best possible resolution, it is necessary to illuminate the diffraction grating completely. This is done by
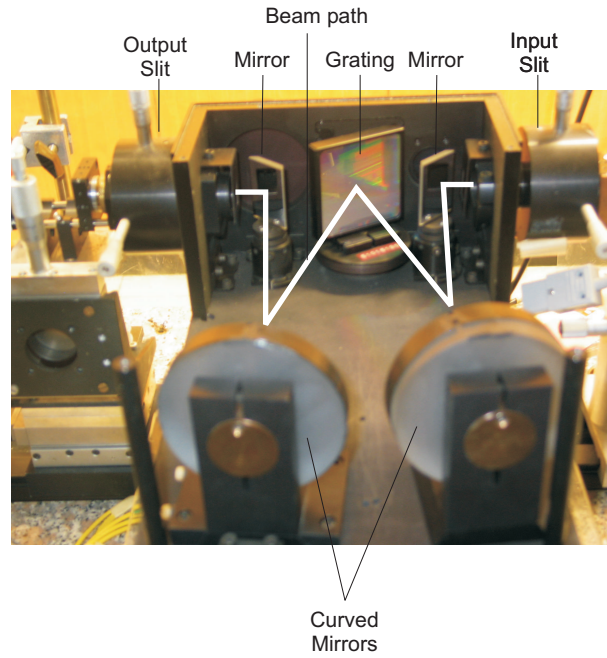
Figure 4.8: HR320 Monochromator with Czerny-Turner design. The monochromator has a blazed grating at $1\,\mu$m. The grating is $68\,\text{mm} \times 68\,\text{mm}$ with 600 lines per mm. The focal length of the curved mirrors used for shaping the wavefront is $32\,\text{cm}$. The optical path is shown by thick white lines.

carefully choosing the illumination optics. The details concerning the optics are shown in Fig. 4.9.
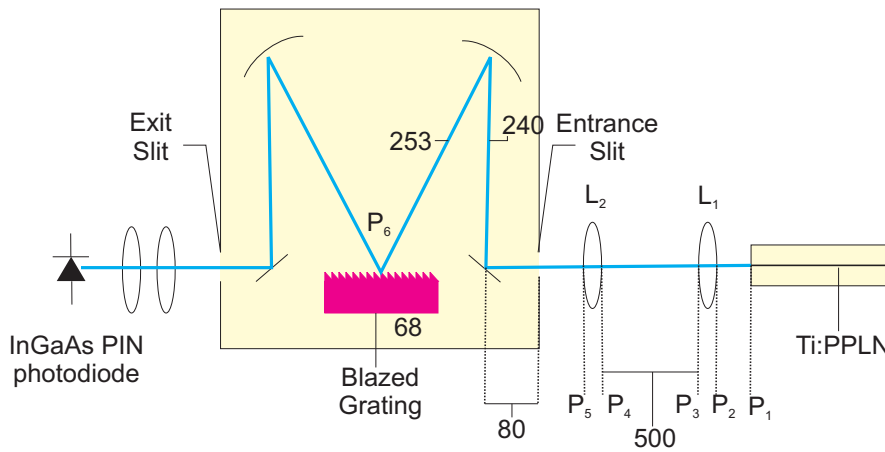
Figure 4.9: Schematic diagram of the monochromator along with the illumination and collection optics. The optics in front of the input slit is designed to illuminate the grating completely. The optics behind the slit focuses all the light from the output slit on the InGaAs PIN diode. The optical path lengths are shown in the green boxes in mm.

The lens L_1 ($f = 10$mm) is used to collect the light transmitted through the waveguide. The lens L_2 focuses the collimated beam on the input slit of the monochromator. The beam expands behind the input slit. The mirror M_1 re-

shapes the wavefront of the expanded beam so that a plane wavefront hits the grating. We assume the intensity distribution at the waveguide end face is the waist of an imaginary Gaussian beam. We track the evolution of the Gaussian beam from the point P_1 to P_6, using the well known ABCD matrix method [48]. The focal length of the lens L_2 is chosen in such a way that the beam waist at P_6 is half the size of the grating ($68\,\mathrm{mm} \times 68\,\mathrm{mm}$). The results are summarized in Fig. 4.10(a) and Fig. 4.10(b). The resolution is improved by reducing the width of the output slit of the monochromator. Even though the lens with $20\,\mathrm{mm}$ focal length almost fully illuminates the grating ($\approx 60\,\mathrm{mm}$) compared to the one with $30\,\mathrm{mm}$ focal length ($\approx 40\,\mathrm{mm}$), the improvement in resolution is not seen during the measurement. This points to the fact that the resolution is limited by the optics inside the monochromator. The imperfection of the spherical mirror may result in a non-planar wavefront incident on the grating. This results in a spread of the angle corresponding to the first order diffraction. In this case, the spot formed on the output slit, after focusing by the second spherical mirror is broader than the one at the input slit. It is seen that to obtain a resolution better than $0.5\,\mathrm{nm}$, transmission through the monochromator has to be compromised.

(a)   (b)
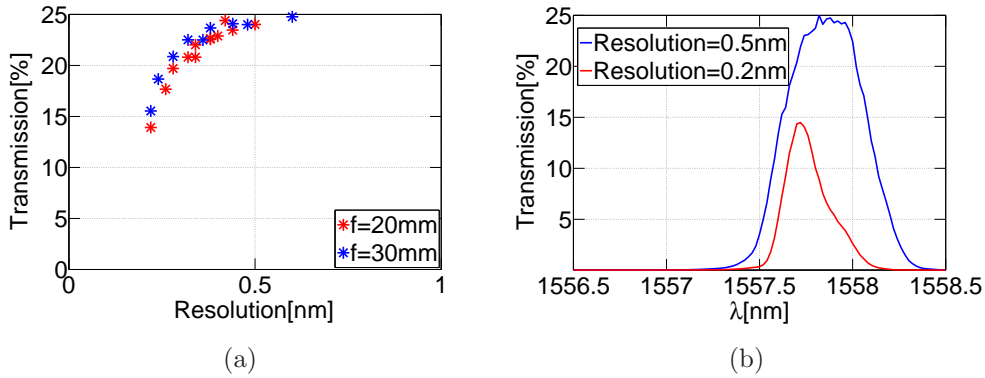
Figure 4.10: (a)Transmission through the monochromator for TE polarized field at $1557.75\,\mathrm{nm}$. The maximum transmission is limited to $25\,\%$ and is limited by the finite reflectivities of the mirrors and lens as well as by the decrease in diffraction efficiency. The transmission has to be compromised to obtain a resolution better than $0.5\,\mathrm{nm}$. (b) The spectra of the ECL at $1557.75\,\mathrm{nm}$ as measured by the monochromator for two different values of resolution.

An example of measured spectrum is shown in Fig. 4.11. The TM emission is consistently lower than the TE emission. This is attributed to the higher TM-propagation loss in the waveguide and to the polarization dependent loss of the monochromator. The measurement is done at high temperature to reduce the photo-refractive damage. The conversion efficiency for the measurement with $\lambda_p \approx 775\,\mathrm{nm}$ is calculated from the measured photo-diode current(I) as shown in Eq. 4.4. The smaller conversion efficiency seen in the measurement with $\lambda_p \approx 771\,\mathrm{nm}$ is because of reduced pump coupling.
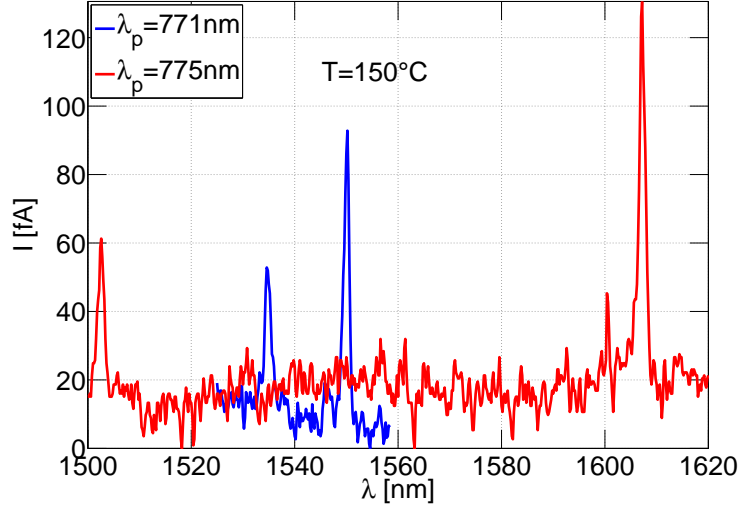
Figure 4.11: The measured spectra of SPDC at $T = 150\,^\circ\text{C}$. The peak with higher amplitude corresponds to TE polarized field. The TE field is higher because of smaller loss in the waveguide and better transmission through the monochromator.

$$
\begin{aligned}
\eta_{\text{TE}}[\%] &\equiv \frac{P_{\text{TE}}}{P_{\text{p,coupled}}} \times 100 \\
P_{\text{TE}} &= \frac{I \times T_{\text{TE}}}{R} \\
&= \frac{150\,[\text{fA}] \times 4}{0.55\,[\frac{\text{A}}{\text{W}}]} \\
&\approx 1.5\,\text{pW.} \\
\Rightarrow \eta_{\text{TE}} &= \frac{1.5\,\text{pW} \times 100}{5\,\text{mW}} \\
&= 3 \times 10^{-8}\,\%
\end{aligned}
\qquad
\begin{aligned}
\eta_{\text{TM}}[\%] &\equiv \frac{P_{\text{TM}}}{P_{\text{p,coupled}}} \times 100 \\
P_{\text{TM}} &= \frac{I \times T_{\text{TM}}}{R} \\
&= \frac{80\,[\text{fA}] \times 5}{0.55\,[\frac{\text{A}}{\text{W}}]} \\
&\approx 1.0\,\text{pW.} \\
\Rightarrow \eta_{\text{TM}} &= \frac{1.0\,\text{pW} \times 100}{5\,\text{mW}} \\
&= 2 \times 10^{-8}\,\%
\end{aligned}
$$

Further measurements of SPDC are done at low temperature $(< 50\,^\circ\text{C})$. This is essential because, the fiber pigtailing process requires low temperature operation of the waveguide. The calculated and measured tuning characteristics of SPDC is shown in Fig. 4.12(a). The slope of TE field is $\partial_{\lambda_\text{p}} \lambda_{\text{TE}} = 10$ and the TM field is $\partial_{\lambda_\text{p}} \lambda_{\text{TM}} = -5$. The change in the wavelengths of down-conversion as a result of changing the domain period is shown in Fig. 4.12(b). The TM wavelength changes with a slope of $\partial_\Lambda \lambda_{\text{TM}} = 0.42$ and the TE wavelength changes with a slope of $\partial_\Lambda \lambda_{\text{TE}} = -0.42$

4.3 Polarization Beam Splitter

As mentioned already a Polarization Beam Splitter (PBS) is integrated behind some of the waveguides in the sample. The poling is restricted to a region of 66 mm outside the PBS. The PBS is designed as a special 2×2 coupler. Both the TE and
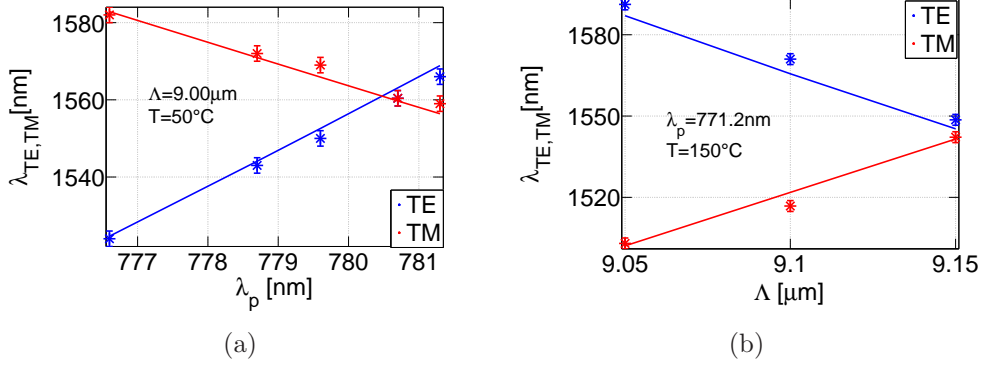
Figure 4.12: (a) The pump wavelength characteristic of SPDC. The slope of TE field is $\partial_{\lambda_p}\lambda_{\mathrm{TE}} = 10$ and the TM field is $\partial_{\lambda_p}\lambda_{\mathrm{TM}} = -5$. (b) The change in the down conversion wavelength with domain periods.

TM fields which enter the coupling region, excite corresponding symmetric and anti-symmetric normal modes. These modes have different propagation constants. The length of the coupling region is chosen in such a way that, for TE (TM) modes we get constructive (destructive) interference in the cross port and for TM (TE) modes we get constructive (destructive) interference in the parallel port. The schematic of the PBS is shown in Fig. 4.13.
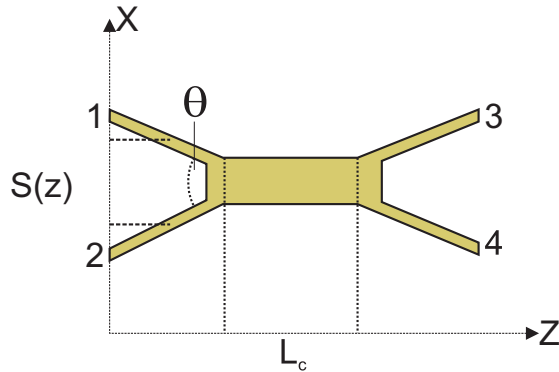
Figure 4.13: Schematic of the polarization splitter. S(z) is the separation between the transition region. The opening angle, θ and the length of the central section, L_c are the design parameters.

The fields coupled into the PBS enter the central section after traversing a transition region where there is longitudinal variation in the effective index. Because of the longitudinal variation in the refractive index, the transition region as a whole does not have normal modes with well defined propagation constants. However, it is possible to define local normal modes for an infinitesimal section of the transition region. The properties of completeness and orthogonality are satisfied by the local normal modes in this infinitesimal section. As a consequence, any field distribution in the transition region is written as a superposition of the

38

local normal modes as shown below.

$$E(x,y,z) = \sum_i c_i(z) \, \psi_i(x,y,z) \, e^{-i\theta_i(z)}$$

$$\theta_i(z) = \int_0^z dz' \, \beta_i(z')$$

In the above equations, ψ_i represents the distribution of local normal modes, and β_i represents the propagation constant of the local normal mode at the location z along the transition region. Note that the longitudinal dependence of the transverse mode profile and the propagation constants are the characteristics of the local normal modes. The evolution equation of the amplitude coefficient, c_i, is obtained after substituting the local normal mode decomposition of the field distribution into the Maxwell's eqations.

$$\partial_z c_i = \sum_{i \neq j} M_{ij} \, c_j \, e^{i[\theta_i - \theta_j]} \qquad \text{where}$$

$$M_{ij} = \frac{k_0}{4Z_0 P[\beta_i - \beta_j]} \int dxdy \, \psi_i^* \, \partial_z n^2 \, \psi_j$$

The matrix M has non-zero non-diagonal elements, which means that the amplitude coefficients change because of coupling between the local normal modes. The coupling is mediated by the longitudinal variation of the refractive index $(\partial_z n^2)$. However, for sufficiently smooth variations, the coupling constant is negligible. In other words, the power exchanged between the local normal modes is neglected. In the case of PBS, the longitudinal variation of the refractive index is slow enough. The waveguide transition in this case is said to be adiabatic. We are concerned only with the first two local normal modes, the symmetric $(\psi_s(x,y,z), \beta_s(z))$ and the anti-symmetric $(\psi_a(x,y,z), \beta_a(z))$. Thus the total field is written as

$$E(x,y,z) = c_s(z) \, \psi_s(x,y,z) \, e^{-i\theta_s(z)} + c_a(z) \, \psi_a(x,y,z) \, e^{-i\theta_a(z)}$$

The field distributions that are localized in the branches are obtained by adding and subtracting the two local normal modes.

$$\psi_1 = \frac{1}{\sqrt{2}} \, [\, \psi_s + \psi_a \,]$$

$$\psi_2 = \frac{1}{\sqrt{2}} \, [\, \psi_s - \psi_a \,]$$

The total electric field in terms of the localised distributions is rewritten as

$$E(x,y,z) = \frac{1}{\sqrt{2}} \, [\, c_1(z) \, \psi_1(x,y,z) + c_2(z) \, \psi_2(x,y,z) \,] \qquad \text{where}$$

$$c_1(z) \equiv \frac{1}{\sqrt{2}} \, [\, c_s(z) \, e^{-i\theta_s(z)} + c_a(z) \, e^{-i\theta_a(z)} \,] \qquad \text{and}$$

$$c_2(z) \equiv \frac{1}{\sqrt{2}} \, [\, c_s(z) \, e^{-i\theta_s(z)} - c_a(z) \, e^{-i\theta_a(z)} \,]$$

The field amplitudes and transverse distributions are normalised as follows:

$$[c_{a,s,1,2}] = 1$$
$$[\psi_{a,s,1,2}] = \frac{V}{m}$$

In order to solve the amplitude evolution equations, consider a linearly polarized (TE or TM) field with power P_0 that is coupled into the input port 1. The input field excites the symmetric and anti-symmetric normal modes with equal power. The initial conditions of the equations under this condition are,

$$c_1(0) = \sqrt{\frac{P_1(0)}{P_0}} = \frac{1}{\sqrt{2}}$$

$$c_2(0) = \sqrt{\frac{P_2(0)}{P_0}} = \frac{1}{\sqrt{2}}$$

The closed form solutions are

$$P_1(z) = P_1(0) \cos^2\left[\frac{\Delta\theta(z)}{2}\right]$$

$$P_2(z) = P_2(0) \sin^2\left[\frac{\Delta\theta(z)}{2}\right]$$

The term $\Delta\theta(z)$ represents the phase difference accumulated between the symmetric and anti-symmetric normal modes, both in the transition regions and the straight section. In other words, $\Delta\theta(L) = \Delta\beta \, L_c + 2\Delta\theta$. The first term includes the contribution from the difference in the propagation constants ($\Delta\beta$) in the central section of the coupler. The second term ($\Delta\theta$) includes the contribution from the two transition regions. It is evident that the output power is localised in either branch if $\Delta\theta = m\pi$. The bar state is when the output power is localised in the port 3. The cross state is when the output power is localised in the port 4. The structure will act as a PBS if for a particular value of the length of the central region (L_c) and the opening angle (θ_0), we end up with a phase difference of an even multiple of π for one polarization and an odd multiple of π for the orthogonal polarization.

$$\Delta\theta(L) = \Delta\beta L_c + 2\Delta\theta$$
$$= \Delta\beta L_c + \cot\left(\frac{\theta_0}{2}\right) \int_{S_{min}}^{S_{max}} \Delta\beta(s) \, dS$$
$$= \begin{cases} n\pi & QTE \\ m\pi & QTM \end{cases}$$

We solve for the two design parameters (L_c and θ_0) for various possible combinations of m and n. The local normal mode analysis by means of the finite element method (FEM) yields the difference of the phase constants as a function of the waveguide separation. Details regarding the numerical aspects of the simulation

can be found in [23] and [49]. The closed form solutions for L_c and θ_0 are shown below.

$$L_c = \pi \frac{m\,A_{\mathrm{TE}} - n\,A_{\mathrm{TM}}}{\Delta\beta_{\mathrm{TM}}\,A_{\mathrm{TE}} - \Delta\beta_{\mathrm{TE}}\,A_{\mathrm{TM}}}$$

$$\theta_0 = \frac{2}{\pi}\,\tan^{-1}\left[\frac{\Delta\beta_{\mathrm{TM}}\,A_{\mathrm{TE}} - \Delta\beta_{\mathrm{TE}}\,A_{\mathrm{TM}}}{n\,\Delta\beta_{\mathrm{TM}} - m\,\Delta\beta_{\mathrm{TE}}}\right]$$

n	m	L_c [μm]	θ_0 [°]	L_{total} [μm]
2	*3*	*563*	*0.599*	*6869*
3	4	311	0.283	13648
4	5	58	0.185	20428
4	7	2197	0.779	7047
5	8	1944	0.318	13827
6	9	1691	0.199	20607
6	11	3830	1.113	7225
7	10	1439	0.146	27387
7	12	3577	0.363	14005

parameter	value
width	7 μm
thickness	90 nm
diffusion time	9 hours
diffusion temperature	1060 K

Table 4.1: The opening angle θ and the central section length L_c, as a function of the interference order. The parameters corresponding to $n = 2$ and $m = 3$ are chosen for fabrication of the polarization splitter. The fabrication parameters of the waveguides are also shown.
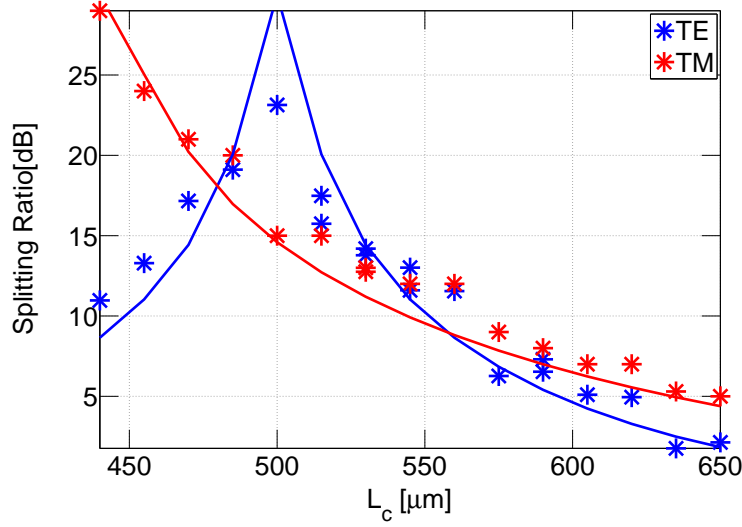
Figure 4.14: Splitting ratio of TE and TM polarizations as a function of the coupling length, L_c. The measured results are shown by (*) and the a $\sin^2$ fit by lines.

The set up used to characterize the PBS is the same as in Fig. 4.7. For the measurement we use only the DFB laser ($\lambda = 1550$ nm). We adjust the TE or TM polarization using the fiber polarization controller. To measure the splitting ratio in TE polarization, we launch TE polarized light into port 1 through the waveguide and monitor the power at ports 3 and 4. The splitting ratio in this case

is $\gamma_{\text{TE}} = \frac{P_4}{P_3 + P_4}$. Similarly, the splitting ratio of TM is measured after launching TM polarized light into port 1 and monitoring the power at ports 3 and 4. The splitting ratio for TM polarization is defined as $\gamma_{\text{TM}} = \frac{P_3}{P_3 + P_4}$. In the best case, a splitting ratio of $\gamma_{\text{TM}} = 30\,\text{dB}$ and $\gamma_{\text{TE}} = 24\,\text{dB}$ is measured. The optimum L_c for the best splitting is different for TE and TM modes because of dispersion. The splitting ratio decreases rapidly on either side of the peak. Since the photo-mask was designed with only a few values of L_c, the peak measured for the TE polarization may not correspond to the actual peak. However, a structure with a splitting ratio of 20 dB for both polarizations ($L_c = 485\,\mu\text{m}$) is chosen for further experiments. A splitting ratio of 20 dB is sufficient for the single photon experiments. This is because the spurious events contributed by the finite splitting is much smaller than the dark counts in the single photon detectors.

4.4 Pigtailing and Packaging

As mentioned already, fiber pigtailing of the sample helps to obtain a more robust and stable operation of the photon pair source. Also, the light exiting the fiber has a symmetric Gaussian profile unlike in a waveguide, which helps to avoid beam shaping optics in some applications. The packaging of the pigtailed sample helps in easier handling. In this section, the different steps in the pigtailing of the input and output fibers and the packaging are explained in detail.

After the characterization of the sample by measuring scattering loss, non-linear efficiency and splitting ratio of the PBS, a specific structure is chosen for pigtailing. As a first step, the endfaces of the sample are angle polished to avoid back-reflection. In order to couple the pump power into the waveguide, a polarization maintaining fiber (PMF) at 775 nm is used. The commercially available PMF is angle polished at $8°$. Hence the sample endface through which the pump power is coupled (endface [A]) is polished at an angle determined by the Snell's law of refraction.

$$n \times \sin\theta_i = n_{\text{eff,TE}}[\lambda_p = 775\,\text{nm}] \times \sin\theta_r$$
$$1.5 \times \sin 8° = 2.26 \times \sin\theta_r$$
$$\Rightarrow \theta_r = 5.3°$$

The endface [B] from which the down-converted photons are coupled out is also angle polished. The optimum polishing angle is different for the TE and TM photons. The Snell's law suggests $5.4°$ for TE and $5.6°$ for TM. As a compromise, the sample is polished at an angle of $5.5°$.

The photon pair source requires supressing the residual pump, which would otherwise find its way into the single photon detectors. A dielectric mirror is deposited on the endface B to reflect the residual pump. The mirror consists of 12 alternating layers of TiO_2 and SiO_2. The thickness of each layer is optimised by a Monte-Carlo simulation. The criteria for optimization are high transmission for the down-converted photons and high reflectivity for the pump photons. A pump suppression of $\approx 98\,\%$ is achieved, whereas the transmission losses for signal

and idler photons is kept very small ($\approx 4\,\%$). The calculated and measured mirror transmission characteristics are shown in Fig. 4.15. The measurement is done with a reference mirror having the same fabrication parameters as the mirror on the endface B. The thickness of the different layers used is shown on the left hand side. There is a good agreement between the calculated and measured reflectivity spectra. The reflectivity of $< 4\,\%$, extends over a 150 nm range at 1550 nm which allows tuning of the wavelengths of down converted photons.

Material	Thickness [nm]
SiO_2	409
TiO_2	394
SiO_2	123
TiO_2	86
SiO_2	381
TiO_2	418
SiO_2	138
TiO_2	76
SiO_2	395
TiO_2	79
SiO_2	129
TiO_2	83
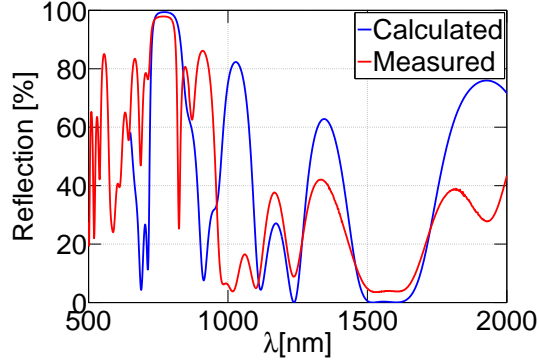
Figure 4.15: The thickness of the different layers in the dielectric mirror. The calculated and measured mirror reflectivities are shown on the right hand side. The reflectivity at the pump wavelength is 98 %. The reflectivity at 1550 nm is 4%.

The pigtail used to couple the down-converted photons out from the endface B is a standard single mode fiber at 1550 nm. Since the TM photons arrive at port 3 and the TE photons arrive at port 4 behind the PBS, two different fibers are used for out-coupling. The two fibers are embedded in a single glass ferrule. As a first step in the alignment, light from an unpolarised broad band source is coupled in from the endface A and the transmission through port 3 and port 4 is monitored by a an InGaAs photodiode (ETX200T5). Amplified spontaneous emission from an Erbium doped fiber pumped at 980 nm is used as the broadband source. The light is coupled out using a lens which is anti-reflection coated. The purpose of this measurement is to obtain a reference for transmission through the pigtails at endface B. The next step is to replace the outcoupling lens by the glass ferrule. This is shown schematically in Fig. 4.16(a).

The pigtailing setup is shown in Fig. 4.17. In order to align the fiber tips properly, a single optical stage with provisions for motion along three translation axes, and three rotation axes is used. The accuracy of motion along the three translation axes is about ≈ 30 nm achieved by using three picomotor stages. The glass ferrule with the fiber tips is held in place by a vacuum tip (Fig. 4.16(b)). The flat on the ferrule also helps to position the ferrule on the holder. Also a pre-alignment of the roll of the tip is achieved with the flat. The roll is further aligned by obtaining equal transmission through the two ports behind the PBS. The transmission through the two fibers is monitored by using fiber pigtailed

Figure 4.16: (a)Schematic of the glass ferrule showing the polishing angles of the sample and ferrule. (b) Front view and the side view illustrating the ferrule holder and the vacuum tip.

Figure 4.17: Schematic of the pigtailing setup. An amplfied spontaneous emission (ASE) based source is used to align the glass ferrule. ASE source has equal outputs in both polarizations. The criterion for alignment is maximum transmission through both single mode fibers behind the polarization splitter. The transmission is monitored by two fiber pigtailed InGaAs photo-diodes.

InGaAs detectors (FID13S51JT). In addition to the roll, the yaw of the fiber tips relative to the waveguide has to be precisely aligned. One way to pre-align the yaw of the fiber tips is to launch red light through the two connectors and make sure that the reflected spots from both waveguides coincide with the spot seen on the fiber tips.The roll and yaw alignments are schematically sketched in Fig. 4.18

The alignment of the pitch is more difficult compared to the roll and yaw. The only way to coarsely align the pitch is before placing the sample. This is done be ensuring that the red laser beam remains parallel to the rail on the optical bench. After the three lateral axes and the three rotation axes are coarsely aligned, the fine alignment is done. The metric for fine alignment is to achieve maximum transmission through both the ports of the PBS. A transmission (relative to the reference) of roughly $\approx$ -2 dB is achieved through the TE port and $\approx$ -3 dB through the TM port. The transmission is limited mainly by the mode mismatch between the fiber and waveguide modes, and by the imprecise alignment of the three ro-

44

Figure 4.18: (a) The mis-alignment in the roll of the glass ferrule. The roll mis-alignment is not crucial in the case of pigtailing only one fiber. (b) The yaw of the ferrule is pre-aligned with the red laser.

tation stages.

After the fine alignment procedure, the two fibers are glued to the endface B. For this, the fiber tip is pulled back about 5 mm from the endface B. A single drop of UV curable glue is applied on the ferrule endface. The fiber tip is pushed back into position. During this step, fine alignment is required to bring the transmission through the two fibers back to the original value. Once the transmission is re-established, the glue is cured by illumination with a UV gun ($\lambda = 365$ nm). The UV gun helps to direct the UV radiation from the top and the sides onto the glue. The glue cures after illumination for approximately 3 minutes. The next step is to release the vacuum tip and illuminate the glue from bottom. It is necessary that the UV curing of the glue is done uniformly over the whole drop. Non-uniform curing will result in a degradation of the coupling because of the inhomogeneous mechanical stress. This is verified by monitoring the transmission during the UV illumination.
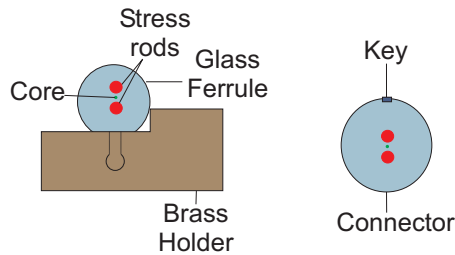
Figure 4.19: Schematic of the glass ferrule holding the polarization maintaing fiber tip. The glass ferrule is polished with the slow axis parallel to the ferrule holder. The flat helps in the pre-alignment of yaw. The orientation of the slow axes with respect to the key of the fiber connector is shown on the right hand side.

Once the endface [B] is pigtailed, the setup (Fig 4.17) is changed to facilitate the pigtailing of the endface A. Unlike the endface B, a PMF is used for pigtailing at the endface [A]. For Type II SPDC, it is necessary that the pump radiation launched into the waveguide is TE polarized. To ensure this, the fiber tip of

the PMF is embedded in a ferrule with a polished surface as shown in Fig. 4.19. The polished surface of the ferrule is perpendicular to the line connecting the stress rods of the PMF. The perpendicular direction was chosen becasue the fiber connector on the other side has a key which is on the line connecting the two stress rods. In this way we make sure that if a TE polarized pump is launched into the PMF, a TE polarized field is coupled into the waveguide.
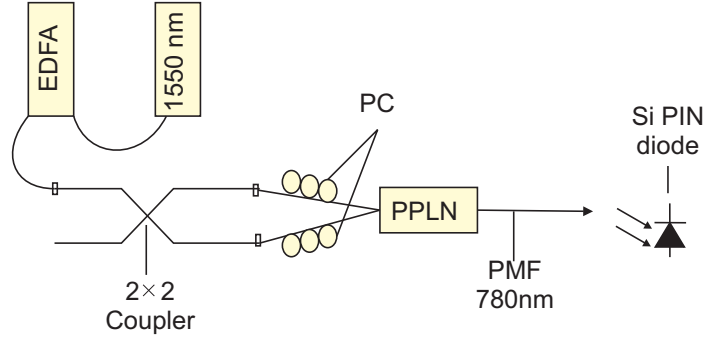
Figure 4.20: Schematic of the set-up to pigtail the polarization maintaining fiber. The criterion for alignment is the maximum transmission of the second harmonic generated in the sample through the fiber. The power is monitored using a Si photo-diode.

As a first step, SH efficiency is measured by coupling in the fundamental radiation through the pigtails. The SH generated in the waveguide is coupled out from the endface A using a lens which is anti-reflection coated for 775 nm, and monitored using a Si PIN photo diode. The SH power measured is the criterion used later to align the fiber to be pigtailed on the endface A. The setup used to monitor the SH and to glue the pigtail on the endface A is shown in Fig. 4.20. The light from an ECL ($\lambda_\mathrm{f} = 1550\,\mathrm{nm}$) is used as the fundamental wave. The fundamental is amplified by an Erbium Doped Fiber Amplifier. The amplified fundamental is split into two beams by using a 2×2 coupler. The fiber polarization controllers in the output arms of the coupler are used to adjust the polarization. TE polarized light is launched into the cross-port and TM polarized light is launched into the parallel port. The SH generated is coupled out using the PMF to be pigtailed on the endface A. The alignment procedures for the PMF are similar to the steps for pigtailing at endface B. The SH power measured after pigtailing the endface A is shown in Fig. 4.21. A Si PIN photo-diode (BPW34) is used for the measurement. The peak fiber-to-fiber SHG efficiency is calculated as follows.

$$
\eta_\mathrm{SH} \equiv \frac{\mathrm{P_{SH}} \times 100}{\mathrm{P_{TE}} \times \mathrm{P_{TM}}} [\frac{\%}{\mathrm{W}}]
$$

$$
\mathrm{P_{SH}} = \frac{\mathrm{I}}{\mathrm{R}} = \frac{0.4\,[\mu\mathrm{A}]}{0.5\,[\frac{\mathrm{A}}{\mathrm{W}}]} = 0.8\,\mu\mathrm{W}.
$$

$$
\mathrm{P_{TE}} = \mathrm{P_{TM}} = 8\,\mathrm{mW}
$$

$$
\eta_\mathrm{SH} = \frac{0.8\,\mu\mathrm{W} \times 100}{8\,\mathrm{mW} \times 8\,\mathrm{mW}} = 2\,\frac{\%}{\mathrm{W}}
$$
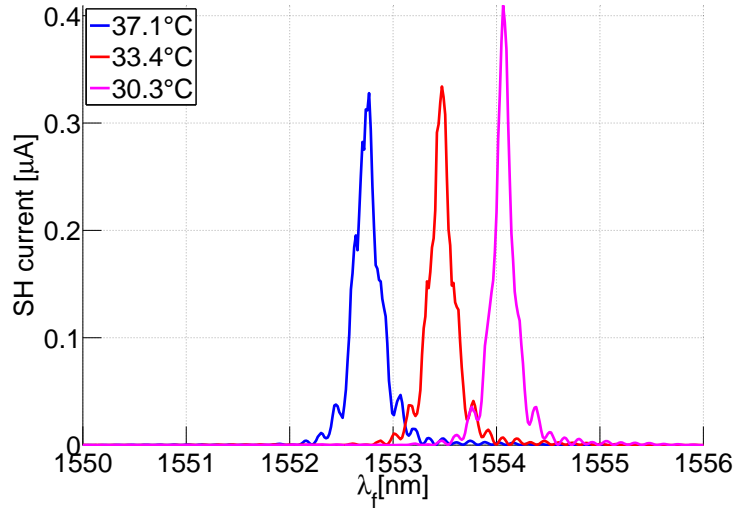
Figure 4.21: Measured phase matching characteristics of second harmonic after pigtailing. The measurements are done at three different temperatures.

The SH efficiency is $\eta_{\text{SH}} \approx 2\,\frac{\%}{W}$. The measured tuning characteristic has a FWHM of 150 pm which agrees well with modelling result. The slope of temperature tuning of the SH is $\approx -190\,\frac{pm}{\circ C}$.

After pigtailing both endfaces, the sample is placed in a specially designed package. Before this, the pigtails coming out of the ferrules are fixed on an invar block. This is necessary to prevent any mechanical stresses on the cured glue. Invar is chosen because its thermal expansion coefficient is similar to that of an optical fiber. The fiber is fixed on the invar block by using a two component epoxy adhesive (ECCOBOND 286). The adhesive after mixing curess within 10 hours. The procedure is shown in Fig 4.22. The invar block is fixed on the Cu
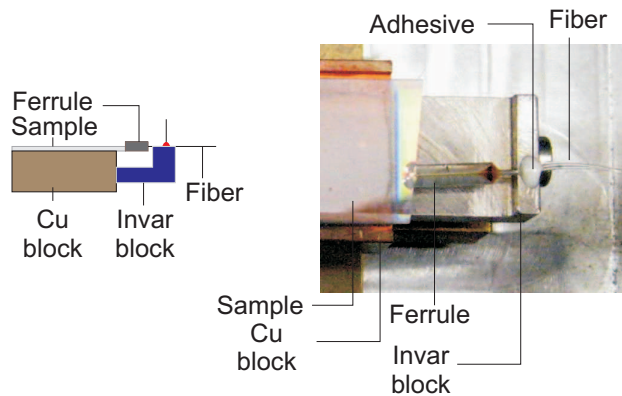
Figure 4.22: The pigtailed fiber is fixed on an Invar block. This helps to prevent any mechanical stress on the pigtail.

block holding the sample. Cu is chosen as the sample holder because the thermal coefficient of expansion of Cu is similar to that of LN. The temperature of the sample is stabilized by using three peltier elements and a negative temperature coefficient thermistor. The leads of the peltier elements and the NTC thermistor

47

are accessible outside the Al housing through a D-sub connector. The packaging is shown in Fig. 4.23.

Figure 4.23: Photograph of the packaged and pigtailed device.

The pigtailed and packaged sample is further characterized by SPDC experiment. The light from an ECL at $(\lambda_p = 780\,\mathrm{nm})$ is coupled into the waveguide. The spectrum of the SPDC is analyzed by using a monochromator (HR 320). The setup used for the measurement is shown in Fig. 4.24. The setup is similar to the one used for measurement before pigtailing. The measured TE polarized SPDC spectrum is shown in Fig. 4.25.
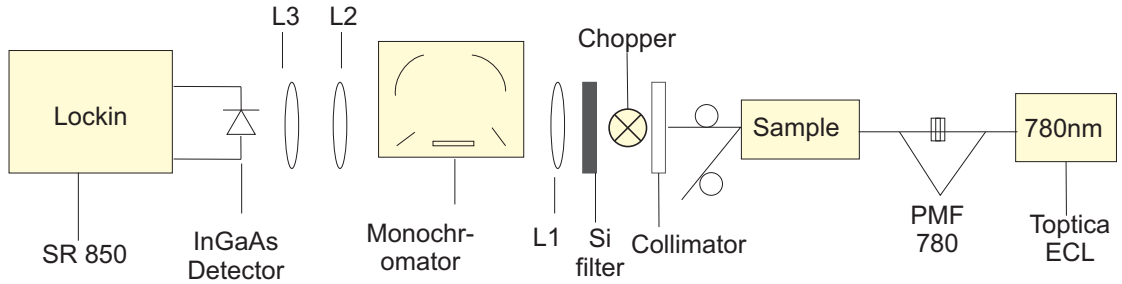
Figure 4.24: Schematic of the set-up used to measure the down conversion after pigtailing. The scheme is the same as the set-up shown in Fig. 4.7 except for replacing the lens L_4 by a fiber port (collimator) and putting the chopper behind the device.

The non-linear efficiency of the down-conversion measured after pigtailing is smaller compared to the earlier measurement. A pump power of 10 mW is available at the input pigtail. The peak current measured by the lockin is 100 fA. The measured fiber-to-fiber down conversion efficiency is smaller than the efficiency measured before pigtailing by a factor of 3. The reason for this could be the photo-refractive damage of the waveguide. The measured FWHM of the SPDC is about 3 nm. The resolution of the monochromator is 1 nm. So the actual FWHM of the SPDC is about 2 nm. This is much higher than the expected FWHM of

48
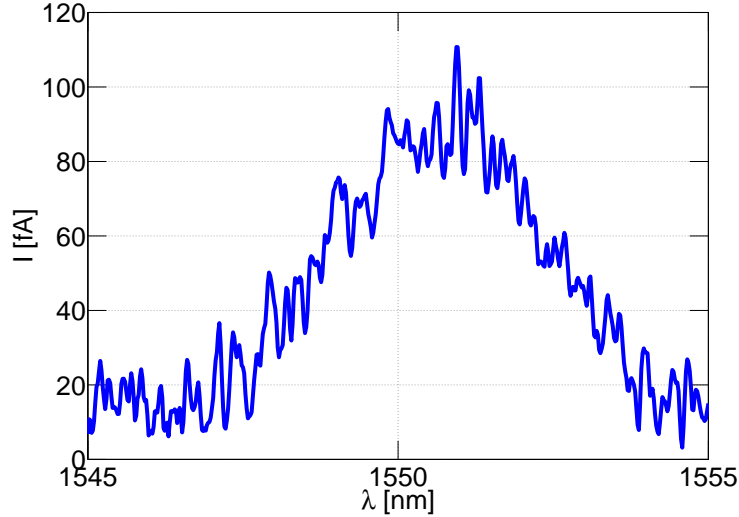
Figure 4.25: The spectrum of down conversion of the TE polarized mode after pigtailing. The FWHM of the spectrum is 2 nm.

0.5 nm. The broadening of the SPDC spectrum also points to photo-refractive damage.

4.5 Photon Pair Generation

The photon pair generation from the packaged source is investigated by coincidence measurements. The schematic of the coincidence measurement setup is shown in Fig. C.1. Light from ECL (λ =780 nm) is used as the pump. The temperature of the sample is stabilized to 40°C. The residual pump photons are reflected by the end-face dielectric mirror. The pump suppression hence achieved is 17 dB. The down-converted photons are coupled out through the pigtails. The TE photons arrive at the pigtail-1 while the TM photons arrive at the pigtail-2. The TE photons later enter the single photon counting detector-1 after passing through the isolator-1. The TM photons enter the single photon counting detector-2 after passing through the isolator-2. The time-to-digital converter (TDC) stores the arrival times of the photons at the detectors. The coincidence measurement process is computer controlled.

Both single photon detectors (id Quantique-201) consist of a cooled avalanche photodiode (APD) with temperature control, as well as biasing, quenching and sensing circuits [50]. The APD is biased above the breakdown voltage (Geiger mode of operation). In this mode, the APD is in a meta-stable state. A photon, if detected, results in the generation of a primary electron-hole pair. The high electric field accelerates the primary electron. The primary electron gains sufficient energy to generate other electron-hole pairs by impact ionization. The process is self-sustaining, resulting in a large macroscopic current even for a single photon detected. The id Quantique detector is biased in a gated mode (Fig. 4.27). The bias is briefly raised above the breakdown by applying the gate voltage. The bias
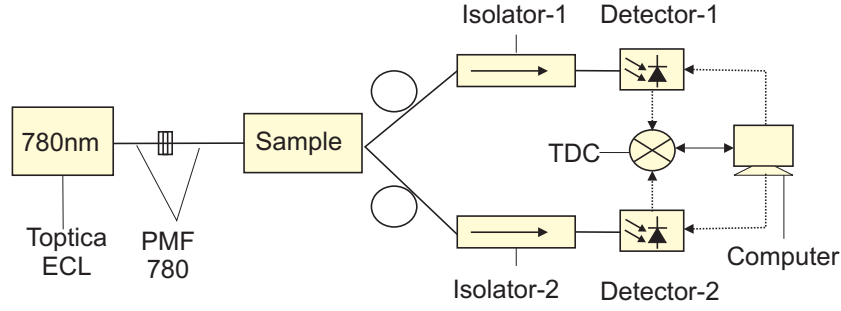
Figure 4.26: Setup for coincidence measurement

duration can be set to 100 ns, 50 ns, 10 ns, 5 ns and 2.5 ns. The detector is only active during this excess bias period.
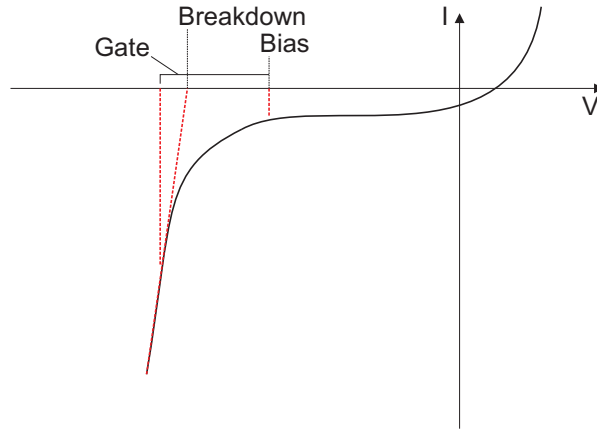
Figure 4.27: Bias, breakdown and gate voltages on the APD.

The duration between the successive gates is carefully chosen to limit the dark counts in the detectors [51; 52]. The primary reason for dark counts is the after-pulse effect. This arises from the trapping of charge carriers during an avalanche by the defects in the high field region of the junction. The maximum life time of the trapped carriers is of the order of $1\,\mu s$. So the maximum rate at which the gate voltage is applied to the APD is limited to 1 MHz. Also, thermally generated carriers also result in dark counts. But this contribution can be neglected, since the APD is thermo-electrically cooled down to $\approx 220\,K$. The detection probability of the APD used can be set to 10 %, 15 %, 20 % and 25 %. In order to achieve a higher detection probability, the gate voltage on the APD has to be increased. But this will also result in a higher dark count rate. This is because, with higher gate voltage there is higher number of filled traps after a detection event, which may result in after pulse. So a compromise has to be found between the detection efficiency and the tolerable dark count rate. Fig 4.28 shows the dependence of dark counts on the trigger rate. With a 25 % detection probability, the dark count rate increases by more than two orders of magnitude as the trigger rate is increased from 1 kHz to 100 kHz. However, with a 10 % detection probability the dark count rate increases only by a factor of 2. The dead time (the time interval between successive gates) is $10\,\mu s$ and gate width is 100 ns for these measurements. The

measurement suggests the use of a smaller detection probability when the photon count rate is low. However, this entails longer measurement duration compared to a measurement at higher detection probability.
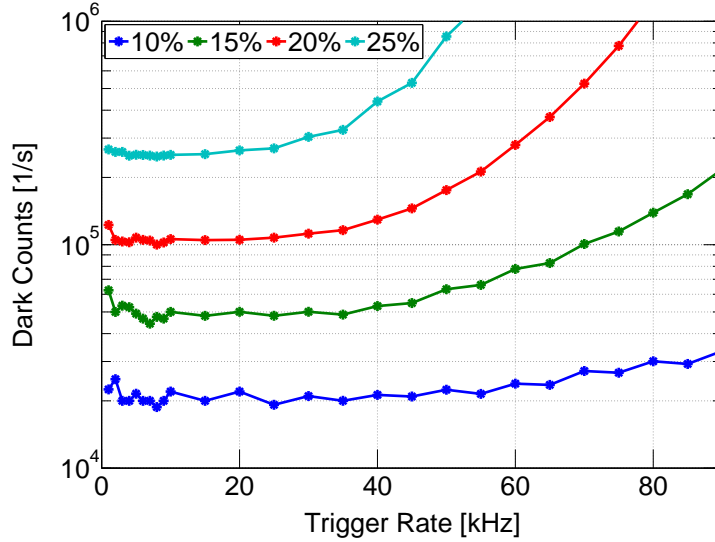
Figure 4.28: Dark count rate as a function of trigger rate. The detection probability is set to 15 % during the subsequent coincidence measurements.

To start the coincident count rate measurement, a computer triggers the Time to Digital Converter (TDC, ACAM ATMD-GPX) [53]. The trigger is generated using the parallel printer port of the computer. The trigger has a transistor-transistor-logic (TTL) voltage level. The voltage level (5 V) is scaled by a factor of roughly 3 by using a potential divider consisting of two resistors. This is necessary because the external trigger input of the TDC has a low-voltage-TTL (LVTTL) logic level. Once the TDC is triggered, two other channels are activated waiting for the stop signals. Meanwhile, the two single photon detectors are also triggered. The gate voltage falls on the APD $\approx$ 13 ns after the detectors are triggered. The gate biases the APD above the break-down voltage for a period set by the gate width. If a photon is detected during the gate, the detector sends out a detect signal (TTL). The quenching circuit immediately biases the gate below the break-down voltage. The detected signal is further scaled down to LVTTL by a potential divider before it is used as a stop signal for the TDC. The computer reads out the stop times from the TDC. The measurement continues by re-triggering the TDC and the detectors until sufficient counts are registered for analysis. The clock cycle for the coincidence measurement is shown in Fig. 4.29.

After reading out the stop times from the TDC, a coincidence histogram is constructed. The histogram plots the number of stop events on the two channels of the TDC as a function of their temporal separation. The coincidence counts measured is shown in Fig. 4.30(a) and Fig. 4.30(b).

The measurement is done with both detectors set to an efficiency of $\eta_{1,2} = 15\%$. The gate width is set to 100 ns. The total number of trigger events is 10 million. So the effective time during which the detector is open is $(10 \times 10^6) \times (100 \times 10^{-9}) =$ 1s. The sharp peak in the figure shows that the arrival times of the photons at the
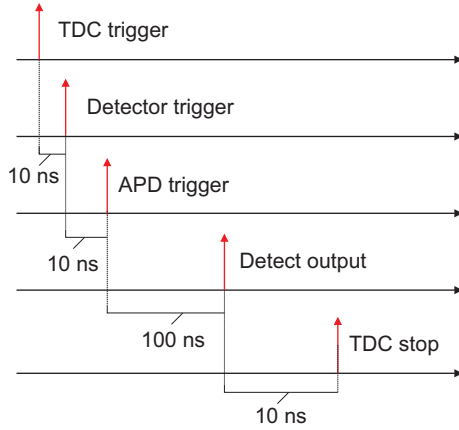
Figure 4.29: Clock cycle of coincidence measurement.

(a) (b)
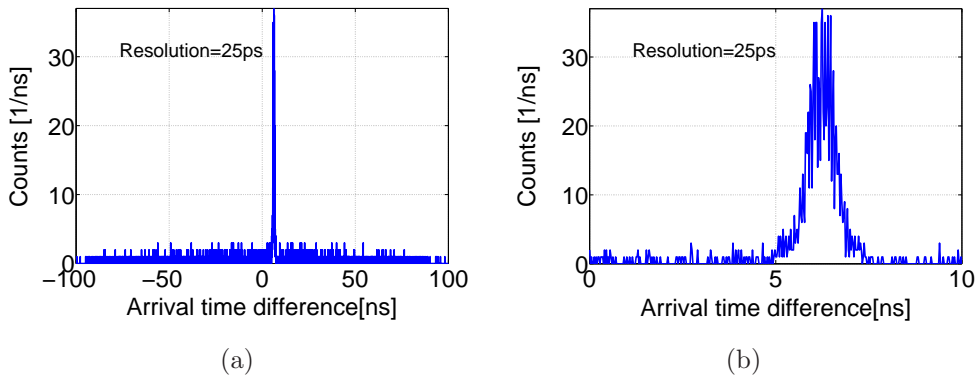
Figure 4.30: (a) Coincident counts as a function of the difference in the arrival times of the photons at the two detectors. Each point is integrated over a period of 25 ps. The correlated counts contribute to the sharp peak. (b) The coincident counts around the peak shown in detail. The offset from zero arrival time difference is mainly contributed by electrical delay and not by optical delay.

detectors are correlated. The figure on the right hand side shows the coincident counts over a short range centered around the peak. The reason for the small offset in the peak from zero arrival time difference is the difference in the electrical path lengths of the stop signals arriving at the TDC. The FWHM of the peak is around 2.5 ns. The FWHM is determined by the jitter in the APDs. The jitter limits the measurement of the actual half-width. The photo-electron requires a finite time to drift from where it is generated to the high field region where the avalanche starts. These regions are often separated in the APD device structure. Depending on how deeply into the detector the photon propagates before it is absorbed, the photoelectron may have a shorter or longer drift delay. Because the spatial probability density for photon absorption is exponential, the depth at which the photon is absorbed has a standard deviation equal to the absorption length. The fluctuations in the drift delay is the main cause of jitter. The resolution of the TDC is $\approx$ 25 ps. This means that the TDC can distinguish between two events, with a temporal separation of 25 ps, at any of its stop channels. In order to find the coincident events due to the down-conversion process we sum over the counts

only ≈ 2.5 ns around the peak.
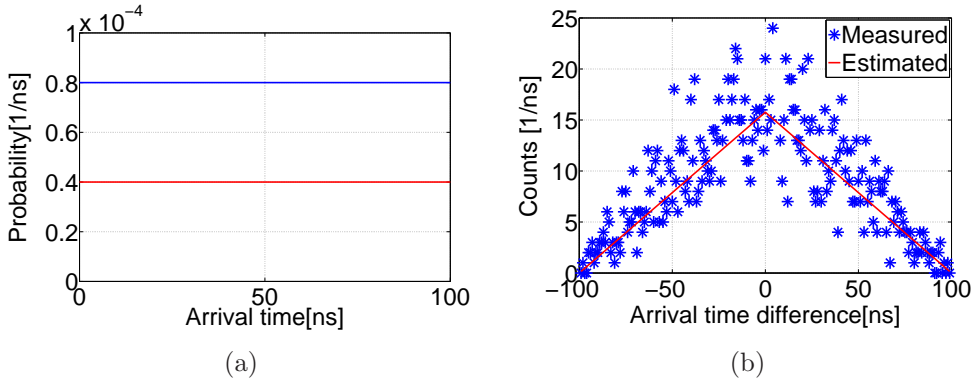
Figure 4.31: (a) Probability distribution function of the singles and the dark counts at the two detectors as a function of the arrival time. A uniform probability distribution is assumed. (b) Measured and calculated distribution of the uncorrelated counts as a function of the difference in the arrival times at the two detectors.

However, there are coincident events due the down-converted photon arriving at one detector and a dark count in the other detector. Similarly, dark counts in the detectors may occur during the same trigger and lead to a coincident event. This is the reason for the background in the coincident count histogram. The dark counts in detector-1 (D_1) and detector-2 (D_2) are $40 \times 10^3 \frac{1}{s}$ and $80 \times 10^3 \frac{1}{s}$ respectively. The arrival time probability of the dark counts is assumed to be uniformly distributed over the duration of a gate. Similarly, the arrival time probability of counts due to down conversion is uniformly distributed over the duration of a gate. Hence the arrival time probability distributions of the D_1 and D_2 are as shown in Fig. 4.31(a). In order to obtain the total dark counts in a detector in a measurement duration of 1 s, we simply multiply the distribution given in $\frac{1}{ns}$ by 10^9. To estimate the distribution of accidental coincidence counts, we correlate the probability distributions corresponding to the three distinct possibilities and add them up. The estimated and measured accidental coincidence rates agree very well.

The correlated counts estimated from the coincidence measurements should be consistent with the efficiency of SPDC measured by using the monochromator. The calculations proceed are shown below. The single count rates in the detectors ($S_{1,2}$) are smaller than the photon pair generation rate (N). The fiber coupling efficiency, transmission losses through the isolators ($\mu_{1,2}$) and the detection efficiency ($\eta_{1,2}$) are responsible for the reduction of the counts measured by the detectors. The dark counts of the detectors ($D_{1,2}$) are also taken into account.
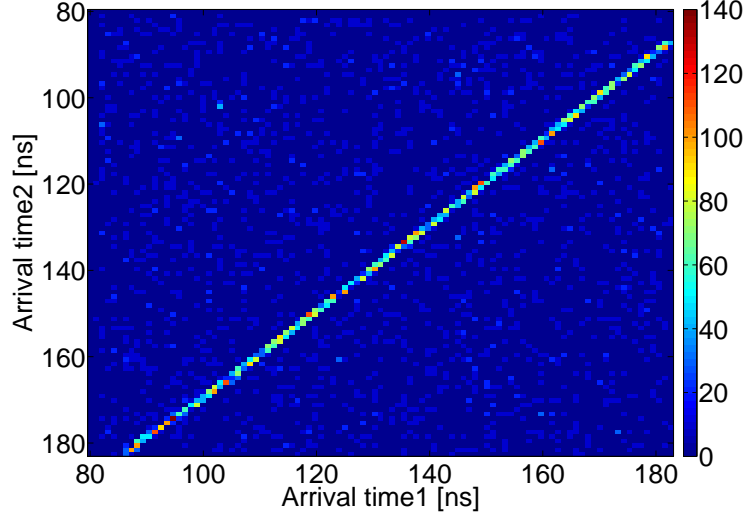
Figure 4.32: The distribution of the *correlated* coincident counts as a function of the arrival times at the two detectors. The white stripe shows the shows the correlated counts. They are uniformly distributed over the entire gate (100 ns). The uncorrelated coincident counts are the dots outside the white stripe.

The single count rates and the coincident count rates are modeled as follows:

$$
\begin{aligned}
S_1 &= \mu_1\,\eta_1\,N + D_1 & S_1 &\approx 113 \times 10^3,\ \eta_1 = 15\%,\ D_1 \approx 40 \times 10^3 \\
S_2 &= \mu_2\,\eta_2\,N + D_2 & S_2 &\approx 170 \times 10^3,\ \eta_2 = 15\%,\ D_2 \approx 80 \times 10^3 \\
R &= \mu_1\,\mu_2\,\eta_1\,\eta_2\,N & R &\approx 10^3 \\
\Rightarrow N &= \frac{(S_1 - D_1)\,(S_2 - D_2)}{R} \\
&= 5.7 \times 10^6 \\
\Rightarrow \mu_1 &= \frac{S_1 - D_1}{\eta_1\,N} & \mu_2 &= \frac{S_2 - D_2}{\eta_2\,N} \\
&= 9\% & &= 10\%
\end{aligned}
$$

The $\mu_{1,2}$ estimated ($\approx 10\%$) includes both the fiber coupling efficiency and the trasmission through the different components. The measured value of the transmission from the input port of the isolator to the single photon detector is -2 dB. Hence, the fiber coupling efficiency calculated is $\approx 16\ \%$ for both the pigtails.

The pump power available at the input pigtail for this measurement is $\approx 95\ \mu$W. The number of photon pairs generated inside the sample is $\approx 5.7 \times 10^6\ \frac{1}{s}$. The generation rate normalized to the pump power is $60 \times 10^6\ \frac{1}{s \cdot mW}$. The conversion efficiency normalized to the pump photon rate is $10^{-7}\ \%$. This is one order higher than the conversion efficiency estimated by the SPDC measurement before pigtailing. Two possible reasons are postulated for this difference. One, the SPDC measurement is done at a relatively high pump power of 10 mW. The photo-refractive damage may reduce the non-linear efficiency. Second, the pair generation rate estimated from the coincidence measurement may be higher than the actual value. Excess single counts in the detectors may result from unwanted processes in the

sample. Considering these two aspects, an agreement within one order of magnitude between the SPDC measurement and the coincidence measurement results is satisfactory.

In order to compare the performance of the fiber pigtailed device with other sources, we define a metric called brightness (B). With a pump power P_p, emission bandwidth $\Delta\lambda$ and coincidence count rate R, brightness is defined as

$$B \equiv \frac{R}{P_p\,\Delta\lambda} \qquad\qquad R = \frac{10^3}{0.15^2\,\times\,0.63^2}\left[\frac{1}{s}\right]$$

$$= \frac{45\,\times\,10^3\left[\dfrac{1}{s}\right]}{0.095\,[\text{mW}]\,\times\,0.5\,[\text{nm}]}$$

$$= 10^6\,\frac{1}{s\cdot\text{mW}\cdot\text{nm}}$$

$$= 10^4\,\frac{1}{s\cdot\text{mW}\cdot\text{GHz}}$$

The comparison is summarized in the table below. The brightness of the fiber pigtailed source is one order below compared to the results reported in the literature. A similar configuration by Fuji [54] reports a brightness of $6 \times 10^6\,\frac{1}{s\cdot\text{GHz}\cdot\text{mW}}$. The scheme uses ridge waveguide instead of a channel waveguide. The ridge waveguide has better confinement of all the three interacting fields and better overlap compared to the channel waveguide. A source operating with $\lambda = 1310$ nm as degeneracy point, based on type II down conversion reported a brightness of $10^5\,\frac{1}{s\cdot\text{GHz}\cdot\text{mW}}$. The waveguide losses in this case is very low, less than $0.1\,\frac{\text{dB}}{\text{cm}}$, for both polarizations. In our structure the waveguide losses (measured on an adjacent waveguide in the same group) is $\alpha_{\text{TE}} = 0.25\,\frac{\text{dB}}{\text{cm}}$ and $\alpha_{\text{TM}} = 0.3\,\frac{\text{dB}}{\text{cm}}$. The decision to choose the waveguide group with relatively high loss is to use the polarization beam splitter in the same group with the most desirable splitting ratio. Brightness of the same order $10^4\,\frac{1}{s\cdot\text{GHz}\cdot\text{mW}}$ is reported by Suhara [15]. The brightness is achieved in a channel waveguide with length 30 mm.

Table 4.2: Comparison of different photon pair sources.

Reference	Configuration	Brightness$[\frac{1}{s\cdot\text{mW}\cdot\text{GHz}}]$
Fuji [54]	Type II 1550 nm	$6\,\times\,10^6$
Martin [16]	Type II 1310 nm	10^5
Suhara [15]	Type II 1550 nm	10^4

The comparison points to the scope of improvement of the brightness of our structure by at least one order of magnitude. This can be achieved by reducing the waveguide losses, excess loss in the polarization beam splitter and improvement in

Conclusion

A pigtailed and packaged integrated photon pair source is presented. Design issues and experimental results concerning the different components of the source, including the waveguide, polarization splitter and dielectric mirror, are explained in detail. The photon pair generation from the source is investigated by a coincidence counting experiment using two single photon detectors. The pair generation rate estimated from the measurement is $10^4 \, \frac{1}{\mathrm{s\,GHz\,mW}}$. The pair generation rate is compared with the results reported in the literature. Finally, different possible ways in which an improvement in performance can be achieved is mentioned.

Chapter 5

Entangled Photon Pair Source with Interlaced Domain Structure

Entangled photon pair sources are essential devices for quantum key distribution. Different approaches have been used to generate entangled photon pairs. Polarization entangled photon pair sources with high efficiency and brightness based on SPDC have been demonstrated with Ti:LiNbO$_3$ waveguides of homogeneous domain structure. Such sources operate at degeneracy, i.e., both the down converted photons have the same wavelength. In this chapter, a new scheme of generating entangled photon pairs is presented. Unlike the conventional scheme, the entangled photon pairs are at non-degeneracy. This is achieved by an interlaced domain structure.

In the first section, the principle of polarization entanglement is explained in detail. A schematic of the entangled photon pair source is presented. The drawback of the conventional scheme at degenerate wavelengths is discussed. A new scheme with interlaced domain structure is presented. The simplest way to understand the principle of interlaced domains is through the second harmonic generation process. Hence design as well as experimental results concerning second harmonic generation in interlaced structure are presented. Also results of spontaneous parametric down conversion are presented. In the third and final section the characterization of the entangled photon pair source is discussed in detail. Comparison with existing schemes is presented.

5.1 Polarization Entanglement

Polarization entanglement is a correlation between four optical modes at two different locations. The correlation can only be explained by a quantum theory of optical fields. In the case of polarization entanglement, the photon arriving at a location, after measurement, can be either TE or TM polarized. Subsequent measurement of the second photon at the second location will show an orthogonal polarization, irrespective of the outcome of the first measurement. The conventional scheme, based on type II SPDC to generate polarization entangled photons is shown in Fig. 5.1.

As shown in the figure, the downconverted photons have the same wavelength, but orthogonal polarizations. The beam splitter behind the source redirects the generated photons, into its output arms. There are four different ways in which the photons are redirected. The joint state at the output of the beam splitter is
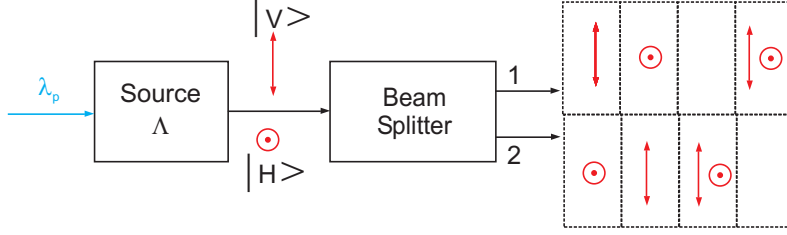
Figure 5.1: Conventional scheme to generate polarization entanglement. Only half of the generated pairs contribute to polarization entanglement. The pump photon λ_p travelling through the waveguide with poling period Λ down converts into two longer wavelength cross-polarized photons. The beam splitter behind the source redirects the output photons into two output ports. The four possibilities are shown in the boxes.

written as

$$|\psi\rangle_{12} = \frac{1}{2}\{ \underbrace{|V\rangle_1 |H\rangle_2 + |V\rangle_2 |H\rangle_1}_{\text{arrival at different locations}} + \underbrace{|V\rangle_1 |H\rangle_1 + |V\rangle_2 |H\rangle_2}_{\text{arrival at same location}} \},$$
$$\text{with} \quad {}_{12}\langle\psi|\,\psi\rangle_{12} = 1$$

In the above equation, subscripts 1 and 2 indicate the spatial locations. V and H states are the single photon states corresponding to vertically ($\equiv$ TM) and horizontally ($\equiv$ TE) polarized modes. The first two states correspond to case where both photons arrive at separate output ports. The last two states represent the case when both photons arrive at the same output port. All the four cases have the same probability indicated by the equal weightages in the superposition state. However, the last two terms do not represent entangled state. They do not contribute to any coincident counts unlike the first two terms. The joint state at the output of the beam splitter, after post-selection by a coincidence measurement is

$$|\psi\rangle_{12} = \frac{1}{2}\{ |V\rangle_1 |H\rangle_2 + |V\rangle_2 |H\rangle_1 \}. \tag{5.2}$$

The single photon states of all the four modes involved are at the same frequency. The drawback of the conventional scheme is that only half of the down converted photons contribute to entanglement.

A new scheme of polarization entanglement without post-selection has been demonstrated by Suhara [55]. The scheme is based on type II down conversion at non-degeneracy. The interaction region consists of two sections; both sections are periodically poled, but the second section has a Ta_2O_5 cladding layer (refractive index ≈ 2). The section with the cladding layer, even though has the same periodicity as the first section, will contribute to a different type II down conversion process. Therefore, the wavelength of emission of the down-converted photons in the section with the cladding layer is offset from the section without the cladding layer. In order to achieve polarization entanglement, the pump wavelength is chosen such that orthogonally polarized emissions from the two regions have the same wavelength. A wavelength division de-multiplexer behind the interaction region separates the down-converted photons depending on their wavelengths (λ_1

and λ_2). The joint state at the two output ports of the de-multiplexer is

$$|\psi\rangle_{12} = \frac{1}{\sqrt{2}} \left\{ |H\rangle_1 |V\rangle_2 + e^{i\delta} |V\rangle_1 |H\rangle_2 \right\}. \qquad (5.3)$$

The subscripts 1 and 2 indicate the output ports of the de-multiplexer. The phase difference, δ, between $|H\rangle$ and $|V\rangle$ arises from the birefringence of the interaction region. The advantage of the source is that it is post-selection procedure is not needed.

We propose a new scheme to generate the same polarization entangled state [56]. The new scheme uses two different poling periodicities in the same waveguide as shown schematically in Fig. 5.2. The scheme has many advantages compared to the scheme by Suhara.
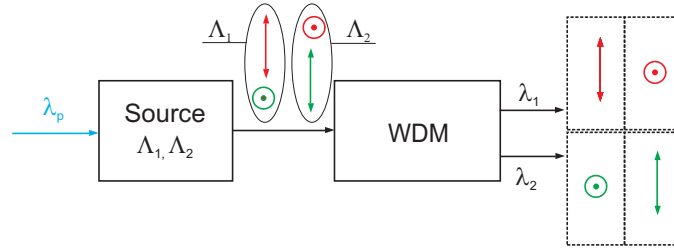
Figure 5.2: New scheme to generate polarization entanglement. All the generated pairs contribute to polarization entanglement. Entanglement is obtained at non-degeneracy.(WDM: Wavelength Division Multiplexer)

With two different poling periods (Λ_1 and Λ_2), two photon pairs corresponding to two independent SPDC processes are generated. The poling periods are chosen in such a way that the emission wavelength of the TE photon corresponding to the first process coincides with the emission wavelength of the TM photon of the second process. Similarly, the emission wavelength of the TM photon of the first process coincides with the emission wavelength of the TE photon of the second process. The wavelength division multiplexer behind the source redirects the photons with equal wavelengths to the same output port. However, the polarization of the photon arriving at the output port could be either vertical or horizontal. Whenever a photon is observed at output 1, a photon of orthogonal polarization and different wavelength can be simultaneously observed at output 2 and vice versa. The phase matching conditions of the two independent processes are summarized by the following equations.

$$\begin{aligned} \beta_p &= \beta_{TE1} + \beta_{TM1} + \beta_{\Lambda1} \\ &= \beta_{TE2} + \beta_{TM2} + \beta_{\Lambda2}, \end{aligned} \qquad (5.4)$$

where $\beta_{p,TE,TM}$ are the propagation constants of the pump, TE- and TM-polarized signal and idler fields respectively. $\beta_{\Lambda1,\Lambda2}$ are the wave vectors associated with the domain periods $\Lambda_{1,2}$. The subscripts 1 and 2 indicate down conversion corresponding to Λ_1 and Λ_2, respectively. The pump wavelength has to be carefully chosen to guarantee that the emission wavelength of a polarization in one process coin-

cides with the emission wavelength of the orthogonal polarization in the second process. Once this is satisfied, the energy conservation conditions ensure that the emission wavelengths of the remaining polarizations coincide. This is proved formally below.

$$
\begin{aligned}
\omega_{\mathrm{p}} &= \omega_{\mathrm{TE1}} + \omega_{\mathrm{TM1}} \quad (\text{with} \quad \omega_{\mathrm{TE1}} = \omega_{\mathrm{TM2}}) \\
\Rightarrow \omega_{\mathrm{TM1}} &= \omega_{\mathrm{p}} - \omega_{\mathrm{TE1}} \\
&= \omega_{\mathrm{p}} - \omega_{\mathrm{TM2}} \\
\Rightarrow \omega_{\mathrm{TM1}} &= \omega_{\mathrm{TE2}},
\end{aligned}
\tag{5.5}
$$

where $\omega_{\mathrm{p,TE,TM}}$ are the emission frequencies of the pump, TE and TM fields respectively. The subscripts 1 and 2 indicate down conversion corresponding to Λ_1 and Λ_2 respectively. The design issues of the source with two poling periods are discussed in the next section.

(a)

(b)

(c)
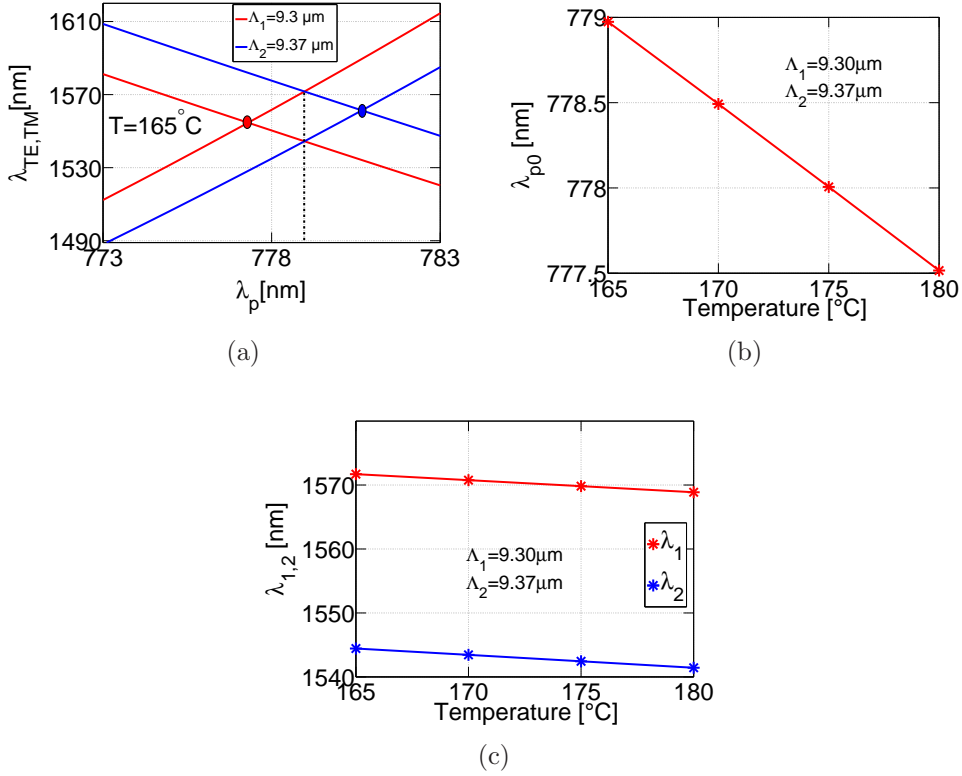
Figure 5.3: (a) Calculated phase matching curves for type II SPDC at $165^{\circ}C$. At the operating point ($\lambda_{\mathrm{p0}} = 779$ nm) the wavelengths of the down converted photon pairs are $\lambda_1 = 1544$ nm and $\lambda_2 = 1572$ nm. (b) Temperature tuning characteristic of the operating point (λ_{p0}). The slope is $\approx -68 \frac{\mathrm{pm}}{^{\circ}\mathrm{C}}$. (c) Wavelengths of the photon pairs generated at operation point as a function of temperature. The slope of $\approx -138 \frac{\mathrm{pm}}{^{\circ}\mathrm{C}}$ is the same for either wavelength.

5.2 Design of Interlaced Domains

The domain periods are chosen such that the photon pairs generated have wavelength in the 1550 nm range. The calculated phase matching curve of type II down conversion at 165°C is shown in Fig. 5.3(a). The red lines represent the tuning characteristics with $\Lambda_1 = 9.30\ \mu\text{m}$. They intersect at the degeneracy point, $\lambda = 1553$ nm (red dot). The blue lines represent the tuning characteristics with $\Lambda_2 = 9.37\ \mu\text{m}$. They intersect at the degeneracy point $\lambda = 1560$ nm (blue dot). The lines with a positive slope correspond to TE emission and those with negative slope correspond to TM emission. The TE emission of Λ_1 meets the TM emission of Λ_2 at a pump wavelength of λ_{p0}. At the same pump wavelength, the TM emission of Λ_1 meets the TE emission of Λ_2. The pump wavelength λ_{p0} is defined as the operating point of entanglement (shown by dashed line). The operating point depends, in addition to the domain periods and their separation, on the temperature. The temperature tuning characteristics of the operating point is shown in Fig. 5.3(b). The slope is $\approx -68\ \frac{\text{pm}}{°\text{C}}$. The wavelengths of the photon pairs generated are shown in Fig. 5.3(c). The calculations show a limited range of tunability of the source by temperature tuning. The slope is the same for either wavelength ($\approx -138\ \frac{\text{pm}}{°C}$).

The waveguide is poled with two different periodicities. The first half of the waveguide is poled with periodicity Λ_1 and the second half with Λ_2. The conversion efficiencies of down conversion in the two regions are same provided the interaction lengths are same and propagation losses are negligible. However, this sequential structure has a drawback. The photons generated by the first process arrive at different times at the detectors. The arrival time difference (τ_a) is dependent on the group velocity difference between the orthogonally polarized photons and the length of the waveguide. Similarly, there is an arrival time difference of the photons generated by the second process (τ_b). The arrival time difference between the photons corresponding to the first process is maximum if they are created at $z = 0$. The arrival time difference is minimum if they are created at $z = \frac{L}{2}$. Hence, on an average, the arrival time difference, τ_a is

$$\tau_\text{a} = \frac{1}{2}\underbrace{\left[\frac{L}{V_{\text{TE}}(\lambda_2)} - \frac{L}{V_{\text{TM}}(\lambda_1)}\right]}_{\Lambda_1\text{process}} + \frac{1}{2}\underbrace{\left[\frac{\frac{1}{2}L}{V_{\text{TE}}(\lambda_2)} - \frac{\frac{1}{2}L}{V_{\text{TM}}(\lambda_1)}\right]}_{\Lambda_2\text{process}}$$

$$= \frac{3}{4}\left[\frac{L}{V_{\text{TE}}(\lambda_2)} - \frac{L}{V_{\text{TM}}(\lambda_1)}\right] \tag{5.6}$$

Similarly for the photons corresponding to the second process, the arrival time difference is maximum if they are created at $z = \frac{L}{2}$ and no arrival time difference if they are created at $z = L$. Hence, on an average, the arrival time difference, τ_b is

$$\tau_\text{b} = \frac{1}{4}\left[\frac{L}{V_{\text{TE}}(\lambda_1)} - \frac{L}{V_{\text{TM}}(\lambda_2)}\right] \tag{5.7}$$

In the above equations, V is the group velocity of a photon. The subscripts indicate the polarization. In order to enhance the in-distinguishability of the photons,

it is necessary to compensate the arrival time differences, τ_a and τ_b. The compensation is achieved by using a birefringent medium behind the source. The length ($\approx 5\,\mathrm{m}$) and orientation of the birefringent medium has to be chosen carefully to compensate for the arrival time difference. However, since $\tau_a \neq \tau_b$,the compensation is not exact for both processes. The inexact compensation of the arrival time differences, τ_a and τ_b, is one of the drawbacks of the scheme proposed by Suhara. One way to overcome this drawback is to use an interlaced domain structure. In this case, segments with different periodicities are distributed through out the waveguide. The two approaches are shown schematically in Fig. 5.4.
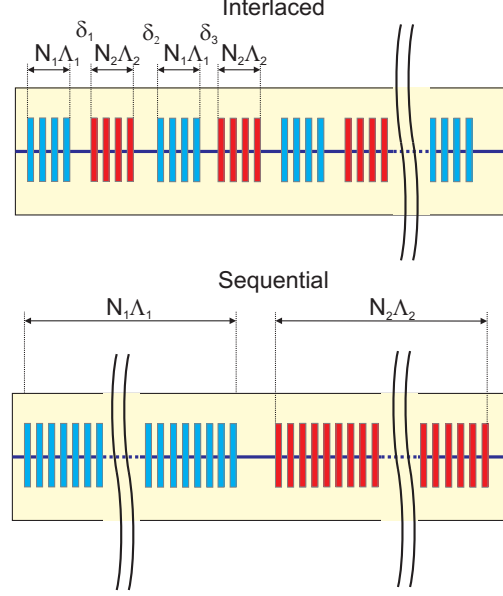
Figure 5.4: Layout with interlaced (top) and sequential (bottom) domain structures. With interlaced structure, the two different segments are distributed through out the interaction region. Between successive segments, a region ($\delta_{1,2}$) is introduced so that the phase relationships are maintained between the interacting fields. With sequential structure, only two long segments are present. The two different periodicities ($\Lambda_{1,2}$) are shown by two colors. $N_{1,2}$ are the number of domain periodicities in each segment.

As already mentioned in the introduction, calculations concerning phase matching behavior of second harmonic generation in such an interlaced structure are easier to understand compared to calculation of down conversion. Hence, to study the interlaced structure, second harmonic generation is simulated by solving the coupled mode equations. The evolution equations of the complex amplitudes corresponding to second harmonic and the fundamental fields are discussed in detail in chapter 1 (Eq. 2.18). We are operating in the regime where the depletion of the energy in the fundamental field, due to the transfer to second harmonic field, is negligible. Formally, this means $\partial_z A_{TE} \approx \partial_z A_{TM} \approx 0$. A closed form solution exists for the evolution of A_{SH} and is shown in Eq. 5.8.

$$A_{SH}(z) = A_{SH}(0) + \frac{i2\omega_{SH}\,d_{31}\,\eta}{n_{SH}c}\,A_{TE}(0)\,A_{TM}(0)\,\frac{[e^{i\Delta\beta z} - 1]}{i\Delta\beta} \qquad (5.8)$$

The variable $\Delta\beta = \beta_{TE} + \beta_{TM} - \beta_{SH}$ is the phase mismatch between the non-linear

polarization and the traveling electric field at at ω_{SH}. A_{SH} is the slowly varying amplitude of the generated second harmonic field. A_{TE} and A_{TM} are the slowly varying amplitudes of the TE and TM polarized fields respectively, associated with the fundamental wave. The closed form solution is helpful to calculate the SH power generated after the whole interaction region. This is done by solving for the SH field after each domain in an iterative manner. The steps involved are as follows.

1. Evolution in the first domain z=0 to z=$\frac{\Lambda}{2}$ (shown by red arrow in the figure)
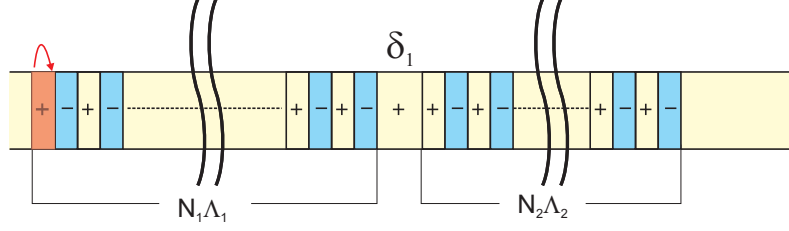
$$A_{\text{SH}}(0) \rightarrow A_{\text{SH}}\left(\frac{\Lambda}{2}\right)$$
$$A_{\text{SH}}\left(\frac{\Lambda}{2}\right) \rightarrow A_{\text{SH}}\left(\frac{\Lambda}{2}\right) e^{i\beta_{\text{SH}}\frac{\Lambda}{2}}$$
$$A_{\text{TE}}\left(\frac{\Lambda}{2}\right) = A_{\text{TE}}(0) e^{i\beta_{\text{TE}}\frac{\Lambda}{2}} \qquad (5.9)$$
$$A_{\text{TM}}\left(\frac{\Lambda}{2}\right) = A_{\text{TM}}(0) e^{i\beta_{\text{TM}}\frac{\Lambda}{2}}$$

2. Evolution in the inverted domain (z=$\frac{\Lambda}{2}$ to z=Λ)
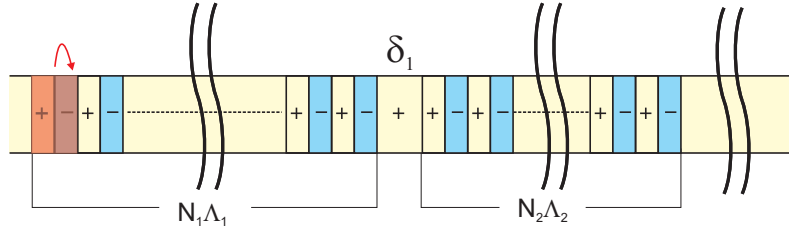
$$A_{\text{SH}}\left(\frac{\Lambda}{2}\right) \rightarrow A_{\text{SH}}(\Lambda)$$
$$A_{\text{SH}}(\Lambda) \rightarrow A_{\text{SH}}(\Lambda) e^{i\beta_{\text{SH}}\frac{\Lambda}{2}}$$
$$A_{\text{TE}}(\Lambda) = A_{\text{TE}}\left(\frac{\Lambda}{2}\right) e^{i\beta_{\text{TE}}\frac{\Lambda}{2}}$$
$$A_{\text{TM}}(\Lambda) = A_{\text{TM}}\left(\frac{\Lambda}{2}\right) e^{i\beta_{\text{TM}}\frac{\Lambda}{2}}$$

3. Steps 1 and 2 are repeated until the SH evolution is calculated along all the

domains in the segment.
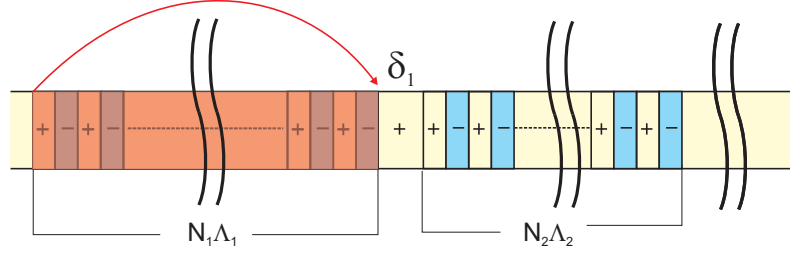
4. Phase adjustment region (δ_1). The phase relationship between the interacting fields in the segment with poling period Λ_1 changes after the segment with poling period Λ_2. In order to ensure the growth of SH field in the second segment with poling period Λ_1, it is necessary that phase relationship is the same at the end of the first segment with the same periodicity. This is ensured by choosing the length of the region δ_1, such that $N_2\Lambda_2 + \delta_1$ is a multiple of Λ_1.
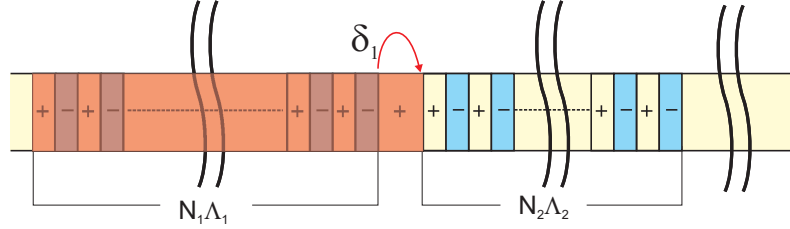
$$
\begin{aligned}
A_{SH}(N_1\Lambda_1) &\rightarrow A_{SH}(N_1\Lambda_1) \times e^{i\beta_{SH}\delta_1} \\
A_{TE}(N_1\Lambda_1) &\rightarrow A_{TE}(N_1\Lambda_1) \times e^{i\beta_{TE}\delta_1} \\
A_{TM}(N_1\Lambda_1) &\rightarrow A_{TM}(N_1\Lambda_1) \times e^{i\beta_{TM}\delta_1}
\end{aligned}
\tag{5.10}
$$

5. Steps 1 to 4 are repeated in all the segments in the waveguide.

SH generated in a 50 mm long waveguide is calculated using this method. The waveguide is poled with two different periodicities, $\Lambda_1 = 9.07\,\mu$m and $\Lambda_2 = 9.14\,\mu$m. A sequential structure is realized in 50 mm long guide. There are only two segments in the waveguide with $N_1 = 3000$ and $N_2 = 2490$. The result is summarized in Fig. 5.5. As shown in the figure, two distinct peaks ($\lambda_1 = 1553$ nm and $\lambda_2 = 1560$ nm) appear, which correspond to the two different poling periods. The effective length of interaction corresponding to Λ_1 is $N_1\Lambda_1 = 27.2$ mm and that of Λ_2 is $N_2\Lambda_2 = 22.8$ mm. Since the SH efficiency scales proportional to the square of the length of interaction, the amplitude of the second peak is $\frac{22.8^2}{27.2^2} = 70\,\%$ of that of the first peak. The difference in the interaction lengths of the two processes is also reflected in the phase matching bandwidths. The FWHM of the first peak is $\Delta\lambda_1 = 280$ pm. Since the FWHM scales inversely with the interaction length, the FWHM of the second peak is $\Delta\lambda_2 = \frac{27.2}{22.8} \times 180 = 330$ pm.

Fig. 5.6 corresponds to the case where more than two segments are present in the waveguide. In addition to the two main peaks, satellite peaks appear in the phase matching spectrum. The presence of satellite peaks is due to the modulation
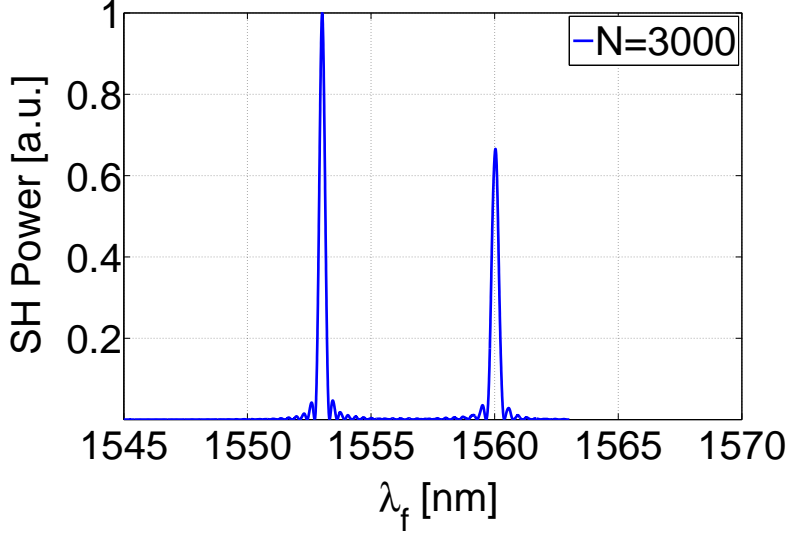
Figure 5.5: Calculated phase matching spectrum of SH from a sequential structure with $N_1 = 3000$ and $N_2 = 2490$. The temperature is 35°C, $\Lambda_1 = 9.07\,\mu$m and $\Lambda_2 = 9.14\,\mu$m

of the homogeneous domain structure. With 100 domain periods per segment, the two strongest satellite peaks appear 5 nm above and below the main peak. The location of the peaks seen in SH phase matching spectrum is the location of the degeneracy points in down conversion. The appearance of satellite peaks in the SH phase matching spectra point to additional degeneracy points in down conversion. The unwanted down conversion will deteriorate the quality of entanglement and hence, should be avoided. This is done by pushing the satellite peaks further away by decreasing the number of domains in each segment. With 10 domain periods per segment, the two strongest satellite peaks are pushed further away, and lie 40 nm above and below the main peak. However, the amplitude of the satellite peaks, relative to the main peaks, remain unchanged at 40 %.

Satellite peaks appear for both processes. The two main satellite peaks lie on either side of the main peak of each process. These peaks correspond to the wavelength whose coherence length of interaction exactly equals the length of a segment. To understand the evolution of the satellite peaks along the interaction region, we take a closer look at the phase matching spectrum corresponding to N=500 domain periods per segment. In addition to the main peak at $\lambda_f = 1553$ nm, the satellite peaks at $\lambda = 1552.1$ nm and $\lambda = 1553.9$ nm are the processes phase matched by Λ_1. Similarly, the satellite peaks at $\lambda = 1559.1$ nm and $\lambda = 1560.9$ nm are the processes phase matched by Λ_2. The coherence length of interaction of the satellites of the first process is $N_1\,\Lambda_1$. Similarly, the coherence length of interaction of the satellites of the second process is $N_2\,\Lambda_2$. The growth of the center peak and the satellites at $\lambda = 1552.1$ nm and $\lambda = 1553.9$ nm are shown in Fig. 5.6(d).

The satellites as well as the main peak which grow in the first segment, transfers energy back to the fundamental when they enter the second segment with a different periodicity. The curvature of the evolution of the main peak is a constant in the first segment. This is the characteristic of a parabolic growth at the exact
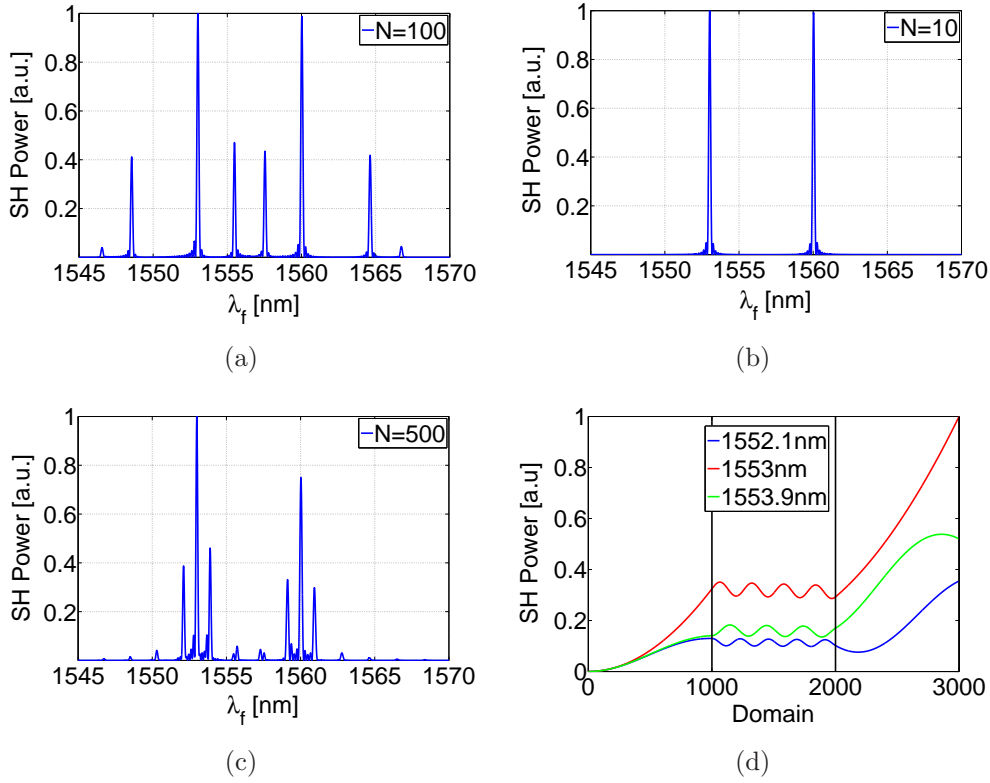
Figure 5.6: (a) Calculated phase matching spectrum of SH from a sequential structure with $N_1 = N_2 = 100$. The temperature is 35°C, $\Lambda_1 = 9.07\,\mu$m and $\Lambda_2 = 9.14\,\mu$m. The main satellite peaks are offset by ≈ 4 nm from the main peaks. (b) Phase matching spectrum with $N_1 = N_2 = 10$. The satellite peaks are ≈ 70 nm away from the main peaks. (c) Phase matching spectrum with $N_1 = N_2 = 500$. The satellite peaks are ≈ 1 nm away from the main peaks. (d) The evolution of satellite peaks, $\lambda = 1552.1$ nm and $\lambda = 1553.9$ nm in the first three segments. Also shown is the evolution of the main peak at $\lambda = 1553$ nm.

phase matching wavelength. However the curvature of the satellites change in the first segment. The coherence lengths of the satellites in the first segment are shown below.

$$L_{c1} = L_{c2} = N_1 \times \Lambda_1$$

$$\Delta\beta_1 = -\left[\frac{2\pi}{\Lambda_1} + \frac{\pi}{N_1 \times \Lambda_1}\right] \qquad \text{(at } \lambda = 1552.1 \text{ nm)}$$

$$\Delta\beta_2 = -\left[\frac{2\pi}{\Lambda_1} - \frac{\pi}{N_1 \times \Lambda_1}\right] \qquad \text{(at } \lambda = 1553.9 \text{ nm)}$$

In the second segment the coherence lengths are calculated as follows.

$$L_c = \frac{\pi}{\Delta\beta + \frac{2\pi}{\Lambda_2}} = \frac{\pi}{-\frac{2\pi}{\Lambda_1} + \frac{2\pi}{\Lambda_2}}$$

$$= \frac{1}{2}\left[\frac{1}{-\frac{1}{\Lambda_1} + \frac{1}{\Lambda_2}}\right] \approx 592 \ \mu\text{m} \ [130 \text{ domains for the peak}]$$

$$L_{c1} = \frac{\pi}{\Delta\beta + \frac{2\pi}{\Lambda_2}} = \frac{\pi}{-\frac{2\pi}{\Lambda_1} - \frac{\pi}{N_1\Lambda_1} + \frac{2\pi}{\Lambda_2}}$$

$$= \left[\frac{1}{-\frac{2}{\Lambda_1} + \frac{2}{\Lambda_2} - \frac{1}{N_1\,\Lambda_1}}\right] \approx 524 \ \mu\text{m} \ [115 \text{ domains for the satellite 1}]$$

$$L_{c2} = \frac{\pi}{\Delta\beta + \frac{2\pi}{\Lambda_2}} = \frac{\pi}{-\frac{2\pi}{\Lambda_1} + \frac{\pi}{N_1\Lambda_1} + \frac{2\pi}{\Lambda_2}}$$

$$= \left[\frac{1}{-\frac{2}{\Lambda_1} + \frac{2}{\Lambda_2} + \frac{1}{N_1\,\Lambda_1}}\right] \approx 681 \ \mu\text{m} \ [149 \text{ domains for the satellite 2}]$$

The power in the satellites at the end of the first segment are exactly equal. Relative to the center peak, the power is a factor of $\left[\frac{2}{\pi}\right]^2$ lower. The reason for this is clear from the solution of coupled mode equations (Eq. 5.8). The wavelength dependence arises primarily from the term $\frac{[e^{i\Delta\beta z}-1]}{i\Delta\beta}$ in the closed form solution. At $z = N_1\Lambda_1$,

$$\frac{[e^{i\Delta\beta z} - 1]}{i\Delta\beta} = N_1 \Lambda_1 \qquad \Delta\beta = 0 \text{ for the center peak}$$

$$\frac{[e^{i\Delta\beta z} - 1]}{i\Delta\beta} = \pm \frac{2}{\pi} N_1 \Lambda_1 \qquad \Delta\beta = \pm\frac{\pi}{N_1\Lambda_1} \text{ for satellites}$$

The factor of $\frac{2}{\pi}$ in the closed form solution accounts for the smaller SH power in the satellites. In the second segment, a portion of the energy goes back and forth between the SH and the fundamental. The peak to peak amplitudes and the periodicities of these oscillations depend on the coherence length.

A formal interpretation of the satellite peaks is based on the spatial Fourier decomposition of the interlaced poling pattern. The spatial distribution of the

non-linear coefficient $\chi^{(2)}(z)$ is as follows.

$$
\chi^{(2)}(z) = d_{31} \underbrace{\overbrace{\sum_{m=0}^{m=\infty} \mathrm{rect}\left(\frac{z - mN_2\Lambda_2}{N_1\Lambda_1}\right)}^{\text{interlacing}} \times \underbrace{\square\left(\frac{z}{\Lambda_1}\right)}_{\Lambda_1 \text{ poling}}}_{\Lambda_1 \text{ process}} +
$$

$$
d_{31} \underbrace{\overbrace{\sum_{m=1}^{m=\infty} \mathrm{rect}\left(\frac{z - mN_1\Lambda_1}{N_2\Lambda_2}\right)}^{\text{interlacing}} \times \underbrace{\square\left(\frac{z}{\Lambda_2}\right)}_{\Lambda_2 \text{ poling}}}_{\Lambda_2 \text{ process}}
$$

(5.14)

The expression for $\chi^{(2)}(z)$ contains two parts, first part representing sections with poling periodicity Λ_1 and second part representing sections with poling periodicity Λ_2. Each part contains rectangular functions and a square function, $\square$. The rectangular functions sum over different sections with the same periodicity. The square function $\square(\frac{z}{\Lambda_{1,2}})$ represents a square wave with periodicity $\Lambda_{1,2}$. The *rect* function is defined as

$$
\mathrm{rect(x)} = 1 \qquad \text{for} |x| < \frac{1}{2}
$$

$$
= 0 \qquad \text{for} |x| > \frac{1}{2}
$$

The spatial fourier decomposition of $\chi^{(2)}(z)$ contains terms which contribute to different phase matching processes. With the grating vectors defined as $\beta_{\Lambda 1,2} \equiv \frac{2\pi}{\Lambda_{1,2}}$, we can write

$$
\chi^{(2)}(z) = \left(\frac{N_1\Lambda_1}{N_1\Lambda_1 + N_2\Lambda_2} + \right.
$$

$$
\sum_{m=1}^{m=\infty} \frac{1}{m\pi}\left[-1 + \sin\left(\frac{2m\pi N_1\Lambda_1}{N_1\Lambda_1 + N_2\Lambda_2}\right)\right]\cos\left(\frac{2\pi m z}{N_1\Lambda_1 + N_2\Lambda_2}\right) +
$$

$$
\sum_{m=1}^{m=\infty} \frac{1}{m\pi}\left[1 - \cos\left(\frac{2m\pi N_1\Lambda_1}{N_1\Lambda_1 + N_2\Lambda_2}\right)\right]\sin\left(\frac{2\pi m z}{N_1\Lambda_1 + N_2\Lambda_2}\right)\right)
$$

(5.16)

$$
\times \sum_{m=1}^{m=\infty} \frac{2}{m\pi}\left[1 - \cos(m\pi)\right]\sin\left(\frac{2\pi m z}{\Lambda_1}\right) +
$$

$\{$Corresponding terms of Λ_2 process$\}$

In our design the number of domains in the two types of segments are the same, i.e., $N_1 = N_2$. Also the domain separation is very small compared to the domain period, i.e., $\Lambda_1 \approx \Lambda_2$. Under these conditions, we further simplify the terms in

$\chi^{(2)}(z)$ that contribute to Λ_1 processes as follows:

$$\chi^{(2)}(z) \approx \left[\frac{1}{2} + \sum_{m=1}^{m=\infty} \frac{1}{m\pi} \left[1 - \cos(m\pi)\right] \sin\left(\frac{\pi m\,z}{N_1 \Lambda_1}\right) \right]$$
$$\times \sum_{m=1}^{m=\infty} \frac{2}{m\pi} \left[1 - \cos(m\pi)\right] \sin\left(\frac{2\pi m\,z}{\Lambda_1}\right) \tag{5.17}$$

Cosidering the d.c. term and the terms corresponding to $m = 1$ we arrive at,

$$
\begin{aligned}
\chi^{(2)}(z) &\approx \left[\frac{1}{2} + \sum_{m=1}^{m=\infty} \frac{1}{m\pi} \left[1 - \cos(m\pi)\right] \sin\left(\frac{\pi m\,z}{N_1 \Lambda_1}\right) \right] \\
&\quad \times \sum_{m=1}^{m=\infty} \frac{2}{m\pi} \left[1 - \cos(m\pi)\right] \sin\left(\frac{2\pi m\,z}{\Lambda_1}\right) \\
&= \frac{2}{\pi} \sin\left(\frac{2\pi z}{\Lambda_1}\right) + \frac{4}{\pi^2} \sin\left(\frac{\pi z}{N_1 \Lambda_1}\right) \sin\left(\frac{2\pi z}{\Lambda_1}\right) + (m > 1 \text{ terms}) \\
&= \frac{1}{\pi} e^{-i\beta_{\Lambda 1} z} + \frac{2}{\pi^2} e^{-i(1\pm\frac{1}{N_1})\beta_{\Lambda 1} z} + (m > 1 \text{ terms}) - c.c.
\end{aligned}
\tag{5.18}
$$

In the above equations, c.c. represents complex conjugate. The first term in the equation represents the phase matching of the center peak. Note that in this case the grating vector is $\beta_{\Lambda 1}$. The second term represents the phase matching due to the two satellites located immediately above and below the main peak phase matched by Λ_1. They have the grating vectors $\beta_{\Lambda 1}(1 + \frac{1}{N})$ and $\beta_{\Lambda 1}(1 - \frac{1}{N})$. The Fourier amplitude of the satellite peaks is $\frac{2}{\pi}$ smaller than the main peak. The satellite peaks still further away from the main peaks have the grating vectors $\beta_m = (1 \pm \frac{m}{N_1})\beta_{\Lambda 1}$ and Fourier amplitudes $\frac{2}{m\pi}$, where $m \geq 2$. Similarly, the grating vectors $\beta_{\Lambda 2}(1 \pm \frac{1}{N_2})$ correspond to the satellites immediately above and below the center peak phase matched by Λ_2. The satellites further away have the grating vectors $(1 \pm \frac{m}{N_2})\beta_{\Lambda 2}$. Note that in the final step of Eq. 5.18, the exponentials corresponding to $e^{i(1\pm\frac{m}{N_1})\beta_{\Lambda 1} z}$ are neglected. This is because the corresponding phase matching processes are not in the wavelength range of interest.

Second Harmonic Generation

The measured SH phase matching spectrum of a waveguide with 100 domain periods per segment is shown in Fig. 5.7(a). The set-up used to measure the SH is shown in Fig. 4.3. The location of the satellite peaks relative to the main peak is correctly predicted by the calculations. The Fig. 5.7(b) shows the peak at 1556.25 nm in more detail. The measured full width at half maximum is 145 pm, which agrees with the calculated value. The measured SH conversion efficiency is $\approx 2.5 \frac{\%}{W}$.

SH generated in waveguides with segments $N_1 = N_2 = 3000$, $N_1 = N_2 = 500$ and $N_1 = N_2 = 10$ are also investigated. The results are summarized in Fig. 5.7(c), Fig. 5.7(d) and Fig. 5.7(e) respectively. The experimental results agree with calcu-
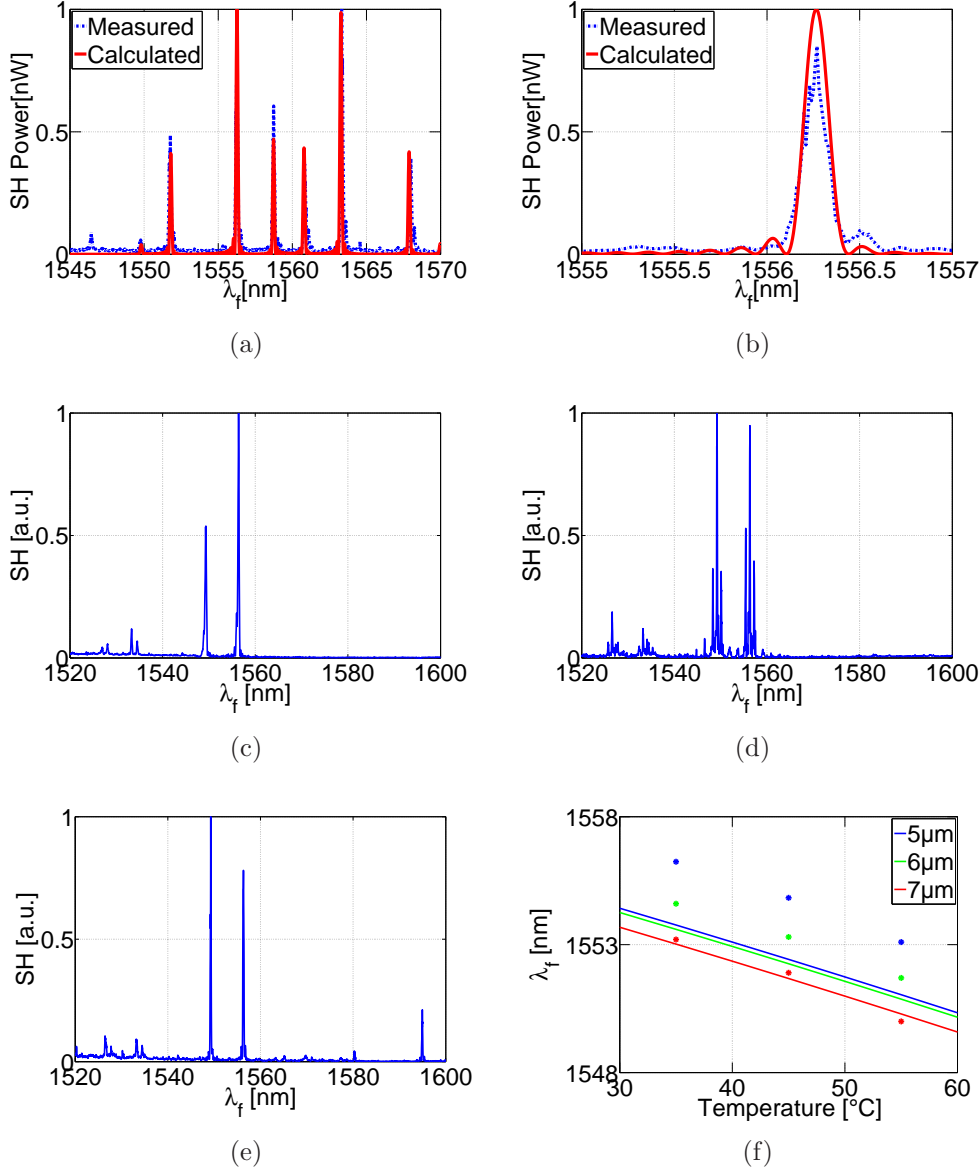
Figure 5.7: (a) SH phase matching characteristic with $N_1 = N_2 = 100$. Measured SH efficiency is 2.5 $\frac{\%}{W}$. (b) The peak at $\lambda = 1556.25$ nm in more detail. The measured FWHM is $\Delta\lambda = 145$ pm.(c) SH phase matching characteristic with $N_1 = N_2 = 3000$. Peaks at $\lambda_1 = 1549.3$ nm and $\lambda_2 = 1556.3$ nm correspond to $\Lambda_1 = 9.02\,\mu m$ and $\Lambda_2 = 9.07\,\mu m$. (d) SH phase matching characteristic with $N_1 = N_2 = 500$. Satellite peaks appear ≈ 1 nm above and below the center peaks. Location of the center peaks remain unchanged. Temperature $= 35°C$, Width $= 7\,\mu m$. (e) SH phase matching characteristic with $N_1 = N_2 = 10$. Satellite peaks are pushed away from the range of interest. One of the main satellite peak in this case is at $\lambda = 1595$ nm. The two distinct peaks between $\lambda = 1520$ nm and $\lambda = 1540$ nm (in Figs. (c) to (d)) are due to higher order modes of the pump phase matched.(d) Calculated (solid lines) and measured (*) temperature tuning characteristics of SH. The slope of the calculated curve is $-125\,\frac{pm}{°C}$. The domain period, $\Lambda_1 = 9.07\,\mu m$.

lated results explained in the previous section. The temperature tuning characteristic of SH phase matching is calculated and compared with experiments(Fig. 5.7(f)).

The slope of temperature tuning curve is -125 $\frac{\text{pm}}{°\text{C}}$. There is an offset of 4 nm between the location of the measured and calculated phase matching peaks. However, the calculated and measured slopes are roughly the same.

Spontaneous Parametric Down Conversion

The set up used to measure spontaneous parametric down conversion from the interlaced structure is shown in Fig. 4.7. The experiment helps to identify the operating point of entanglement. A waveguide with 10 domain periods per segment is characterized. With 10 domain periods per segment, the satellite peaks are pushed ≈ 70 nm away from the main peaks. This way, the possibility of the spurious down conversion resulting from the satellites is completely eliminated. The down conversion experiments are done with the sample stabilized to temperatures above 150 °C. The high temperature is preferred because the photo-refractive damage can be eliminated. The measured spectra is shown in Fig. 5.8. The pump wavelength used for these measurements is 778.2 nm. After fixing the pump wavelength, the temperature of the waveguide is tuned to find the correct operating point of entanglement. The four peaks in the figure correspond to the measurement at a temperature of 172.5 °C. The correct operating point is achieved at temperature of 172 °C. The TE peaks of both processes are stronger than the TM peaks because of the smaller losses in the waveguide and in the monochromator.
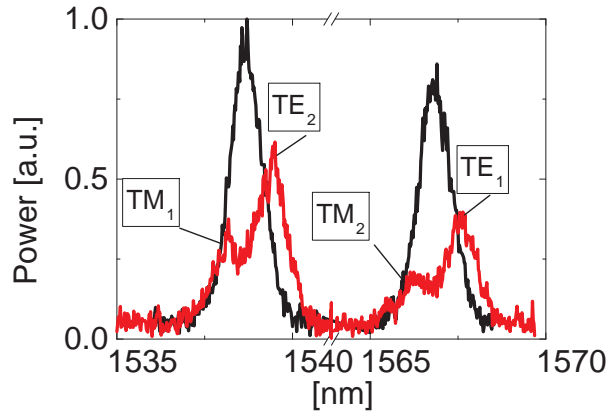
Figure 5.8: The measured spectra of down conversion. The four peaks in the figure correspond to the measurement at a temperature of 172.5 °C (red). The correct operating point is achieved at temperature of 172 °C (blue).

The temperature tuning characteristics of down conversion is shown in Fig. 5.9. The pump wavelength for these measurements is $\lambda_\text{p} = 777.47$ nm. The operating point in this case is reached at temperature ≈ 163.9 °C. Since the emission bandwidth is ≈ 0.5 nm, and the slope of temperature tuning is $\partial_\text{T}\lambda = 0.6 \frac{\text{nm}}{°\text{C}}$, a change in temperature by 0.4 °C will remove the spectral overlap achieved. The temperature of the sample in our experiments is stabilized to within ± 0.1 °C. More critical is the stability of the pump wavelength. Since the slope of pump wave-
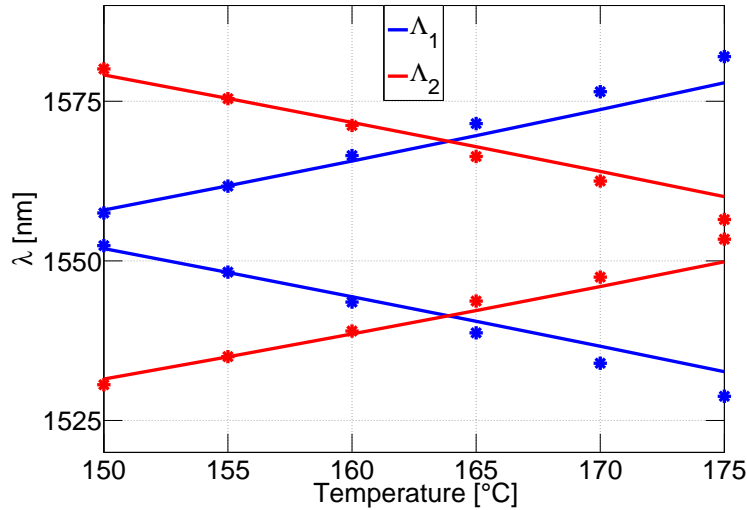
Figure 5.9: The temperature tuning characteristics of down conversion. The pump wavelength for these measurements is $\lambda_{\mathrm{p}} = 777.47$ nm. The operating point in this case is reached at temperature $\approx 163.9\,^{\circ}\mathrm{C}$.

length tuning is $\partial_{\lambda_{\mathrm{P}}} \lambda_{\mathrm{TM}} = -5$ and $\partial_{\lambda_{\mathrm{P}}} \lambda_{\mathrm{TE}} = 10$, a change in pump wavelength by ≈ 33 pm will remove the spectral overlap.

5.3   Demonstration of Polarization Entanglement

Generation of polarization entangled states is investigated by an interference experiment. The experiment measures characteristic quantum interference in the correlated counts of two single photon detectors. The schematic of the characterization is shown in Fig. 5.10.
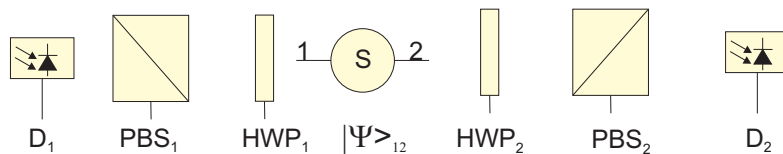
Figure 5.10: Schematic of the interference set-up to investigate polarization entanglement. S:Source, HWP:Half Wave Plate, PBS: Polarization Beam Splitter, D: Single Photon Detector

The source S generates the polarization entangled state $|\psi\rangle_{12}$. The subscripts 1 and 2 indicate the two output ports of the source. The half wave plates (HWP_1 and HWP_2) inserted in the output arms rotate the linear polarization states of the photons at the output ports 1 and 2 respectively. Polarization Beam Splitters (PBS_1 and PBS_2) inserted behind the half wave plates act as polarizers by allowing only the horizontally polarized photons to pass to the detectors 1 and 2. The experiment is done by fixing the orientation of the half wave plate in one arm and rotating the half wave plate in the other arm. The correlated counts in the two detectors are measured as a function of the rotation of the half wave plate.

72

If the photons are entangled, the coincident counts show an interference pattern. The visibility of the interference is a metric of the quality of entanglement.

In order to understand the nature of the interference we look at the joint state of the photons behind the half wave plates. The half wave plate with the fast axis oriented at an angle θ_1 with respect to the horizontal axis reflects the linear polarization of the input field along its axis. The Jones matrix for the half wave plate is

$$\hat{J}_1(\theta_1) = \begin{bmatrix} \cos(2\theta_1) & \sin(2\theta_1) \\ \sin(2\theta_1) & -\cos(2\theta_1) \end{bmatrix}$$

The vector representation for the single photon states $|H\rangle_1$ and $|V\rangle_1$ are

$$|H\rangle_1 = \begin{bmatrix} 1 \\ 0 \end{bmatrix} \qquad\qquad |V\rangle_1 = \begin{bmatrix} 0 \\ 1 \end{bmatrix}$$

The single photon state of the TE mode ($|H\rangle_1$) is transformed by the halfwave plate into a single photon state of a mode with a polarization at an angle 2θ with respect to the H axis. The transformed states $|H'\rangle_1$ and $|V'\rangle_1$ in the $\{|H\rangle, |V\rangle\}$ basis are given by

$$
\begin{aligned}
|H'\rangle_1 &= \hat{J}_1 |H\rangle_1 & |V'\rangle_1 &= \hat{J}_1 |V\rangle_1 \\
&= \begin{bmatrix} \cos(2\theta_1) & \sin(2\theta_1) \\ \sin(2\theta_1) & -\cos(2\theta_1) \end{bmatrix} \begin{bmatrix} 1 \\ 0 \end{bmatrix} & &= \begin{bmatrix} \cos(2\theta_1) & \sin(2\theta_1) \\ \sin(2\theta_1) & -\cos(2\theta_1) \end{bmatrix} \begin{bmatrix} 0 \\ 1 \end{bmatrix} \\
&= \begin{bmatrix} \cos(2\theta_1) \\ \sin(2\theta_1) \end{bmatrix} & &= \begin{bmatrix} \sin(2\theta_1) \\ -\cos(2\theta_1) \end{bmatrix} \\
|H'\rangle_1 &= \cos(2\theta_1)|H\rangle_1 + \sin(2\theta_1)|V\rangle_1 & |V'\rangle_1 &= \sin(2\theta_1)|H\rangle_1 - \cos(2\theta_1)|V\rangle_1
\end{aligned}
$$

Similarly, the transformed states $|H'\rangle_2$ and $|V'\rangle_2$ in the $\{|H\rangle, |V\rangle\}$ basis are given by

$$
\begin{aligned}
|H'\rangle_2 &= \cos(2\theta_2)|H\rangle_2 + \sin(2\theta_2)|V\rangle_2 \\
|V'\rangle_2 &= \sin(2\theta_2)|H\rangle_2 - \cos(2\theta_2)|V\rangle_2\,.
\end{aligned}
$$

The angle θ_2 is the rotation of the fast axis of the halfwave plate in arm 2.

The joint two photon state $|\psi\rangle_{12}$ behind the source is transformed by the half wave plates into the state $|\phi\rangle_{12}$. The orthogonal bases for the two photon state are $|H\rangle_1 |H\rangle_2$, $|H\rangle_1 |V\rangle_2$, $|V\rangle_1 |H\rangle_2$ and $|V\rangle_1 |V\rangle_2$. The state $|\phi\rangle_{12}$ is written as a superposition of the two photon basis states.

$$
\begin{aligned}
|\phi\rangle_{12} = & \left[\cos 2\theta_1 \sin 2\theta_2 + e^{i\delta} \sin 2\theta_1 \cos 2\theta_2\right] |H\rangle_1 |H\rangle_2 - \\
& \left[\sin 2\theta_1 \cos 2\theta_2 + e^{i\delta} \cos 2\theta_1 \sin 2\theta_2\right] |V\rangle_1 |V\rangle_2 - \\
& \left[\cos 2\theta_1 \cos 2\theta_2 - e^{i\delta} \sin 2\theta_1 \sin 2\theta_2\right] |H\rangle_1 |V\rangle_2 + \\
& \left[\sin 2\theta_1 \sin 2\theta_2 - e^{i\delta} \cos 2\theta_1 \cos 2\theta_2\right] |V\rangle_1 |H\rangle_2 +
\end{aligned}
$$

Only the term corresponding to the basis state $|H\rangle_1 |H\rangle_2$ contributes to coincident counts. The exponent, $e^{i\delta}$, accounts for the phase shifts between $|H\rangle_1$ and $|V\rangle_1$ in arm 1, and $|H\rangle_2$ and $|V\rangle_2$ in arm 2. The polarization beam splitters behind the half wave plates only allow the horizontally polarized fields to be transmitted. The coincident count rate as a function of the orientation of the half wave plates, $R_c(\theta_1, \theta_2)$, is given by

$$
\begin{aligned}
R_c(\theta_1, \theta_2) &= |_1\langle H|_2 \langle H| \, |\psi\rangle_{12}|^2 \\
&= |\left[\cos 2\theta_1 \sin 2\theta_2 + e^{i\delta} \sin 2\theta_1 \cos 2\theta_2 \right]|^2
\end{aligned}
\tag{5.24}
$$

If we keep the angle θ_1 fixed and rotate the angle θ_2 of the half wave plate, the coincident count rate oscillates with a periodicity of 90°. The visibility of interference pattern depends on the phase δ. The visibility is maximum when $\delta = \{0, \pi\}$. In this case, the count rates in the detectors remain constant, independent of the orientation of the half wave plates.
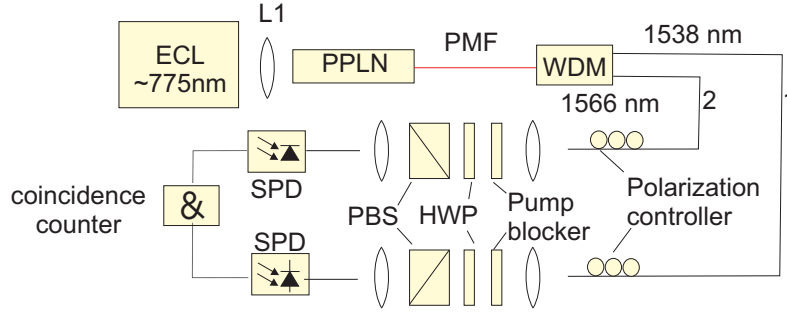
Figure 5.11: Setup used to characterize polarization entanglement.

The setup used to measure the interference pattern is shown in Fig. 5.11. Light from ECL (λ_p =778.2 nm) is used as the pump. The light is coupled into the waveguide using the lens L_1 which is anti-reflection coated. The temperature of the sample is kept at 172°C to reach the correct operating point. The down converted field is coupled out using a polarization maintaining fiber. The orientation and the length of the fiber compensates for the group velocity mismatch between the TE and TM photons. The down converted photons are then separated depending on their wavelengths using a wavelength division de-multiplexer. The joint state of the photons at the two output ports is the entangled state $|\psi\rangle_{12}$. The entangled state is analyzed using the interference set up consisting of the two half wave plates and two polarization beam splitters. Coincident counts are measured as a function of the orientation of the half wave plate 2 at two different orientations of the half wave plate 1. The polarization of the photon states are defined by the fiber polarization controllers. The measured interference pattern is shown in the Fig. 5.12.

The visibility of the interference pattern is 70%. When the orientation of the half wave plate 1, θ_1=22.5°, the coincidence count is maximum with the orientation of half wave plate 2, θ_2= 67.5°. The measurement is said to be in the non-trivial basis because the interference pattern can result only from the entangled state $|\psi\rangle_{12}$. Similarly, when $\theta_1 = 67.5$ °, the coincident counts reach a minimum with the orientation, $\theta_2 \approx 67.5$ °.
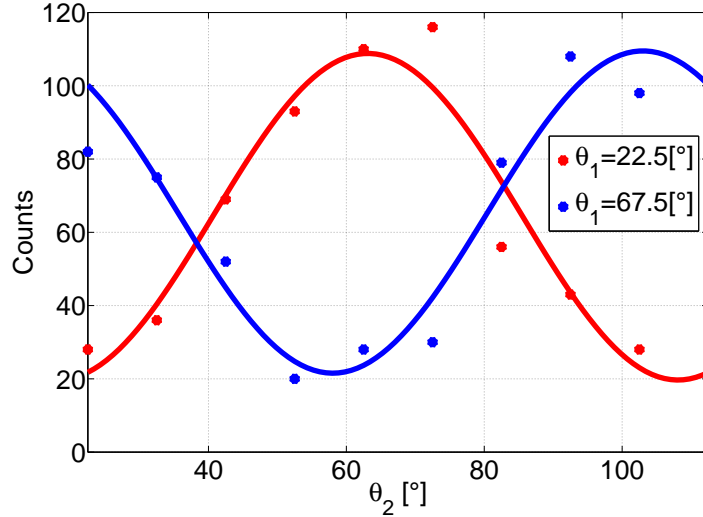
Figure 5.12: Interference in the coincidence counts seen when rotating the half-wave plate in Arm 2 while keeping the orientation of the half-wave plate in Arm 1 is fixed. The visibility of the interference pattern is ≈ 70 %.

The coincident count rate as a function of the arrival time difference of the photons at the two detectors is shown in Fig. 5.13(a). The measurement corresponds to the peak in the interference pattern with the half wave plate orientations $\theta_1 = 22.5°$ and $\theta_2 = 67.5°$. The Fig. 5.13(a) shows the counts in the two detectors as a function of θ_2. As predicted the counts in each detector remain constant irrespective of θ_2.

(a)

(b)
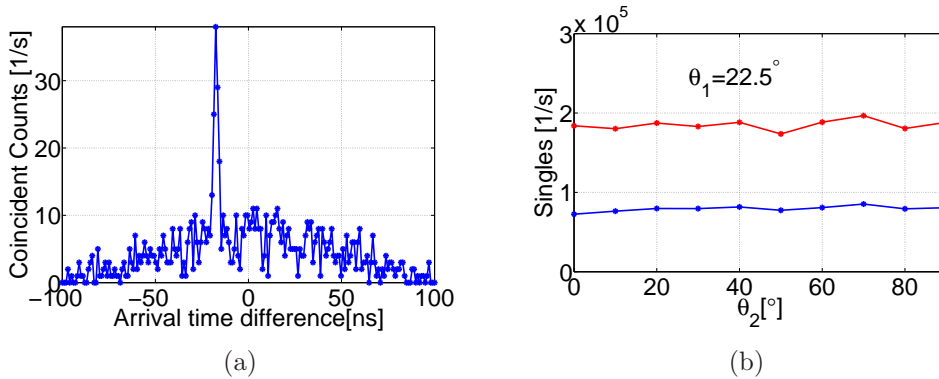
Figure 5.13: (a) The coincident count rate as a function of the arrival time difference of the photons at the two detectors when half wave plate orientations are $\theta_1 = 22.5°$ and $\theta_2 = 67.5°$. (b) The single counts measured by the two detectors when $\theta_1 = 22.5°$ and θ_2 is varied.

The count rate in the detectors $(S_{1,2})$ depend on the out-coupling efficiency, the transmission through the different components, $(\mu_{1,2})$, and the detector efficiencies. In order to estimate the out-coupling efficiency, we use the method by Klyshko [57], already explained in Chapter 3. The transmission through the arm 1, measured from the input port of the wavelength division de-multiplexer until the detector 1 is ≈ -7 dB. Similarly, transmission through the arm 2 is ≈-5 dB. The

detection efficiencies of both the detectors were set to 15 %. The count rates (over a duration of 1 s) are modelled as follows.

$$S_1 = \mu_1 \, \eta_1 \, N + D_1 \qquad\qquad S_1 \approx 184 \times 10^3, \; \eta_1 = 15\%, \; D_1 \approx 80 \times 10^3$$
$$S_2 = \mu_2 \, \eta_2 \, N + D_2 \qquad\qquad S_2 \approx 73 \times 10^3, \; \eta_2 = 15\%, \; D_2 \approx 40 \times 10^3$$
$$R = \mu_1 \, \mu_2 \, \eta_1 \, \eta_2 \, N \qquad\qquad R \approx 100$$
$$\Rightarrow N = \frac{(S_1 - D_1)\,(S_2 - D_2)}{R}$$
$$= 33 \times 10^6$$
$$\Rightarrow \mu_1 = \frac{S_1 - D_1}{\eta_1 \, N} \qquad\qquad \mu_2 = \frac{S_2 - D_2}{\eta_2 \, N}$$
$$= 5\% \qquad\qquad\qquad = 2\%$$

$\mu_{1,2}$ estimated in the above equations include both the out-coupling efficiency and the transmission loss. After correcting for the transmission loss, the fiber coupling efficiency, $\mu_1 = 17\,\%$ (at $\lambda = 1538$ nm) and $\mu_2 = 11\,\%$ (at $\lambda = 1566$ nm). Since the coupling estimated from the coincidence measurement is smaller than expected, a second method was used to estimate the coupling efficiency. By using a lens behind the sample and monitoring the transmitted power, and later normalizing the transmission through the out-coupling fiber to this value, we estimated a coupling efficiency of $\approx 70\,\%$. The difference in the two estimates points to excess counts in atleast one of the detectors by a spurious process. The spurious counts in the detector will reduce the correlated coincident events.

There are various possible reasons behind the reduction in the visibility. The possible slight offset of the pump wavelength or temperature from the exact operating point results in a reduction of the indistinguishability. The in-exact compensation of the group velocity difference is another possible reason. A drift in the polarization also leads to reduced visibility. A comprehensive model to study the visibility follows.

The model for coincident counts resulting in Eq. 5.24 igonores the finite emission bandwidth of the photon pairs. In order to explain reduction in visibility due to the reasons mentioned, we have to include the finite emission bandwidth of the photon pairs into the model. The distribution of photon coincidence counting rate (see Fig. 5.10) is proportional to $g(t_1,t_2)$ defined as follows [58; 59]:

$$g(t_1, t_2) \equiv \langle E_1^{(+)}(t_1) E_2^{(+)}(t_2) E_1^{(-)}(t_1) E_2^{(-)}(t_2) \rangle$$
$$= |E_1^{(-)}(t_1) E_2^{(-)}(t_2) \, |\psi\rangle_{12}|^2, \tag{5.26}$$

where t_1 and t_2 are the arrival times of the photons at detectors 1 and 2 respectively. $E_{1,2}^{(\pm)}$ are the operators representing positive or negative frequency amplitudes of the electric fields at ports 1 or 2. Note that we are concerned only with the operators representing TE polarized fields. This is because the polarization beam splitters are oriented in such a way that only TE polarized fields are allowed into the detector. However, the presence of half-wave plates implies that the operators $E_1^{(\pm)}$ have contributions from both TE and TM polarized normal modes of the

waveguide at frequencies centered around ω_1. Similarly, operator $E_2^{(\pm)}$ have contributions from both TE and TM polarized normal modes at frequencies centered around ω_2.

To proceed further, we focus on the complex field operators behind the two half-wave plates. The Jones matrices J_1 and J_2 of the half-wave plates, in the quantum picture, are the transformation matrices for the field operators. In other words,

$$
\begin{aligned}
E_1^{(+)} &= \cos(2\theta_1)\, A_{\mathrm{TE}}^{(+)} + \sin(2\theta_1)\, A_{\mathrm{TM}}^{(+)} \quad \text{and} \\
E_2^{(+)} &= \cos(2\theta_2)\, B_{\mathrm{TE}}^{(+)} + \sin(2\theta_2)\, B_{\mathrm{TM}}^{(+)}.
\end{aligned}
\tag{5.27}
$$

$A_{\mathrm{TE,TM}}$ are the field operators representing TE and TM polarized fields in front of the half-wave plate in arm 1. Similarly, $B_{\mathrm{TE,TM}}$ are the field operators representing TE and TM polarized fields in front of the half-wave plate in arm 2. In terms of annihilation operators, the field operators are represented as follows.

$$
\begin{aligned}
A_{\mathrm{TE,TM}}^{(+)}(t) &= \int d\omega\, a_{\mathrm{TE,TM}}(\omega)\, e^{-i\omega t} \\
B_{\mathrm{TE,TM}}^{(+)}(t) &= \int d\omega\, b_{\mathrm{TE,TM}}(\omega)\, e^{-i\omega t}
\end{aligned}
\tag{5.28}
$$

$a_{\mathrm{TE,TM}}$ are the annihilation operators associated with TE and TM polarized normal modes in front of the half-wave plate in arm 1. Similarly, $b_{\mathrm{TE,TM}}$ are the annihilation operators associated with TE and TM polarized normal modes in front of the half-wave plate in arm 2. Note that a normal mode is defined as a field distribution in time and space with a unique propagation constant and frequency. The entangled state behind the source (including the wavelength division multiplexer) is given by

$$
|\psi\rangle_{12} \approx \underbrace{\tilde{f}(\omega, \omega_{\mathrm{p}} - \omega)\, |\mathrm{TE}, \omega\rangle_1 |\mathrm{TM}, \omega_{\mathrm{p}} - \omega\rangle_2}_{\Lambda_1\ \text{process}} +
$$
$$
\underbrace{\tilde{f}(\omega', \omega_{\mathrm{p}} - \omega')\, |\mathrm{TM}, \omega_{\mathrm{p}} - \omega'\rangle_1 |\mathrm{TE}, \omega'\rangle_2}_{\Lambda_2\ \text{process}}
\tag{5.29}
$$

The state $|\mathrm{TE}, \omega\rangle$ is a single photon state associated with a TE normal mode at frequency ω. Similarly, $|\mathrm{TM}, \omega\rangle$ is a single photon state associated with a TM normal mode at frequency ω. Unlike the entangled state represented by Eq. 5.2, the above equation takes into consideration the emission spectrum through the joint state function $\tilde{f}(\omega, \omega_{\mathrm{p}} - \omega)$. The derivation of the joint state function is summarized in Appendix B. The generated state can be represented only approximately as the sum of two joint photon states. The reason is we are ignoring the Bose-Einstein distribution over the number states. The motivation for this approximation is also explained in Appendix B. The joint state function is normalized in such a way that $_{12}\langle\psi|\psi\rangle_{12} = 1$. Note that the two terms of $|\psi\rangle_{12}$ represent two independent down conversion processes.

The distribution obtained after substituting Eq. 5.27 and Eq. 5.28 in Eq. 5.26

follows:

$$
\begin{aligned}
g(t_1, t_2) &= |E_1^{(+)}(t_1) E_2^{(+)}(t_2) |\psi\rangle_{12}|^2 \\
&= |[\cos(2\theta_1)\, A_{TE}^{(+)} + \sin(2\theta_1)\, A_{TM}^{(+)}][\cos(2\theta_2)\, B_{TE}^{(+)} + \sin(2\theta_2)\, B_{TM}^{(+)}] |\psi\rangle_{12}|^2 \\
&= |[\cos(2\theta_1)\sin(2\theta_2)\, A_{TE}^{(+)} B_{TM}^{(+)} + \cos(2\theta_2)\sin(2\theta_1)\, B_{TE}^{(+)} A_{TM}^{(+)}] |\psi\rangle_{12}|^2
\end{aligned}
$$

$$(5.30)$$

Among the four possible cross-terms, only two, corresponding to the arrival of orthogonally polarized generated photons at the two detectors, are retained. In order to simplify notations, we introduce $T_1 = \cos(2\theta_1)\sin(2\theta_2)$ and $T_2 = \cos(2\theta_2)\sin(2\theta_1)$. The expression for $g(t_1,t_2)$ is further simplified by substituting Eq. 5.29 into Eq. 5.30.

$$
g(t_1, t_2) =
$$

$$
|T_1 \int d\omega\, \tilde{f}(\omega)\, e^{-i\omega t_1 - i(\omega_p - \omega)t_2}\, a_{TE}(\omega)\, b_{TM}(\omega_p - \omega)\, |TE, \omega\rangle_1\, |TM, \omega_p - \omega\rangle_2 +
$$

$$
T_2 \int d\omega'\, \tilde{f}(\omega')\, e^{-i\omega' t_2 - i(\omega_p - \omega')t_1}\, a_{TM}(\omega_p - \omega')\, b_{TE}(\omega')\, |TM, \omega_p - \omega'\rangle_1\, |TE, \omega'\rangle_2|^2
$$

$$
= \left| T_1\, e^{-i\omega_p t_2} \int d\omega\, \tilde{f}(\omega)\, e^{-i\omega(t_1 - t_2)} + T_2\, e^{-i\omega_p t_1} \int d\omega'\, \tilde{f}(\omega')\, e^{i\omega'(t_1 - t_2)} \right|^2
$$

$$
= |T_1\, e^{-i\omega_p t_2}\, e^{-i\omega_0(t_1 - t_2)} \underbrace{\int d\delta\omega\, \tilde{f}(\delta\omega)\, e^{-i\delta\omega(t_1 - t_2)}}_{\text{I.F.T of } f(\delta\omega)} +
$$

$$
T_2\, e^{-i\omega_p t_1}\, e^{i\omega_0'(t_1 - t_2)} \underbrace{\int d\delta\omega'\, \tilde{f}(\delta\omega)\, e^{i\delta\omega'(t_1 - t_2)}}_{\text{I.F.T of } f(-\delta\omega)} |^2
$$

$$
= |\, T_1\, e^{-i\omega_p t_2}\, e^{-i\omega_0(t_1 - t_2)}\, f(t_1 - t_2) + T_2\, e^{-i\omega_p t_1}\, e^{i\omega_0'(t_1 - t_2)}\, f(t_2 - t_1)\, |^2
$$

$$
= T_1^2 \times \underbrace{|f(\tau)|^2}_{\Lambda_1 \text{process}} + T_2^2 \times \underbrace{|f(-\tau)|^2}_{\Lambda_2 \text{ process}} +
$$

$$
\underbrace{T_1 T_2 \times f(\tau)\, f^*(-\tau)\, e^{i[\omega_p - \omega_0 - \omega_0']\tau} + T_1 T_2 \times f^*(\tau)\, f(-\tau)\, e^{-i[\omega_p - \omega_0 - \omega_0']\tau}}_{\text{quantum interference}}
$$

$$(5.31)$$

The time τ is the arrival time difference defined as $\tau \equiv t_1 - t_2$. The functional form of $g(t_1,t_2)$ is similar to the result worked out by Sergienko [60] for an entangled source based on type II down conversion. The function $g(t_1,t_2)$ has contributions from four terms. The first term represents the contribution to the coincidence counts from the first process, and the second term represents the contribution from the second process. Note that the second term contains $|f(-\tau)|^2$, which is a time reversed version of $|f(\tau)|^2$ present in the first term. This is because the photons contributing to the coincident events by the first process arrive at the detector 1 after the arrival of the corresponding twin (TM photon) at the detector 2. However, the the photons contributing to the coincident events by the second process arrive at the detector 1 before the arrival of the corresponding twin (TE photon) at the detector 2.

The last two terms arise because of the interference in the probability amplitudes corresponding to the contributions from the two processes. The interference term contains frequency ω_0 (ω_0'), which is the exactly phase matched emission frequency of the TE field of the first (second) process. At the correct operating point, $\omega_0' = \omega_p - \omega_0$. The function $f(\tau)$ is the inverse Fourier transform of the joint state function $\tilde{f}(\delta\omega, -\delta\omega)$, where $\delta\omega$ is the offset from ω_0. The functional forms of $\tilde{f}$ and f are given below. For details refer Appendix B and Appendix C.

$$
\begin{aligned}
\tilde{f} &= \kappa_p A_p L \, sinc\left[\left(\frac{L}{2V_{TE}} - \frac{L}{2V_{TM}}\right)\delta\omega\right] \, e^{i\left(\frac{L}{2V_{TE}} - \frac{L}{2V_{TM}}\right)\delta\omega} \\
f(\tau) &= \frac{\kappa A_p L}{\tau_g} \, rect\left[\frac{\tau - \tau_g}{2\tau_g}\right]
\end{aligned}
\tag{5.32}
$$

where $\tau_g = \left(\frac{L}{2V_{TE}} - \frac{L}{2V_{TM}}\right)$. The time τ_g is the average arrival time difference between the photons in the TE and TM modes. Now we consider the factors affecting the visibility in detail.

Group Velocity Delay

As already mentioned, because of the group velocity difference the TE and TM photons reach the detectors at different times. A polarization maintaining fiber with proper orientation is used for compensating the arrival time difference. However, an in-exact compensation because of in-correct orientation or length of the fiber may reduce the visibility. More formally, the different cases are summarized as follows:

$$
\begin{aligned}
\int d\tau \, f(\tau) \times f(-\tau) &= 0 & \text{un-compensated} \\
f(\tau) &= f(-\tau) & \text{exact compensation} \\
\int d\tau \, f(\tau) \times f(-\tau) &< \int d\tau \, f(\tau) \times f(\tau) & \text{in-exact compensation}
\end{aligned}
$$

These concepts are illustrated in Fig. 5.14.

To estimate the visibility, we substitute the functional form of $f(\tau)$ shown in Eq. 5.32 into Eq. 5.31. We arrive at the following expression for $g(\tau)$:

$$
\begin{aligned}
g(\tau) = \; &T_1^2 \, |f(\tau)|^2 + T_2^2 \, |f(-\tau)|^2 + \\
&T_1 T_2 \, f(\tau) f^*(-\tau) + T_1 T_2 \, f^*(\tau) f(-\tau)
\end{aligned}
\tag{5.34}
$$

In-order to calculate the coincidence count rate R_c, we integrate $g(\tau)$ over the time limits set by the resolution of the measurement scheme. For all practical purposes, the time limits can be taken as $\tau = -\infty$ to $\tau = \infty$. The resolution of the measurement scheme is of the order of ns, while the width of the function
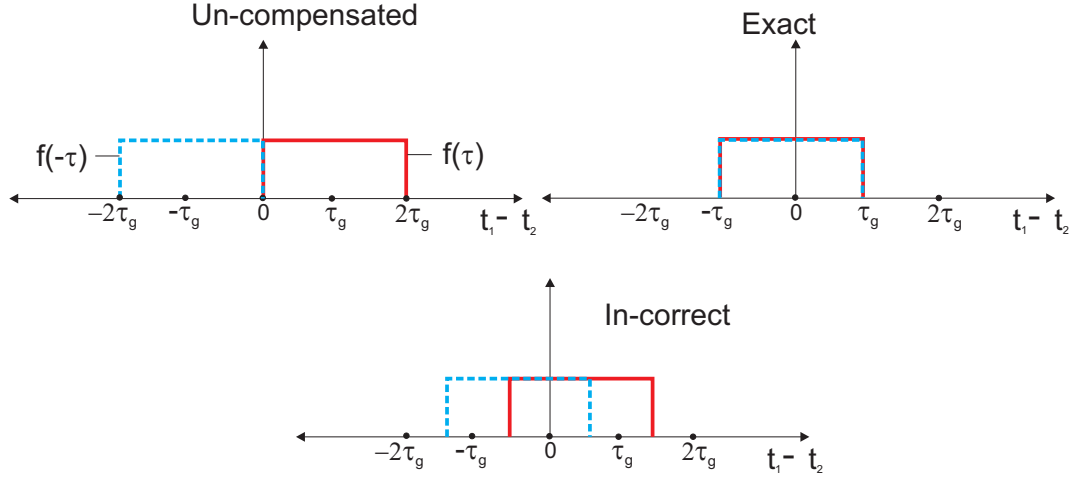
Figure 5.14: The function f plotted as a function of the arrival time difference. When the arrival time difference is un-compensated, there is no overlap between $f(\tau)$ and $f(-\tau)$. With exact compensation $f(v) = f(-\tau)$, the overlap is maximum. When the compensation is in-exact the overlap is reduced.
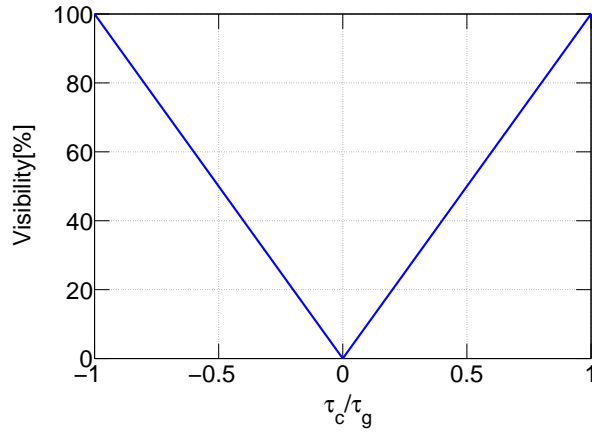
Figure 5.15: Visibility as a function of group velocity delay compensation. $\tau_g \approx 12$ ps is the average arrival time difference between the TE and TM photons defined by Eq. 5.32. τ_c is the duration over which the functions $f(\tau)$ and $f(-\tau)$ overlap.

$|f(\tau)|^2$ is of the order of a few ps. The result is shown below.

$$
\begin{aligned}
R_c(\theta_1, \theta_2) &= \int_{-\infty}^{\infty} d\tau \, g(\tau) \\
&\sim 2\tau_g(T_1^2 + T_2^2) + 2T_1T_2\tau_c
\end{aligned}
\tag{5.35}
$$

The time τ_c is the duration over which the distributions $f(\tau)$ and $f(-\tau)$ overlap. The coincident count rate R_c shows a distinct interference pattern when the orientation of one half-wave plate is fixed and the other one is rotated. But the visibility of the interference pattern depends on τ_c. This is shown in Fig. 5.15

80

Pump Wavelength De-Tuning

The pump wavelength has to be maintained at the operating point to achieve perfect spectral overlap between orthogonally polarized emissions of the two down conversion processes. Slight shift of the pump wavelength (even by a few 100 pm) from the operating point will reduce the spectral overlap, since the TE and TM emissions have steep tuning slopes with opposite signs (refer Fig. 5.3(a)). When the pump wavelength is de-tuned from the operating point, $\omega_p \neq \omega_0 + \omega_0'$. Assuming ω_{p0} is the pump wavelength corresponding to the operating point and $\delta\omega_p$ as the offset from the operating point we arrive at,

$$
\begin{aligned}
\omega_p - \omega_0 - \omega_0' &= \omega_{p0} + \delta\omega_p - \omega_{00} - \delta\omega - \omega_{00}' - \delta\omega \\
&= \underbrace{\omega_{p0} - \omega_{00} - \omega_{00}'}_{\equiv 0} + \delta\omega_p - \delta\omega - \delta\omega \\
&= (1 - 2\alpha)\delta\omega_p,
\end{aligned}
\tag{5.36}
$$

where α is the slope of change in TE emission frequency with change in pump frequency, i.e., $\alpha = \partial_{\omega_p}\omega \approx 2.5$. ω_{00} and ω_{00}' are the emission frequencies at the operating point and $\delta\omega$ is the deviation from the emission at operating point. We finally arrive at the coincident count rate R_c (assuming exact compensation for the group delay difference, i.e., $f(\tau)=f(-\tau)$):

$$
\begin{aligned}
R_c(\theta_1, \theta_2) &= \int_{-\infty}^{\infty} d\tau\, g(\tau) \\
&\sim 2\tau_g \left(T_1^2 + T_2^2 + 2T_1T_2\, \text{sinc}[(1 - 2\alpha)\delta\omega_p\tau_g] \right)
\end{aligned}
\tag{5.37}
$$

For a 50 mm long sample, the average arrival time difference is $\tau_g = 6$ ps. The vis-
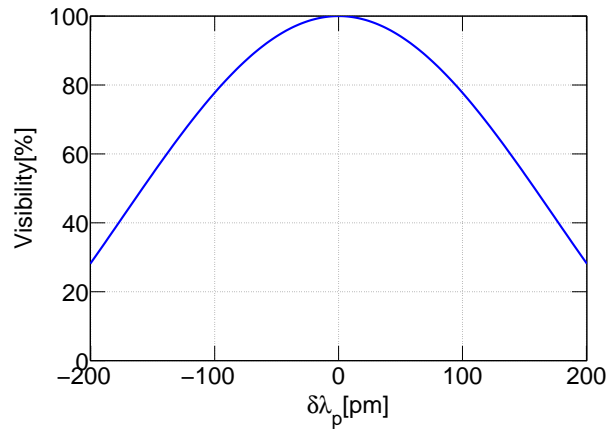
Figure 5.16: Visibility as a function of the de-tuning of pump wavelength from exact operating point.

ibility as a function of the offset from operating point $(\delta\omega_p)$ is shown in Fig. 5.16. The sharp reduction in visibility with the de-tuning of pump wavelength points to the need of stabilizing the pump wavelength. In our experiments the pump wavelength is not stabilized. A shift in the pump wavelength by about 100 pm from

the operating point could explain the visibility of 70 % seen in the experiments.

Temperature De-Tuning

The change in temperature from the exact operating point is another critical factor contributing to reduction in the visibility. The slope of temperature tuning of emission of TE field is $\partial_T \lambda_{TE} \approx -0.6 \frac{nm}{°C}$ and that of TM field is $\partial_T \lambda_{TM} \approx 0.6 \frac{nm}{°C}$. A temperature shift of $\approx 0.5°C$ will completely remove the spectral overlap between the orthogonally polarized emissions of the two processes leading to a loss of entanglement. The waveguide is temperature stabilized to $\pm 0.1°C$. When the temperature is de-tuned from the exact operating point, $\omega_p \neq \omega_0 + \omega_0'$. Assuming ω_{00} and ω_{00}' are the emission wavelengths at the operating point and δT as the offset from the operating point we arrive at

$$
\begin{aligned}
R_c(\theta_1, \theta_2) &= \int_{-\infty}^{\infty} d\tau \, g(\tau) \\
&\sim 2\tau_g \left(T_1^2 + T_2^2 - 2T_1 T_2 \, sinc[2\zeta \, \delta T \, \tau_g] \right)
\end{aligned}
\tag{5.38}
$$

where ζ is the slope of temperature tuning of emission frequency of TE field, i.e., $\zeta \equiv \partial_T \omega \approx -2\pi \times 75 \frac{GHz}{°C}$
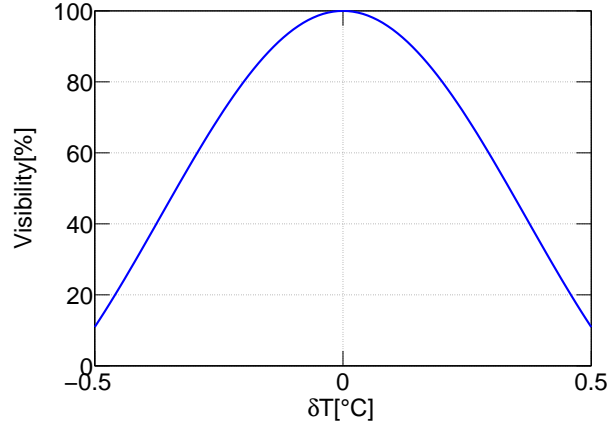
Figure 5.17: Visibility as a function of the de-tuning of temperature from exact operating point.

The visibility as a function of the offset from operating point (δT) is shown in Fig. 5.17.

Polarization Instability

Another important factor affecting the visibility is the stability of polarization in the entanglement characterization setup. Two fiber polarization controllers are used for controlling the polarization. The polarization alignment is done before the visibility measurement. Any drift in polarization during the measurement

will result in a reduction of the visibility. The polarization drift is modelled by introducing an arbitrary phase factor $(\mathrm{e}^{-\mathrm{i}\delta\theta})$ between the two terms in the entangled state $|\psi\rangle_{12}$ (refer Eq. 5.29). With $\delta\theta = 0$, we have a well defined linear polarization in front of the half-wave plate and with $\delta\theta = 90°$, the polarization is circular. Any intermediate value of $\delta\theta$ represents an ellipticaly polarized state. The coincident count rate $\mathrm{R_c}$ in this case is

$$\mathrm{R_c}(\theta_1, \theta_2) = \int_{-\infty}^{\infty} \mathrm{d}\tau \, \mathrm{g}(\tau) \\ \sim 2\tau_\mathrm{g} \left(\mathrm{T}_1^2 + \mathrm{T}_2^2 - 2\mathrm{T}_1\mathrm{T}_2 \cos(\delta\theta) \right) \tag{5.39}$$

The change in visibility with the drift in polarization is shown in Fig. 5.18
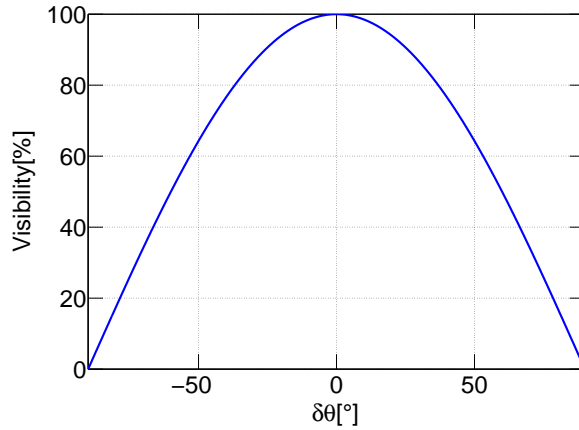
Figure 5.18: Visibility as a function of the polarization drift. With $\delta\theta = 0$, the polarization is linear in front of the halfwave plates. With $\delta\theta = 90°$, the polarization is circular in front of the halfwave plates.

Table 5.1 compares the visibility of other entangled photon pair sources based on type II down conversion.

Table 5.1: Comparison of different entangled photon pair sources.

Reference	Configuration	Visibility [%]
Suhara [55]	Type II 1550 nm	70
Martin [41]	Type II 1310 nm	99
Hasegawa [61]	Type II 1550 nm	82

The visibility of our source matches that of the post-selection free source of Suhara [55]. However, the visibility enhancement expected by the interlaced structure could not be achieved. The most probable reasons for the reduction in the visibility are the offset in the wavelength of the pump or the temperature from the exact operating point and polarization instability during the measurement. A visibility of 99 % is reported by Martin [41] based on type II down conversion at 1310 nm. The delay compensation here is achieved by means of an interferometer set-up. Before measuring the degree of entanglement, a HOM dip experiment is carried out to investigate the indistinguishability of the photons in the two arms.

The experiment helps to compensate for any additional delay between the photons in the two arms casued by the optical fibres in the set-up. Also, the experiment helps to operate the source at the degeneracy point for achieving maximum entanglement. An indistinguishability experiment to achieve the correct operating point of entanglement might result in the enhancement of visibility of our source. Hasegawa [61] has reported visibility of 82% with type II source at 1550 nm. The source is based on a ridge waveguide structure in periodically poled lithium niobate.

Conclusion

A polarization entangled source at non-degeneracy is presented. The source is based on an interlaced domain structure. Design issues as well as experimental results concerning the domain structure is discussed. Before investigating the polarization entanglement, the source is characterized by second harmonic generation (efficiency measured is $\approx 2.5 \frac{\%}{W}$) and spontaneous parametric down conversion (efficiency measured is $\approx 10^{-8} \%$) experiments. Finally, a coincidence measurement with two single photon detectors shows an interference pattern, a characteristic of entanglement, with visibility of $\approx 70\,\%$. A quantum model explaining the visibility measured and ways to improve the visibility are also discussed.

<center>**Chapter 6**</center>

<center># Conclusion</center>

In this thesis, an integrated photon pair source and entangled photon pair source with interlaced structure is demonstrated for the first time, using Titanium indiffused waveguides fabricated in periodically poled LiNbO$_3$. This chapter summarizes the main results obtained and suggests possible extension of the work.

Conclusion

An integrated photon pair source at the telecom wavelength ($\lambda \approx 1550$ nm) is demonstrated (Chapter 4). The source is fully packaged with fiber pigtail at the input side for coupling the pump radiation into a waveguide. The waveguide is realized using Ti in-diffusion in LiNbO$_3$ substrate. A 66 mm long section of the waveguide is periodically poled (with poling periodicity $\Lambda = 9.05\,\mu$m). The pump photons decay into two longer wavelength, orthogonally polarized photons by the non-linear process of spontaneous parametric down conversion. A polarization splitter (realized as a zero-gap coupler) behind the periodically poled section, spatially separates the orthogonally polarized photons. Spurious pump photons (which did not decay) are suppressed by means of a dielectric mirror deposited at the end-face of the waveguide. The spatially separated photons are coupled out of the waveguide using two single mode fibers, pigtailed behind the source.

The fully packaged source is characterized by coincidence measurement using two single photon detectors. The normalized photon pair generation rate of the source is $\sim 10^4 \frac{1}{\text{s·mW·GHz}}$ or $\sim 10^6 \frac{1}{\text{s·mW·nm}}$. The performance of the source can be improved by reducing the waveguide losses. Unfortunately, a relatively high loss waveguide ($\alpha_{\text{TE}} = 0.2\frac{\text{dB}}{\text{cm}}$, $\alpha_{\text{TM}} = 0.25\frac{\text{dB}}{\text{cm}}$) is chosen, because the subsequent polarization splitter has the optimum splitting ratio.

A polarization entangled photon pair source with interlaced domain structure is demonstrated (Chapter 5). The periodically poled waveguide has multiple sections with two different periodicities ($\Lambda_1 = 9.30\,\mu$m and $\Lambda_2 = 9.37\,\mu$m) contributing to two different spontaneous parametric down conversion processes. The operating point of entanglement is defined as the pump wavelength (λ_{p}) and temperature (T) at which the wavelengths of orthogonally polarized emissions of the two processes match. The measured operating point corresponds to a pump wavelength of $\lambda_{\text{p}} = 778.2$ nm and temperature of T = 172°C. The orthogonally polarized emissions from the two processes are at $\lambda_1 = 1538$ nm and $\lambda_2 = 1565$ nm. The entanglement is characterized by an interference experiment. The visibility of the interference pattern measured is $\approx 70\,\%$.

Outlook

The photon pairs generated by spontaneous parametric down conversion have a Bose-Einstein distribution over the joint number states. The photon statistics can be investigated by multi-photon detectors proposed by Silberhorn [62]. The study helps to identify the optimum pump power, above which multi-photon pair generation degrades the performance of the source and below which the photon-pair generation rate is reduced.

The fiber pigtailing of the waveguide reported in Chapter 4 is restricted to low-temperature operation ($<$ 50°C). The pigtailing allowing operation at high temperatures ($>$ 150°C) not only extends the wavelength range but also helps to reduce the photo-refractive damage. Preliminary investigation with *EPO-TEK OG 198-54*, a single component ultra-violet curable adhesive [63], has shown that the fiber pigtailing is stable up to 200 °C.

The waveguides investigated in this thesis are multimode at $\lambda = 775$ nm. The performance of both types of sources can be improved by selectively exciting the fundamental mode at $\lambda =$775 nm. Towards this goal, waveguides with tapers at one end have been fabricated and are currently under investigation.

The use of a polarization splitter for spatial separation can be avoided if the photon pairs generated are counter-propagating. The design issues concerning such a source has been extensively investigated by Silberhorn [64]. The counter propagating down converted field has a very narrow emission bandwidth. Counter-propagating interaction has been achieved in periodically poled KTP crystals [65]. The challenge is to attain poling periodicities of Λ $< 1\,\mu$m in lithium niobate. However, efforts in this direction has been reported [66].

An integrated entangled photon pair source can be realized by replacing the polarization splitter with a polarization insensitive splitter. The polarization insensitive splitter has similar design as that of the polarization splitter but the coupling length and opening angle has to be chosen correctly. The poling period has to be chosen correctly in order to achieve type I or type II down conversion from $\lambda_{\rm p} = 775$ nm to $\lambda = 1550$ nm. With type I down conversion ($\Lambda \approx 16\,\mu$m) the state generated is $|\psi\rangle_{12} = \frac{1}{2}(|{\rm V}\rangle_1 |{\rm V}\rangle_2 + |{\rm H}\rangle_1 |{\rm H}\rangle_2)$ and with type II down conversion ($\Lambda \approx 9\,\mu$m), the state generated is $|\psi\rangle_{12} = \frac{1}{2}(|{\rm H}\rangle_1 |{\rm V}\rangle_2 + |{\rm V}\rangle_1 |{\rm H}\rangle_2)$. The factor of $\frac{1}{2}$ instead of $\frac{1}{\sqrt{2}}$ implies that half of the photon pairs do not contribute to entanglement.

The flexibility of waveguide based quasi phase matching as far as the wavelengths of operation are concerned is crucial in the emerging field of quantum repeaters. Quantum repeaters distribute quantum correlations between two parties over long distances [67]. A photon pair source is an essential component of a quantum repeater. The emission wavelengths of the source is determined, on the one hand the possibility to transmit the quantum state over a standard single mode fiber ($\lambda_1 \approx 1310$ nm) and on the other hand by the wavelength of operation of a quantum memory (for example $\lambda_2 \approx 880$ nm). Type I down conversion based emission in these wavelengths can be achieved in our waveguides with $\Lambda \approx 6\,\mu$m

($\lambda_{\mathrm{p}} \approx 532$ nm). Moreover, the emission wavelengths λ_1 and λ_2 can be separated by a wavelength division de-multiplexer integrated into the same substrate. The residual pump photons at $\lambda_{\mathrm{p}} = 532$ nm can be suppressed by suitably designed dielectric mirrors deposited on the end-face of the substrate (Design is in principle similar to the dielectric mirrors used to suppress the pump at $\lambda_{\mathrm{p}} = 780$ nm). The schematic of such a source is shown in Fig. 6.1.
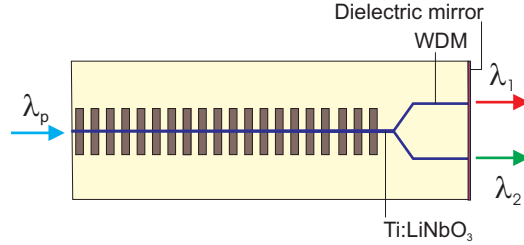
Figure 6.1: The schematic of a photon pair source with wavelengths of emission $\lambda \approx$ 880 nm and $\lambda \approx$ 1310 nm. The photons of a pair are separated by a wavelength division de-multiplexer integrated behind the source. The dielectric mirror deposited on the end-face of the sample provides pump supression.

The non-linear property of the medium can be exploited not only to demonstrate photon pair sources (by down conversion) but also to implement efficient single photon detectors by frequency up-conversion. The single photon detectors in the telecom range of $\lambda \approx 1550$ nm is based on InGaAs avalanche photo-diodes, which has the draw back of poor efficiencies $\eta < 25\%$ (please refer Chapter 4). The idea is to up-convert the frequency of the single photon in $\lambda = 1550$ nm range to the visible range ($\lambda \approx 600$ nm), where efficient Si avalance photo-diodies with efficiency $\eta \approx 60\%$ are available [68; 69].

The list of possible future activities outlined points to the fact that integrated optics is poised to scale new heights in fields where photon pair sources are essential.

APPENDIX A

Sellmeier Expressions of Refractive indices

W. Sellmeier, in 1871, introduced an empirical model for the refractive index of a material as a function of wavelength and temperature. The empirical model contains 'oscillator' terms which represent the characteristic resonant frequencies of the material. In the context of non-linear optics, the Sellmeier model is a powerful tool to calculate the refractive indices of different materials. The dispersion in the refractive index is a crucial input to calculate the phase matching characteristic of the non-linear process under consideration. The Sellmeier model for the bulk LiNbO$_3$ which was used for many calculations in this thesis is as follows [20]:

$$
\begin{aligned}
\mathrm{n}_\mathrm{o}^2(\lambda, T) &= 4.9048 + \frac{0.1178 + 2.346 \times 10^{-8}\,\mathrm{F}}{\lambda^2 - (0.21802 - 2.9671 \times 10^{-8}\,\mathrm{F})^2} - 0.027153\,\lambda^2 \\
&\quad + 2.1429 \times 10^{-8}\,\mathrm{F} \\
\mathrm{n}_\mathrm{e}^2(\lambda, T) &= 4.5820 + \frac{0.09921 + 5.2716 \times 10^{-8}\,\mathrm{F}}{\lambda^2 - (0.21090 - 4.9143 \times 10^{-8}\,\mathrm{F})^2} - 0.021940\,\lambda^2 \\
&\quad + 2.2971 \times 10^{-8}\,\mathrm{F}
\end{aligned}
\tag{A.1}
$$

In the above equations n$_\mathrm{o}$ is the ordianry index and n$_\mathrm{e}$ is the extra-ordinary index. F is a temperature dependent factor defined by F = (T-T$_0$) (T+T$_0$+546), where T$_0$ = 24.5°C. Note that the dimensions of the wavelength λ is $[\lambda] = \mu$m and that of temperature T is [T] = °C.

APPENDIX B

Quantum Theory of Spontaneous Parametric Down Conversion

As mentioned in Chapter 1, a quantum theory of fields is required to understand spontaneous parametric down conversion. The appendix summarizes the important results concerning the down conversion hence obtained. For a detailed description of the general quantum theory of fields, please refer the new book by Alain Aspect [70]. The theory of down conversion in the context of noise in other parametric interactions was first worked out by Yariv [71; 72]. The model presented here follows closely that of Suhara [35].

In the quantum model, the field associated with the normal modes of the waveguide are quantized, i.e., we define creation and annihilation operators for the normal mode. *A normal mode has a well-defined polarization dependent propagation constant (associated with the propagation along z direction and confinement along the transverse direction) and a well-defined frequency.* In the absence of the $\chi^{(2)}$, the evolution of normal modes are un-coupled. In the presence of $\chi^{(2)}$, the evolution equations for the annihilation operators are

$$
\begin{aligned}
\partial_z \hat{a}_{\text{TE}}(z) &= i\kappa\, A_{\text{p}}\, \hat{a}_{\text{TM}}^{\dagger}\, e^{-j\Delta\beta z} \\
\partial_z \hat{a}_{\text{TM}}(z) &= i\kappa\, A_{\text{p}}\, \hat{a}_{\text{TE}}^{\dagger}\, e^{-j\Delta\beta z} \\
\partial_z A_{\text{p}} &\approx 0
\end{aligned}
\tag{B.1}
$$

In the above equations A_{p} is the complex amplitude of the pump. The normal mode corresponding to the pump is not quantized. For precise definitions of the different variables used in the above equations, please refer Chapter 2. The solution of the set of coupled mode equations Eq. B.1 is given by

$$
\begin{bmatrix} \hat{a}_{\text{TE}}(L) \\ \hat{a}_{\text{TM}}^{\dagger}(L) \end{bmatrix} = M \begin{bmatrix} \hat{a}_{\text{TE}}(0) \\ \hat{a}_{\text{TM}}^{\dagger}(0) \end{bmatrix}
\tag{B.2}
$$

where M is

$$
M = \begin{bmatrix} e^{\frac{j\Delta\beta z}{2}}\left(\cosh(\Gamma z) - \frac{j\Delta\beta}{2\Gamma}\sinh(\Gamma z)\right) & e^{\frac{j\Delta\beta z}{2}}\left(-\frac{j\kappa A_{\text{p}}}{\Gamma}\sinh(\Gamma z)\right) \\ e^{-\frac{j\Delta\beta z}{2}}\left(\frac{j\kappa^* A_{\text{p}}^*}{\Gamma}\sinh(\Gamma z)\right) & e^{-\frac{j\Delta\beta z}{2}}\left(\cosh(\Gamma z) - \frac{j\Delta\beta}{2\Gamma}\sinh(\Gamma z)\right) \end{bmatrix}
\tag{B.3}
$$

M is a non-unitary matrix which preserves the commutation relations between the operators. The interaction hamiltonian density $\mathcal{H}_{\text{I}}$ associated with down conversion is

$$
\begin{aligned}
\mathcal{H}_{\text{I}}(t,z) &= \hbar\kappa A_{\text{p}}\, e^{i(\Delta\omega t - \Delta\beta z)}\, a_{\text{TE}}^{\dagger} a_{\text{TM}}^{\dagger} + \text{Hermitian. Conjugate.} \qquad \text{with} \\
[\mathcal{H}_{\text{I}}] &= \frac{J}{m}
\end{aligned}
\tag{B.4}
$$

The density is only one-dimensional (along the interaction length), along the transverse directions the integration is already done and hidden in the overlap integral factor η (see expression for κ in Chapter 2). The quantum states of the TE and TM normal modes, in the presence of interaction, is derived as follows:

$$
\begin{aligned}
|\psi\rangle_{12} &= e^{-\frac{i}{\hbar} \int_{-\infty}^{+\infty} dt' \int_0^L dz\, \mathcal{H}(t',z)} |0\rangle_1 |0\rangle_2 \\
&= \sqrt{1 - |\zeta|^2} \sum_{n=0}^{n=\infty} \zeta^n |n\rangle_1 |n\rangle_2 \qquad \text{where} \\
\zeta &= \frac{\kappa_p A_p \sinh \Gamma L}{\Gamma \cosh \Gamma L - \frac{i\Delta\beta}{2} \sinh \Gamma L}
\end{aligned}
\tag{B.5}
$$

The subscript 1 (2) indicates a TE (TM) normal mode with frequency $\omega_{TE}(\omega_p - \omega_{TE})$. The result shows that the joint photon state of any two normal modes is not a joint single photon state $|1\rangle_1 |1\rangle_2$, instead has a Bose-Einstein distribution over the number states. The spectral dependence of the emission enters into the model through the phase mismatch parameter $\Delta\beta$.

When the pump power is low, $\kappa A_p << 1$ and $|\zeta| << 1$, the joint state $|\psi\rangle_{12}$ can be approximated as follows:

$$
\begin{aligned}
|\psi\rangle_{12} &\approx |0\rangle_1 |0\rangle_2 + \kappa_p A_p L \, \mathrm{sinc}\left(\frac{\Delta\beta L}{2}\right) e^{\frac{i\Delta\beta L}{2}} |1\rangle_1 |1\rangle_2 \\
&= |0\rangle_1 |0\rangle_2 + \tilde{f}(\omega_{TE}, \omega_p - \omega_{TE}) |1\rangle_1 |1\rangle_2
\end{aligned}
\tag{B.6}
$$

The function $\tilde{f}(\omega_{TE}, \omega_p - \omega_{TE})$ is the joint state function. The importance of the state function is evident in the coincidence measurements using two single photon detectors, after spatially separating the TE and TM normal modes. This is discussed in detail in Appendix C.

The phase mismatch parameter $\Delta\beta$ can be re-written in terms of $\delta\omega$, the deviation of emission frequency from the exactly (quasi-) phase matched case.

$$
\begin{aligned}
\Delta\beta &= \beta_{TE}(\omega_{TE)} + \beta_{TM}(\omega_p - \omega_{TE}) + \frac{2\pi}{\Lambda} - \beta_{TE}(\omega_p) \\
&\approx (\partial_\omega \beta_{TE} - \partial_\omega \beta_{TM})\delta\omega \\
&= \left(\frac{1}{V_{TE}} - \frac{1}{V_{TM}}\right)\delta\omega
\end{aligned}
\tag{B.7}
$$

In the above equations $V_{TE,TM}$ are the group velocities of the normal modes. When we substitute the expression for $\Delta\beta$ in Eq. B.6 we arrive at

$$
\tilde{f}(\delta\omega, -\delta\omega) = \kappa_p A_p L \, sinc\left[\left(\frac{L}{2V_{TE}} - \frac{L}{2V_{TM}}\right)\delta\omega\right] e^{i\left(\frac{L}{2V_{TE}} - \frac{L}{2V_{TM}}\right)\delta\omega}
\tag{B.8}
$$

The dimensionless function $\tilde{f}(\delta\omega, -\delta\omega)$ has the familiar sinc profile associated with quasi-phase matched process. The bandwidth of the function is limited by the group velocity difference between TE and TM normal modes.

Quantum Theory of Coincidence Counting Using Two Single Photon Detectors

Quantum theory of coincidence counting using two single photon detectors is explained. The detectors are kept behind a polarization beam splitter which spatially separates the orthogonally polarized photons generated by type II down conversion. The schematic of the coincidence counting set up is shown in Fig. C.1. For details concerning the measurement process please refer Chapter 4.
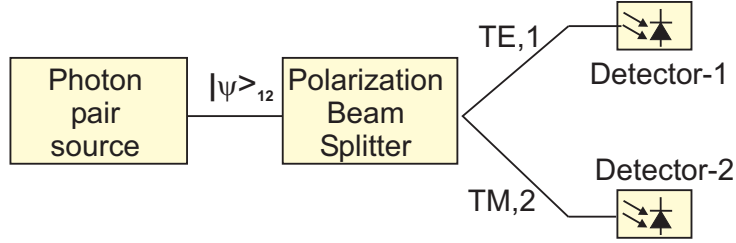
Figure C.1: Schematic of the coincidence measurement setup. The polarization beam splitter behind the source spatially separates the orthogonally polarized photon pairs. The model presented in this chapter explains the coincidence count of the detectors behind the splitter.

The two photon state $|\psi\rangle_{12}$ behind the polarization beam splitter (Appendix B) is

$$|\psi\rangle_{12} \approx |0\rangle_1 |0\rangle_2 + \tilde{f}(\omega, \omega_p - \omega) \, |1\rangle_1 |1\rangle_2 \qquad \text{(C.1)}$$

where ω is the emission wavelength of the TE polarized field, ω_p is the pump wavelength. $|\omega\rangle_1$ represents a single photon state of the TE polarized mode at a well defined frequency ω at the TE output port (1) of the polarization beam splitter. Similarly, $|\omega\rangle_2$ represents a single photon state of the TM polarized mode at the TM output port (2) of the splitter. $\tilde{f}(\omega, \omega_p - \omega)$ is the joint state function, peaked at the frequency of exact (quasi-) phase matching, whose width is determined by the bandwidth of the phase matching process. In these calculations, a photon is defined as an eigenstate of a normal mode with well defined frequency and propagation constant along the waveguide.

The probability density function associated with the coincident count rate of the two detectors, $g(t_1, t_2)$, is given by

$$
\begin{aligned}
g(t_1, t_2) &= \langle E_1^{(+)}(t_1) E_2^{(+)}(t_2) E_1^{(-)}(t_1) E_2^{(-)}(t_2) \rangle \\
&= \left| E_1^{(-)}(t_1) E_2^{(-)}(t_2) \, |\psi\rangle_{12} \right|^2,
\end{aligned}
\qquad \text{(C.2)}
$$

where t_1 and t_2 are the arrival times of the photons at detectors 1 and 2 respectively. $E_{1,2}^{(\pm)}$ are the operators representing positive or negative frequency amplitudes of the electric fields at ports 1 or 2. In other words,

$$E_1^{(+)}(t_1) \; = \; \int d\omega \, a_1(\omega) \, e^{-i\omega t_1} \qquad \text{and } E_1^{(-)}(t_1) \; = \; \left[E_1^{(+)}(t_1) \right]^\dagger \qquad \text{(C.3a)}$$

$$E_2^{(+)}(t_2) \; = \; \int d\omega \, a_2(\omega) \, e^{-i\omega t_2} \qquad \text{and } E_2^{(-)}(t_1) \; = \; \left[E_1^{(+)}(t_1) \right]^\dagger \qquad \text{(C.3b)}$$

$a_1(\omega)$ and $a_2(\omega)$ are the annihilation operators associated with the TE polarized field at port 1 and the TM polarized field at port 2, respectively. Substituting Eq.C.3 into Eq. C.2, we arrive at a simplified expression for $g(t_1, t_2)$ given by

$$g(t_1, t_2) \; =$$
$$\left| \int d\omega d\omega' d\omega'' \, \tilde{f}(\omega, \omega_p - \omega) e^{-j[\omega' t_1 + \omega'' t_2]} a_1(\omega') a_2(\omega'') \, |\omega\rangle_1 \, |\omega_p - \omega\rangle_2 \right|^2$$

$$= \left| \int d\omega d\omega' d\omega'' \, \tilde{f}(\omega, \omega_p - \omega) e^{-j[\omega' t_1 + \omega'' t_2]} \delta(\omega' - \omega) \delta(\omega'' - \omega_p + \omega) |0\rangle_1 \, |0\rangle_2 \right|^2$$

$$= \left| e^{-j\omega_p t_2} \int d\omega \, \tilde{f}(\omega, \omega_p - \omega) e^{-j[\omega(t_1 - t_2)]} \right|^2$$

$$= \left| e^{-j(\omega_0 t_1 + (\omega_p - \omega_0) t_2)} \int d\omega \, \tilde{f}(\delta\omega, -\delta\omega) e^{-j[\delta\omega(t_1 - t_2)]} \right|^2$$

$$g(t_1, t_2) \; = \; |f(t_1 - t_2)|^2 .$$
$$\text{(C.4)}$$

The function $f(t_1\text{-}t_2)$ is the inverse Fourier transform of the function $\tilde{f}(\delta\omega; -\delta\omega)$. The function is independent of the absolute value of arrival times t_1 and t_2, but dependent on the arrival time difference t_1-t_2.

$$f(t_1 - t_2) \; = \; \text{IFT}\{ \, \tilde{f}(\delta\omega; -\delta\omega) \, \}$$
$$= \; \text{IFT} \left\{ \kappa A_p L \, sinc \left[\left(\frac{L}{2V_{TE}} - \frac{L}{2V_{TM}} \right) \delta\omega \right] e^{i \left(\frac{L}{2V_{TE}} - \frac{L}{2V_{TM}} \right) \delta\omega} \right\} \quad \text{(C.5)}$$
$$f(t_1 - t_2) \; = \; \frac{\kappa A_p L}{\tau_g} \, rect \left[\frac{t_1 - t_2 - \tau_g}{2\tau_g} \right]$$

where $\tau_g \; = \; \left(\frac{L}{2V_{TE}} - \frac{L}{2V_{TM}} \right)$ and IFT is the inverse fourier transform [73]. The time τ_g is the average arrival time difference between the photons in the TE and TM modes. The function f has dimension $[f] = \frac{1}{s}$ and g has dimension $[g] = \frac{1}{s^2}$. A time integral over g has dimensions of $\frac{1}{s}$ and is interpreted as the arrival time-difference distribution of the coincident count rate. This time distribution is shown in Fig. C.2.

The rectangular function has a width $2\tau_g$. The distribution points to the fact that the photon pairs can be generated anywhere in the interaction region $0 \leq z \leq L$ with equal probability. The photon pairs with arrival time difference of zero correspond to those generated at $z = L$. Those with arrival time difference of
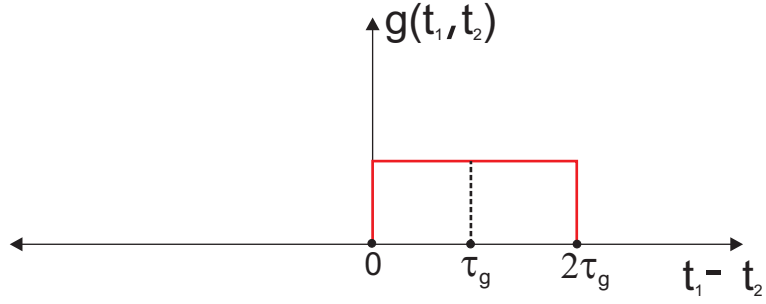
Figure C.2

$2\tau_\mathrm{g}$ correspond to the pairs generated at z = 0.

The calculated value of average arrival time difference between the TE and TM photons generated in a 5 cm long sample of LiNbO$_3$ is ≈ 6 ps. So the coincident count distribution will have a width of 12 ps. However, with the single photon detectors and correlation electronics, it is not possible to resolve the distribution. The jitter in the detectors limits the resolution to ≈ 1 ns (See chapter 4 for more details).

The model derived in this chapter to explain the coincident counts is restricted to a non-entangled state $|\psi\rangle_{12}$. However, the model can be extended to explain the coincident counts seen when characterizing an entangled state. In this case, the phase term $e^{-j(\omega_0 t_1 + (\omega_p - \omega_0)t_2)}$, which we neglected in the final step of Eq. C.4, becomes crucial and leads to interference effects in the coincident counts (see Chapter 5 for more details).

REFERENCES

[1] D. ter. Haar, *The old quantum theory*, Pergamon Press, NY, USA, 1967.

[2] A. Beck, *The Collected Papers of Albert Einstein, Volume 2: The Swiss Years: Writings, 1900-1909. (English translation supplement)*, Princeton University Press, NJ, USA, 1990.

[3] T. H. Maiman, "Stimulated optical radiation in ruby," *Nature* **187**, pp. 493–494, 1960.

[4] S. E. Miller, "Integrated optics - an introduction," *Bell System Technical Journal* **48**, pp. 2059–2069, 1969.

[5] A. Einstein, B. Podolsky, and N. Rosen, "Can quantum mechanical description of reality be considered complete?," *Physical Review Letters* **47**, pp. 777–780, 1935.

[6] J. S. Bell, "On the Einstein Podolsky Rosen paradox," *Physics* **1**, pp. 195–200, 1964.

[7] A. Aspect, P. Grangier, and G. Roger, "Experimental tests of realistic local theories via Bell's theorem," *Physical Review* **47**, pp. 460–463, 1981.

[8] N. Gisin, G. Ribordy, W. Tittel, and H. Zbinden, "Quantum cryptography," *Review of Modern Physics* **74**, p. 145195, 2002.

[9] Y. Kim, S. P. Kulik, and Y. Shih, "Quantum teleportation of a polarization state with a complete Bell state measurement," *Physical Review Letters* **86**, p. 13701373, 2001.

[10] M. Halder, A. Beveratos, N. Gisin, V. Scarani, C. Simon, and H. Zbinden, "Entangling independent photons by time measurement," *Nature Physics* **3**, pp. 692–695, 2007.

[11] L. Arizmendi, "Photonic applications of lithium niobate crystals," *Physica Status Solidi (a)* **201**, pp. 253–283, 2004.

[12] M. M. Fejer, G. A. Magel, D. H. Jundt, and R. L. Byer, "Quasi-phase-matched second harmonic generation: tuning and tolerances," *Physical Review Letters* **28**, pp. 2631 –2654, 1992.

[13] P. Baldi, M. P. D. Micheli, and K. E. Hadi, "Proton exchanged waveguides in LiNbO$_3$ and LiTaO$_3$ for integrated lasers and nonlinear frequency converters," *Optical Engineering* **37**, p. 1193, 1998.

[14] S. Tanzilli, W.Tittel, H. D. Riedmatten, H. Zbinden, P.Baldi, M.DeMicheli, D. Ostrowsky1, and N.Gisin, "PPLN waveguide for quantum communication," *European Physics Journal D.* **18**, pp. 155–160, 2002.

[15] T. Nosaka, B. K. Das, M. Fujimura, and T. Suhara, "Cross-polarized twin photon generation device using quasi-phase matched lithium niobate waveguide," *IEEE Photonics Techonology Letters* **18**, pp. 124–126, 2006.

[16] A. Martin, V. Cristofori, P. Aboussouan, H. Herrmann, W. Sohler, D. Ostrowsky, and O. A. andS. Tanzilli, "Integrated optical source of polarization entangled photons at 1310 nm," *Optics Express* **17**, pp. 1033–1041, 2009.

[17] T. Suhara, "Generation of quantum-entangled twin photons by waveguide nonlinear-optic devices," *Laser and Photonics Review* **3**, pp. 370–393, 2009.

[18] C. K. Hong and L. Mandel, "Experimental realisation of a localised one-photon state.," *Physical Review Letters* **56**, pp. 58–60, 1986.

[19] R. V. Schmidt and I. P. Kaminow, "Metal diffused optical waveguides in lithium niobate," *Journal of Lightwave Technology* **6**, pp. 847–861, 1974.

[20] G. J. Edwards and M. Lawrence, "A temperature-dependent dispersion equation for congruently grown lithium niobate," *Optical and Quantum Electronics* **16**, pp. 373–375, 1984.

[21] W. K. Burns, P. H. Klein, and E. J. West, "Ti diffusion in lithium niobate planar and channel optical waveguides," *Journal of Applied Physics* **50**, pp. 6175–6182, 1979.

[22] K. Okamoto, *Fundamentals of optical waveguides*, Academic Press, Burlington, MA 01803, USA, 2006.

[23] L. Bersiner, U. Hempelmann, and E. Strake., "Numerical analysis of passive integrated-optical polarization splitters: comparison of finite-element method and beam-propagation method results.," *Journal of Optical Society of America-B* **8**, pp. 422–433, 1991.

[24] J. A. Armstrong, N. Bloembergen, J. Ducuing, and P. S. Pershan, "Interactions between light waves in a nonlinear dielectric.," *Physical Review* **127**, pp. 1918–1939, 1962.

[25] F. A. Hopf and G. I. Stegeman, *Applied Classical Electrodynamics: Volume 2, Nonlinear Optics*, John Wiley and Sons, Inc., NY, USA, 1986.

[26] D. Hofmann, *Nichtlineare, integriert optische Frequenzkonverter fuer das mittlere Infrarot mit periodisch gepolten Ti:LiNbO3-Streifenwellenleitern.* PhD thesis, Universitaet Paderborn.

[27] D. Buechter, *Nonlinear Frequency Conversion to/from the Mid-Infrared in Ti:PPLN waveguides for Spectroscopy and Free-Space Optical Communication.* PhD thesis, Universitaet Paderborn.

[28] A. M. Prokhorov, Y. S. Kuz'minov, and O. A. Khachaturyan, *Ferroelectric Thin-Film Waveguides in Integrated Optics and Optoelectronics*, Cambridge International Science Publishing, Cambridge, England, 1996.

[29] V. Gopalan, V. Dielorf, and D. A. Scrymgeour, "Defect - domainwall interactions in trigonal ferroelectrics," *Annual Review of Materials Research* **37**, pp. 449–489, 2007.

[30] R. S. Weis and T. K. Gaylord, "Lithium niobate: Summary of physical properties and crystal structure.," *Applied Physics A* **37**, pp. 191–204, 1985.

[31] D. Lee, H. Xu, V. Gopalan, V. Dierolf, and S. R. Phillpot, "Structure and energetics of ferroelectric domain walls in linbo3 from atomic-level simulation," *Physical Review B* **82**, 2010.

[32] S. E. Harris, M. K. Oshman, and R. L. Byer., "Observation of tunable optical parametric fluorescence," *Physical Review Letters* **18**, pp. 732–734, 1967.

[33] W. Grundkoetter, *Dynamik nichtlinearer Wechselwirkungen zweiter Ordnung in integriert optischen Wellenleitern.* PhD thesis, Universitaet Paderborn.

[34] U. Leonhardt, *Essential Quantum Optics*, Cambridge University Press, Cambridge, UK, 2010.

[35] T. Suhara, "Quantum theory analysis of twin-photon beams generated by parametric fluorescence," *IEEE Journal of Quantum Electronics* **41**, pp. 1203–1212, 2005.

[36] W. Tittel, J. Brendel, H. Zbinden, and N. Gisin, "Violation of bell inequalities by photons more than 10 km apart," *Physical Review Letters* **81**, pp. 3563–3566, 1998.

[37] P. G. Kwiat, E. Waks, A. G. White, I. Appelbaum, and P. H. Eberhard, "Ultrabright source of polarization-entangled photons," *Physical Review A.* **60**, pp. 773–776, 1999.

[38] T. Jennewein, C. Simon, G. Weihs, H. Weinfurter, and A. Zeilinger, "Quantum cryptography with entangled photons," *Physical Review Letters* **84**, pp. 4729–4732, 2000.

[39] M. Fiorentino, P. L. Voss, J. E. Sharping, and P. Kumar, "All-fiber photon-pair source for quantum communications," *IEEE Photonics Technology Letters* **14**, pp. 983–985, 2002.

[40] X. Li, P. L. Voss, J. E. Sharping, and P. Kumar, "Optical-fiber source of polarization-entangled photons in the 1550 nm telecom band," *Physical Review Letters* **94**.

[41] A. Martin, A. Issautier, H. Herrmann, W. Sohler, D. B. Ostrowsky, O. Alibart, and S. Tanzilli, "A polarization entangled photon-pair source based on a type-ii periodically poled lithium niobate waveguide emitting at a telecom wavelength," *New Journal of Physics* **12**, 2010.

[42] T. Suhara and M. Fujimura, *Waveguide Nonlinear-Optic Devices*, Springer, Berlin, Germany, 2003.

[43] R. Regener and W. Sohler, "Loss in low-finesse titanium in lithium niobate optical waveguide resonators," *Applied Physics B* **36**, pp. 143–147, 1985.

[44] S. Tanzilli, W. Tittel, M. Halder, O. Alibart, P. Baldi, N. Gisin1, and H. Zbinden1, "A photonic quantum information interface," *Nature* **437**, pp. 116–120, 2005.

[45] A. Thomas, H. Herrmann, V. Quiring, R. Ricken, and W. Sohler, "Packaged integrated SPDC photon pair source with polarisation splitter.," *Proceedings of SECOQC Demonstration and International Conference* , 2008.

[46] *MODEL SR850 DSP Lock-In Amplifier.* Stanford Research Systems, CA 94089, USA, 1992.

[47] *HR-320 Instructions Manual.* I.S.A JOBIN YVON, Longjumeau Cedex 91163, France, 1992.

[48] B. E. A. Saleh and M. C. Teich, *Fundamentals of Photonics*, John Wiley and Sons, NY, USA, 1991.

[49] E. Schal, "Integriert optische schaltkreise zur erzeugung einzelner photonen-paare," Master's thesis, Universitaet Paderborn, 2007.

[50] *id 201 Single-Photon Detection Module, Operating Guide, version 3.* Id Quantique, Carouge 1227, Switzerland, 2007.

[51] A. Lacaita, F. Zappa, S. Cova, and P. Lovati, "Single-photon detection beyond 1 μm: performance of commercially available InGaAs/InP detectors," *Applied Optics* **35**, pp. 2986–2996, 1996.

[52] G. Ribordy, J. D. Gautier, H. Zbinden, and N. Gisin, "Performance of ingaas/inp avalanche photodiodes as gated-mode photon counters," *Applied Optics* **37**, pp. 2272–2277, 1998.

[53] *TDC-GPX Ultra high Performance 8 Channel Time-to-Digital Converter.* Acam Messelectronic GMBH, Stutensee-Blankenloch, Germany, 2006.

[54] G. Fujii, N. Namekata, M. Motoya, S. Kurimura, and S. Inoue., "Bright narrowband source of photon pairs at optical telecommunication wavelengths using a type-II periodically poled lithium niobate waveguide," *Optics Express* **15**, pp. 12769–12776, 2007.

[55] T. Suhara, G. Nakaya, J. Kawashima, and M. Fujimura, "Quasi-phase-matched waveguide devices for generation of postselection-free polarization-entangled twin photons," *IEEE Photonics Technology Letters* **21**, pp. 1096–1098, 2009.

[56] A. Thomas, H. Herrmann, and W. Sohler, "Novel source of polarization entangled photon pairs using a PPLN waveguide with interlaced domains," *Proceedings of the 15th European Conference on Integrated Optics* , 2010.

[57] D. N. Klyshko, "Use of two-photon light for absolute calibration of photo-electric detectors," *Soviet Journal of Quantum Electronics* **10**, 1980.

[58] R. J. Glauber, "Coherent and incoherent states of the radiation field," *Physical Review Letters* **10**, pp. 2766–2788, 1963.

[59] M. O. Scully and M. S. Zubairy, *Quantum Optics*, Cambridge University Press, Cambridge, UK, 1997.

[60] T. E. Kiess, Y. H. Shih, A. V. Sergienko, and C. O. Alley, "Einstein-Podolsky-Rosen-Bohm experiment using pairs of light quanta produced by type-II parametric down-conversion," *Physical Review Letters* **71**, pp. 3893–3897, 1993.

[61] K. Hasegawa, M. Obinata, N. Namekata, S. Kurimura, and S.Inoue, "Generation of narrowband polarization-entangled photon-pairs using a type-II periodically poled lithium niobate waveguide," *Proceedings of SECOQC Demonstration and International Conference* , 2008.

[62] C. Silberhorn, "Detecting quantum light," *Contemporary Physics* **48**, pp. 143–156, 2008.

[63] "Material characteristics of UV curable adhesives." `http://www.epotek.com`, 2010.

[64] A. Christ, A. Eckstein, P. J. Mosley, and C. Silberhorn, "Pure single photon generation by type-I pdc with backward-wave amplification," *Optics Express* **17**, pp. 3441–3446, 2009.

[65] C. Canalias and V. Pasiskevicius, "Mirrorless optical parametric oscillator," *Nature Photonics* **1**, pp. 459–462, 2007.

[66] L. Gui, *Periodically poled ridge waveguides and photonic wires in $LiNbO_3$ for efficient non-linear interactions.* PhD thesis, Universitaet Paderborn.

[67] R. Thew, "Quantum repeaters for long distance fiber based quantum communication." `http://www.quantumrepeaters.eu`, March 2010.

[68] *id 100 Single-Photon Detection Module, Operating Guide.* Id Quantique, Carouge 1227, Switzerland, 2010.

[69] C. Langrock, E. Diamanti, R. V. Roussev, Y. Yamamoto, M. M. Fejer, and H. Takesue, "Highly efficient single-photon detection at communication wavelengths by use of upconversion in reverse-proton-exchanged periodically poled $LiNbO_3$ waveguides," *Optics Letters* **30**, pp. 1725–1727, 2005.

[70] G. Grynberg, A. Aspect, and C. Fabre, *Introduction to Quantum Optics: From the Semi-classical Approach to Quantized Light*, Cambridge University Press, Cambridge, UK, 2010.

[71] W. H. Louisell, A. Yariv, and A. E. Siegman, "Quantum fluctuations and noise in parametric processes.I.," *Physical Review* **124**, pp. 1646–1654, 1961.

[72] J. P. Gordon, W. H. Louisell, and L. R. Walker, "Quantum fluctuations and noise in parametric processes.II.," *Physical Review* **129**, pp. 481–485, 1963.

[73] G. B. Arfken and H. J. Weber, *Mathematical methods for physicists*, Academic Press, San Diego, USA, 2001.

ACKNOWLEDGEMENTS